AN ABSTRACT OF THE DISSERTATION OF

Bemnet Alemayehu for the degree of Doctor of Philosophy in Radiation Health Physics presented on August 15, 2013.
Title: Real-time Radioxenon Measurement using a Compton-suppressed Well-type Phoswich Detector for Nuclear Explosion Monitoring

Abstract approved:

_____

Abdollah T. Farsoni

Radioxenon detection is a technique used to monitor nuclear explosion and verify the Comprehensive Nuclear-Test-Ban Treaty (CTBT). Because of an ultra-low concentration of radioxenon at radioxenon monitoring stations, radioxenon detection systems must have high sensitivity. This sensitivity is measured in terms of detector's minimum detectable concentration (MDC). It is required that radioxenon monitoring systems should have a MDC of less than or equal to 1 mBq/m^3 for ^{133}Xe. A Well-type Actively Shielded Phoswich Detector (WASPD) for radioxenon detection was designed and assembled at the Radiation Detection and Dosimetry lab at Oregon State University. The active shielding mechanism is integrated into the phoswich detector to improve the MDC of the radioxenon by reducing unwanted background events. Anode pulses were processed using a user-programmable digital pulse processor. All digital processing functions were implemented in a FPGA device in real-time. The detector was characterized for different radioxenon isotopes. MDC calculation of the detector showed that the results are close or below 1 mBq/m^3 for all radioxenon isotopes.

Real-time Radioxenon Measurement using a Compton-suppressed Well-type Phoswich Detector for Nuclear Explosion Monitoring

by

Bemnet Alemayehu

A DISSERTATION

Submitted to

Oregon State University

in partial fulfillment of
the requirements for the
degree of

Doctor of Philosophy

Presented August 15, 2013
Commencement June 2014

Doctor of Philosophy dissertation of Bemnet Alemayehu

Presented on August 15, 2013.

APPROVED:

Major Professor, representing Radiation Health Physics

Head of the Department of Nuclear Engineering and Radiation Health Physics

---

Dean of the Graduate School

I understand that my dissertation will become part of the permanent collection of Oregon State University libraries. My signature below authorizes release of my dissertation to any reader upon request.

Bemnet Alemayehu, Author

ACKNOWLEDGMENTS

Foremost, my sincere thanks go to my advisor Dr. Abi Farsoni for his support of my Ph.D study and research. He is a very kind and genius advisor. I have learnt a lot from him. Without his support and persistent help this dissertation would not have been possible.

Furthermore, I would also like to thank other members of my dissertation committee: Professor David M. Hamby, Dr. Alena Paulenova, Professor Huaping Liu and Dr. Leah Minc, for their guidance in my research work.

Thanks to all my lab mates and Radiation center staffs: Abdulsalam Alhawsawi, Eric Becker, Leila Ranjbar, Scott Menn and Steve Smith for your support in the research.

For my wife Hiwot kassahun: Thank you for your love, support and patience.

For my families: Thank you for your support in every way you could during my studies.

TABLE OF CONTENTS

Page

TABLE OF CONTENTS (Continued)

LIST OF FIGURES

LIST OF FIGURES (Continued)

LIST OF FIGURES (Continued)

LIST OF FIGURES (Continued)

LIST OF TABLES

Real-time Radioxenon Measurement using a Compton-suppressed Well-type Phoswich Detector for Nuclear Explosion Monitoring

1. Background

1.1 The Comprehensive Nuclear-Test-Ban Treaty (CTBT)

The Comprehensive Nuclear-Test-Ban Treaty (CTBT) prohibits carrying out or participating in the carrying out of any nuclear weapon test explosion or any other nuclear explosion (Gupta, 1999). The treaty was adopted on 19 November 1996. But it has not yet entered into force. As of February 2013, 183 countries have signed the treaty, of which 159 have also ratified it. The last to ratify the treaty was Indonesia on 6 February 2012. But 44 specific nuclear technology holder countries must sign and ratify before the CTBT can enter into force. In order to enforce the treaty, a preparatory commission, CTBT organization (CTBTO) was established in Vienna, Austria. CTBTO oversees the treaty's entry into force, the construction and operation of the International Monitoring System (IMS) and the International Data Centre (IDC). The IMS consists of 321 measurement stations all over the world. Fig.1.1 shows the global distribution of the monitoring stations. Two major monitoring methods, wave and radionuclide monitoring, are used to detect signals that could indicate a possible nuclear explosion ("CTBTO Preparatory Commission," 2013.) .

Seismic, hydroacoustic and infrasound monitoring are part of the wave monitoring methods. Data from these measurement stations will be transmitted to the IDC in Vienna through satellite links.

Seismic monitoring is based on seismic waves generated as a result of underground events. When seismic waves hit a seismometer, the instrument transforms the

vibration into electrical signals. These waves are detected by seismometers which convert seismic events to electrical signals. The signals generated will be used to detect and locate underground explosions. There are 170 seismic stations in 76 countries around the world.

Fig. 1.1: Global International Monitoring Stations.(Taken from ("CTBTO Preparatory Commission," 2013)).

Hydroacoustic monitoring is based on the study of sound waves in the water. When sound waves hit a hydoacoustic monitoring station, they will be registered by hydrophones. Hydrophones are sensitive underwater microphones that convert changes in water pressure to electrical signals. Data obtained from this monitoring will be used to determine the location of a nuclear explosion underwater, near the ocean surface or near its coasts. There are 11 hydroacoustic monitoring stations in 8 countries globally.

Infrasound monitoring stations measure very low acoustic waves (infrasound) which are inaudible to the human ear. Atmospheric and shallow underground nuclear explosions can generate these waves that cause changes in the atmospheric pressure. These changes are measured using microbarometers at the infrasound network. The microbarometer transforms the infrasound waves into electrical

impulses. There are 60 infrasound monitoring stations in 35 countries globally ("CTBTO Preparatory Commission," 2013).

Radionuclide monitoring measures the abundance of radioactive particles and gases in the air that result due to nuclear explosions. Currently, there are 80 radionuclide stations in 27 countries around the world. Out of the 80 IMS radionuclide stations, 40 have noble gas detection capabilities. In half of the currently existing radionuclide monitoring stations, airborne radioactive particles are captured and analyzed. But if the explosion is well-contained, radioactive particles will not be released. The alternative solution is measuring the radioactive noble gas isotopes instead. Because they are inert and exist in gaseous state, they can be detected very far away from the explosion site ("CTBTO Preparatory Commission," 2013).

1.2 Radioxenon detection

Among different radioactive noble gases released in nuclear explosions, four xenon isotopes (Radioxenon) are identified to be relevant to indicate nuclear explosion because of their half-lives and fission yields. These are ^{131m}Xe, ^{133}Xe,^{133m} Xe and ^{135}Xe (Kalinowski, Becker, Saey, Tuma, & Wotawa, 2008). The IMS installs radioxenon detectors to monitor these gases at the noble gas measurement stations. The detectors to be employed at these stations should be able to measure a very low concentration of radioxenon in the atmosphere where the background is relatively high. This sensitivity is measured in terms of detector's minimum detectable concentration (MDC). (Wernsperger & Schlosser, 2004).

Integrating the facts that the radioxenon of interest emits a beta or conversion electron in coincidence with an X-ray or gamma-ray and the lack of coincidence events from background, several detectors have been designed to measure coincidence events from radioxenon. These are Automated Radioxenon

Sampler/Analyzer (ARSA) developed at Pacific Northwest National Lab (PNNL) (McIntyre et al., 2001), the Swedish Automatic Unit for Noble gas Acquisition SAUNA developed at the Swedish Research Agency (FOI) (Ringbom, Larson, Axelsson, Elmgren, & Johansson, 2003) and the Russian ARIX (Analyzer of Xenon Radioisotopes) (Prelovskii et al., 2007). In addition, a detector based on high resolution gamma spectrometry called SPALAX (Système de Prélèvements et d'Analyse en Ligne d'Air pour quantifier le Xénon) was developed by the French Atomic Energy Commission (CEA) (Le Petit et al., 2008; Le Petit, Jutier, Gross, & Greiner, 2006). In recent years, Phoswich detectors have also been used as an alternative to simplify radioxenon detection (J. H. Ely, Aalseth, & McIntyre, 2005; Wolfgang Hennig, Tan, Warburton, & McIntyre, 2005).

The ARSA, SAUNA and ARIX radioxenon monitoring instruments use separate scintillation materials (multiple photomultiplier tubes (PMTs)) to detect betas/conversion electrons and gamma/X-rays to reduce unwanted background events. Even though the usage of multiple PMTs increases the sensitivity of the detection instruments, it has made gain matching and calibration cumbersome. For detection systems to be installed at the IMS, power and space limitations should also be considered. These systems should also be efficient in power consumption and should be portable. In the ARSA, SAUNA and ARIX systems, the use of several PMTs and associated readout electronics results in high power consumption and they take large space to be installed. In addition, most of the radioxenon detection systems use large-size and analog radiation spectrometer systems. These problems are alleviated by the use of a phoswich detector viewed by a single PMT and by using a digital pulse processing system.

1.3 Phoswich detectors

A phoswich detector is a combination of two or more scintillation layers optically coupled to a single photomultiplier tube (PMT) in a compact configuration. The multiple layers are specifically chosen to have different material properties in order to differentiate between several interaction scenarios by using pulse processing methods.

Phoswich detectors for radiation detection have been studied by several researchers. (Usuda, 1992; Usuda, Abe, & Mihara, 1994a; Usuda, Abe, & Mihara, 1994b; Usuda, Sakurai, & Yasuda, 1997;Bush-Goddard, 2000) Usuda et al. studied several phoswich arrangements for simultaneous detection of alpha, beta (gamma) and neutrons Discrimination between different pulse shapes were based on pulse rise-time and pulse-height of the signal using analog pulse shape discrimination technique. One phoswich design by Usuda et al. is shown in Fig.1.2.

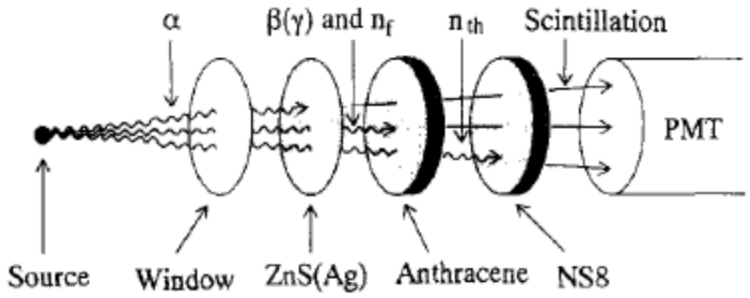

Fig. 1.2: One phoswich detector design by Usuda et al. (Taken from (Usuda et al., 1997)).

White and Miller (1999) and Childress and Miller (2002) developed a triple layer phoswich detector for the discrimination of mixed alpha/beta/gamma radiation field. The three layers used are: ZnS(Ag) for alpha detection, CaF_2(Eu) crystal for

beta detection and NaI(Tl) crystal for gamma detection. The multiple layers are then coupled to a single PMT. Cross-correlation analysis of pulses based on an already built reference pulse was used to discriminate between interaction events. The detector design is shown in Fig. 1.3.

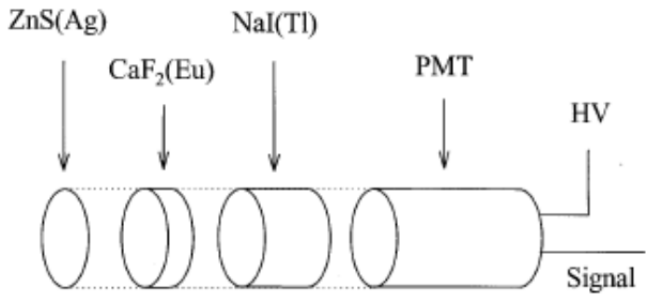

Fig. 1.3: The phoswich detector design for simultaneous detection of alpha, beta and gamma(Taken from (White & Miller, 1999)).

Bardelli et al. (Bardelli, Bini, Poggi, & Taccetti, 2002) developed a triple layer phoswich detector composed of BC404, BC444 and CsI(Tl) coupled to a PMT for identification of fast charged particles. Both analog and digital pulse identification techniques were implemented and compared to optimize the resulting anode output of the PMT. A schematic design of the detector can be seen in Fig. 1.4.

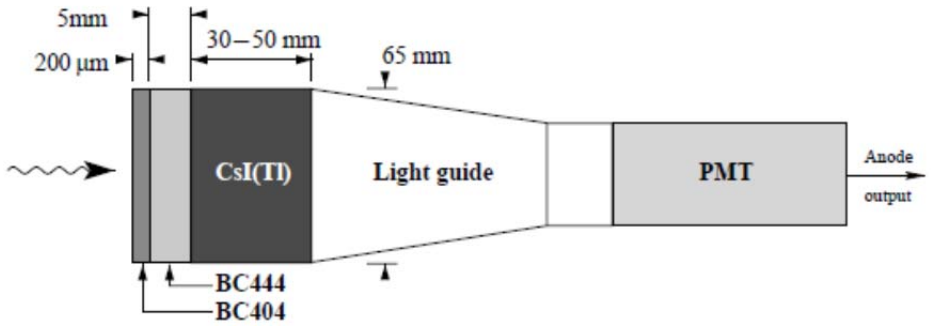

Fig. 1.4: The phoswich detector design by Bradelli et al. (Taken from(Bardelli et al., 2002)

1.4 Radiation detection using scintillators

The phoswich detector developed for this research is based on scintillation detection mechanism. Scintillation detection is the most common method of radiation spectroscopy today (Grupen & Buvat, 2011). Scintillation detection is detection of scintillation light generated from scintillator materials.

1.4.1 The scintillation mechanism

The scintillation mechanism depends on how radiation interacts with the scintillator. When gamma/x-ray interacts with the scintillator they create charged particles. The charged particles then cause atomic or molecular structure excitation in the scintillator. On the other hand, when charged particles interact with the scintillator, they cause direct excitation in the scintillator. The de-excitation process produces light in proportion to the energy deposited within the scintillator. The emitted light will then be detected with light-sensitive devices.

1.4.2 Scintillator types

Scintillator materials are commonly classified into two groups. These are: inorganic and organic scintillators. The classification is based on how scintillation light is produced.

1.4.2.1 Inorganic scintillators

Light emission in inorganic scintillators is based on the crystalline energy band structure of the scintillator. As shown in Fig. 1.5, there are three energy bands commonly called as valence, forbidden and conduction energy band.

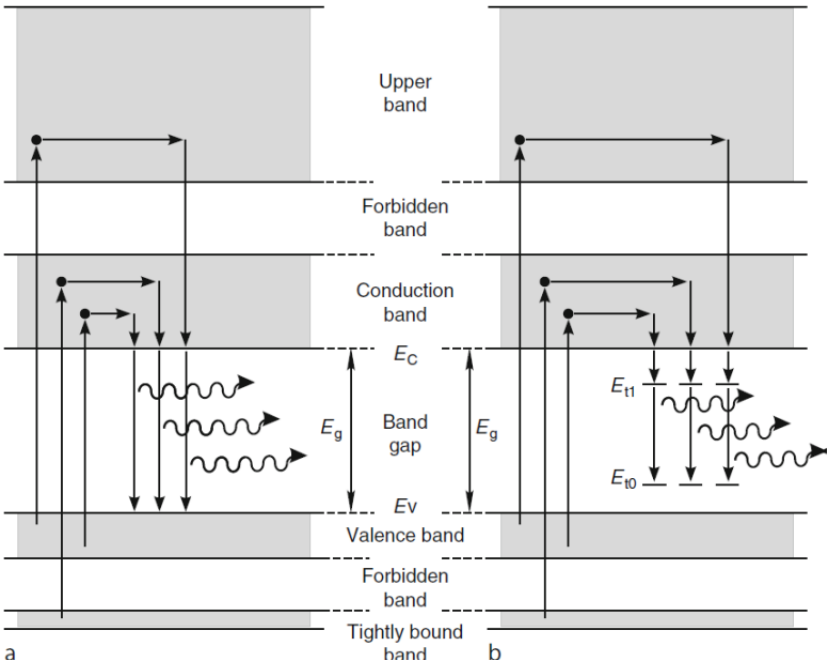

Fig. 1.5: Two methods of light production by an inorganic scintillator: (a) Shows the case for no added dopants and (b) shows the case for an activator dopant added. (Taken from (Grupen & Buvat, 2011)).

When radiation interacts with the scintillator, it excites electrons from the valence band to the conduction band. When the electrons loose energy, they de-excite to the valence band and emit light photons. If the scintillator is intrinsic, these photons will be re-absorbed and again excited to the conduction band. This process results in self-absorption. In order to alleviate this problem, and generate transparent emission, an activator dopant will be added to the crystal. In this case, some of the excited electrons will fall to the excited state of the activator dopant atom. The de-excitation from this atom will have a different frequency than the one de-excited directly from the conduction band. So they will not be re-absorbed.

There are various types of inorganic scintillators in market today designed for many radiation detection applications(McFee, Faust, Andrews, Kovaltchouk, &

Clifford, 2009; van Eijk, 2012; van Eijk, 2003; Weber, 2002). Table 1.1 shows common inorganic scintillators.

Table 1.1: Properties of common inorganic scintillators. (Taken from (Grupen & Buvat, 2011)).

Material	Density(g/cm^3)	Wavelength of maximum emission (nm)	Decay time constant (ns)	Index of refraction	Light yield (photons/MeV)
NaI:Tl	3.67	415	230	1.85	37,700
CsI:Tl	4.51	550	600,3400	1.79	64,800
CsI:Na	4.51	420	630	1.84	38,500
CaF_2:Eu	3.18	435	840	1.47	23,600
^{6}Lil:Eu	4.08	470	1400	1.96	11,000
^{6}Li glass	2.6	390-430	60	1.56	2,000
BaF_2	4.88	315/220	630/0.8	1.50/1.54	10,000/1,400
YAP:Ce	5.55	350	27	1.94	18,000
YAG:Ce	4.57	550	70,300	1.82	19,700
LSO:Ce	7.40	420	40	1.82	30,000
LYSO:Ce	7.10	420	40	1.81	32,000
YSO:Ce	4.55	420	37,82	1.80	45,000
GSO:Ce	6.71	440	56,600	1.85	12,500
BGO	7.13	480	300	2.15	8,200
$CdWO_4$	7.90	470,540	20000,5000	2.3	15,000
$PbWO_4$	8.28	420,425	10, 30	2.20	100, 31
$ZnWO_4$	7.62	490	20000	2.32	9,500
$LaBr_3$:Ce	5.08	280	16	1.9	63,000
$LaCl_3$:Ce	3.85	350	28	1.9	49,000

1.4.2.2 Organic scintillators

The light emission process in organic scintillators is based on transition in the energy level structure of a single molecule. A simplified energy diagram of a molecule can be seen in Fig. 1.6. Energy can be absorbed by exciting molecules into one of the singlet (S_0, S_1) or triplet (T_1, T_2 …) states. Each energy level is separated by a given amount of energy. Each singlet energy level is again subdivided into different levels (S_{00}, S_{01} …) based on the vibrational state of the molecule. When molecules de-excite, they emit scintillation light whose timing depends on the transition process. Prompt fluorescence emission occurs when they de-excite from the Singlet states to the ground. Delayed fluorescence emission occurs when molecules de-excite from the triplet states (Knoll, 2010).

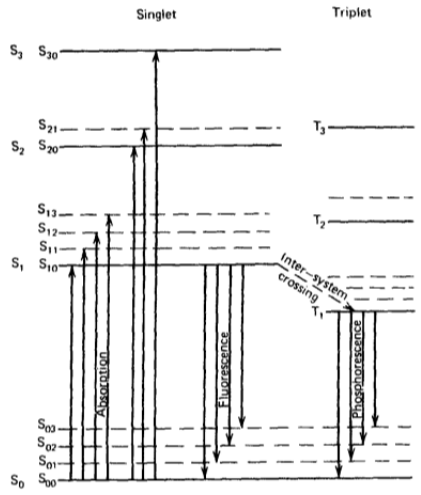

Fig. 1.6: A simplified energy diagram of an organic molecule. (Taken from (Knoll, 2010)).

Organic scintillators are widely used in homeland security, X-ray detectors, charged-particle detectors, heavy-ion detectors, fast- and slow-neutron detection, and electron detectors (Grupen & Buvat, 2011). Table 1.2 shows properties of

commercially available organic scintillators from Saint-Gobain crystals (Saint-Gobain Crystals, 2011).

Table 1.2: Commercially available organic scintillators from Saint-Gobain crystals.

Material	Density(g/cm^3)	Wavelength of maximum emission (nm)	Decay time constant (ns)	Index of refraction	Light yield % Anthracene[a]
BC-400	1.032	423	2.4	1.58	65
BC-404	1.032	408	1.8	1.58	68
BC-408	1.032	425	2.1	1.58	64
BC-412	1.032	434	3.3	1.58	60
BC-414	1.032	392	1.8	1.58	68
BC-416	1.032	434	4.0	1.58	38
BC-418	1.032	391	1.4	1.58	67
BC-420	1.032	391	1.5	1.58	64
BC-422	1.032	370	1.6	1.58	55
BC-422Q	1.032	370	0.7	1.58	11
BC-428	1.032	480	12.5	1.58	36
BC-430	1.032	580	16.8	1.58	45
BC-436	1.130	425	2.2	1.58	52
BC-440	1.032	434	3.3	1.58	60
BC-440M	1.039	434	3.3	1.58	60
BC-444	1.032	428	285	1.58	41
BC-452	1.080	424	2.1	1.58	32
BC-454	1.026	425	2.2	1.58	48
BC-480	1.032	425	-	1.58	-
BC-482A	1.032	494	12.0	1.58	-
BC-490	1.032	425	2.3	1.58	55

BC-498	1.032	423	2.4	1.58	65
[a]Anthracene light output = 40-50% of NaI(Tl)					

1.4.3 Photomultiplier Tubes

The light output from the scintillation crystals is measured by light-sensitive devices. A photomultiplier tube (PMT) is a common light sensing device. The PMT converts light signal into electrical signal. Fig. 1.7 shows a simplified diagram of how a PMT is coupled with a scintillator.

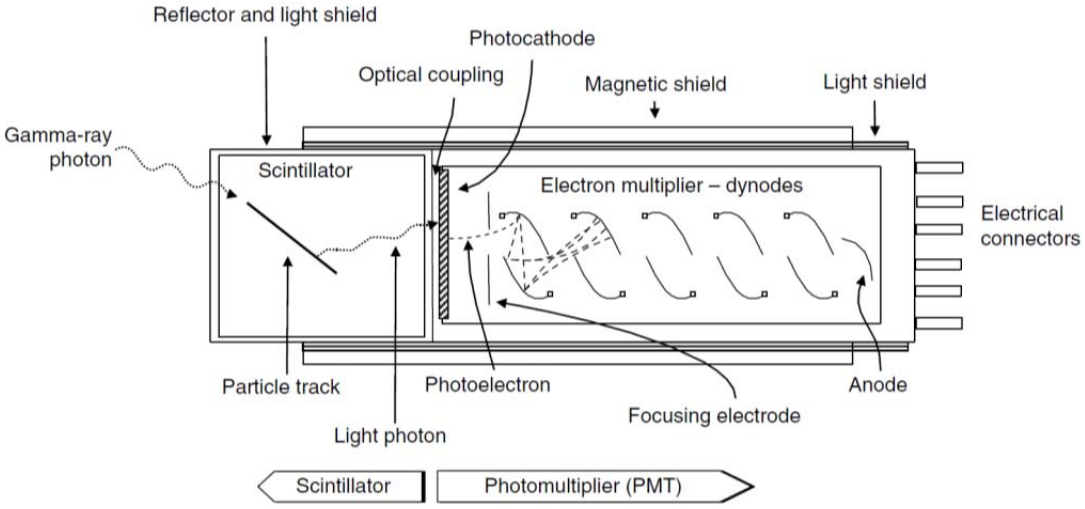

Fig. 1.7: A simplified diagram of the light sensing process in a PMT. (Taken from (Gilmore, 2011)).

The first stage in the conversion is converting the light reaching the PMT window to a photoelectron. This is done by a photocathode. The photoelectron will then be focused on electron multiplying stages (dynodes). The number of dynodes in the

PMT limits the multiplication factor the photoelectrons. The final stage, anode, will collect the amplified signal.

The gain of a PMT is given by:

$$\text{Gain} = \alpha \, \delta^{N} \qquad [1.1]$$

α = The fraction of all electrons collected by the first dynode

δ = Number of electrons liberated for each incident photoelectron at any one dynode

N = Number of dynodes

1.5 Objectives

The main objectives of the work presented in this document are to:

- Develop a well-type phoswich detector to reduce Compton background in radioxenon regions of interest due to unwanted background events;
- Develop a pulse shape discrimination technique and compare it with existing method;
- Characterize the detector in measuring the four radioxenons of interest by activating highly enriched stable xenon gas at the TRIGA reactor of the Oregon State University; and
- Calculate the MDC of the detector for the four radioxenon isotopes and compare it with other radioxenon detectors

2. Survey of Literature

2.1 Radioxenon

There are 18 known radioxenon isotopes produced in nuclear fission with half-lives ranging from less than one second to 11.9 days. Among these isotopes only four (^{131m}Xe, ^{133m}Xe, ^{133}Xe and ^{135}Xe) remain in significant amounts more than a day after a nuclear explosion (Perkins & Casey, 1996). Table 2.1 summarizes the four radioxenon isotopes.

Table 2. 1: Half-lives and characteristic energies for the decay of the four radioxenon(Browne & Firestone, 1986).

Radionuclide	^{131m}Xe	^{133m}Xe	^{133}Xe	^{135}Xe
Half-life	11.93d	2.19d	5.25d	9.14h
Gamma-rays(keV)	163.9	233.2	81	250
Gamma-ray abundance (%)	1.96	10.3	37	90
X-ray, K-shell (keV)	30	30	31	31
X-ray abundance (%)	54.1	56.3	48	5.2
Beta, maximum energy (keV)	-	-	346	905
Beta abundance (%)	-	-	99	97
CE, K-shell (keV)	129	199	45	214
CE abundance (%)	60.7	63.1	54.1	5.7

Few radioxenon monitoring systems are developed or are in the development stages. Radioxenon detection measurements are done either by beta/gamma coincidence spectrometry or high-resolution gamma-spectrometry. Table 2.2 shows the detection instruments and their corresponding detection mechanism.

Table 2.2: Detection Mechanism

Detector type	Detection Mechanism
ARSA	Beta-Gamma coincidence spectroscopy
SAUNA	Beta-Gamma coincidence spectroscopy
ARIX	Beta-Gamma coincidence spectroscopy
SPALAX	High-Resolution Gamma spectroscopy
XIA	Beta-Gamma coincidence spectroscopy
OSU PHOSWICH	Beta-Gamma coincidence spectroscopy

In the next section, the design of these radioxenon detection systems will be reviewed. Because of the limitation of the research, the review mostly focuses on the available radioxenon detection systems.

2.2 Current Radioxenon detection designs

2.2.1 Systeme de Prelevement Automatique en Ligne avec l'Analyse du Xenon (SPALAX)

The SPALAX detector system was designed and developed by the French Atomic Energy Commission (CEA). The system extracts, purifies and concentrates xenon from air. A schematic diagram of the system can be seen in Fig. 2.1.

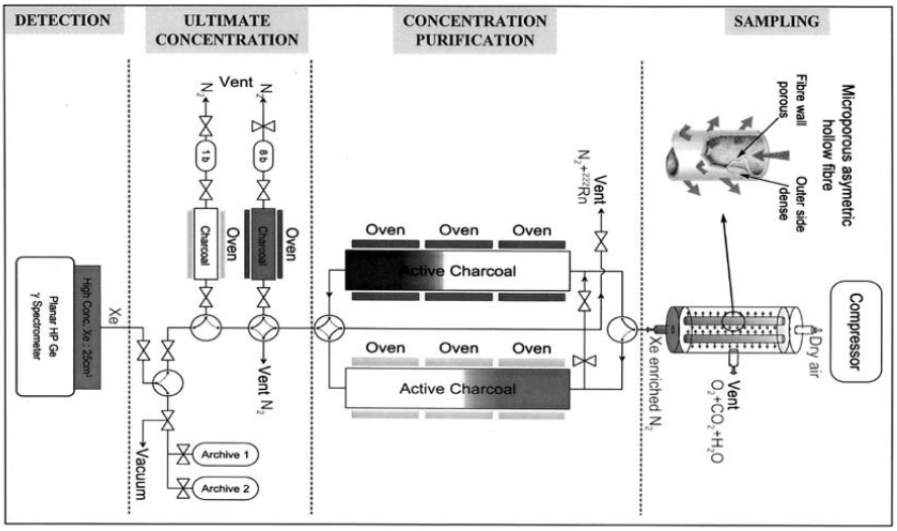

Fig. 2.1: Schematic diagram of the SPALAX detection system (Taken from (Fontaine, Pointurier, Blanchard, & Taffary, 2004)).

In the SPALAX detection system, ^{131m}Xe, ^{133m}Xe, ^{133}Xe and ^{135}Xe are measured by a high resolution broad energy germanium (BEGe) spectrometer. The spectrometer has an active area of 3800 mm^2 and a 1-mm thick aluminum entrance window and covers a wide energy range (15keV-2MeV). The detector is manufactured by the Canberra Company. The detector has a resolution of .54 keV at 30 keV and 0.72 keV at 122 keV (Le Petit et al., 2006; Le Petit et al., 2008). SPALAX is the only radioxenon detection system to date that is based on gamma and X-ray measurements. A typical SPALAX detection system can be seen in Fig. 2.2.

In the SPALAX detection system, the use of a gamma or X-ray only event makes the detection of ^{131m}Xe and ^{133m}Xe cumbersome because of low gamma emission of the isotopes and having the same x-ray energy. Instead, the change in the net count rate at 29.7 keV with time is used to distinguish between the two isotopes. Another problem with the SPALAX system is the occurrence of background events that make the detection of low energies in the region of interest complicated. Aatami

software is used in the spectrum analysis to calculate the background baseline under a spectrum and to construct the desired radioxenon spectrum (Le Petit et al., 2006).

The four radioxenons of interest have separate beta and gamma decay energies. The use of simultaneous beta-gamma measurement is found to be advantageous over the use of gamma- only measurement. The simultaneous beta-gamma measurement further reduces the problem of background interference observed in the SPALAX system by acting as a passive shield in addition to the other active shielding methods that are used. So radioxenon measurement based on beta/gamma coincidence has been introduced.

Fig. 2.2: A typical SPALAX detection system (Taken from ("CEA - Earth and Environmental Science," 2013)) .

2.2.2 Automated Radioxenon Sampler and Analyzer (ARSA) detection system

The ARSA radioxenon monitoring system was designed and built by the Pacific Northwest National Lab (PNNL). The system collects, purifies and quantifies radioxenon. Fig. 2.3 shows the simplified schematic diagram of the design.

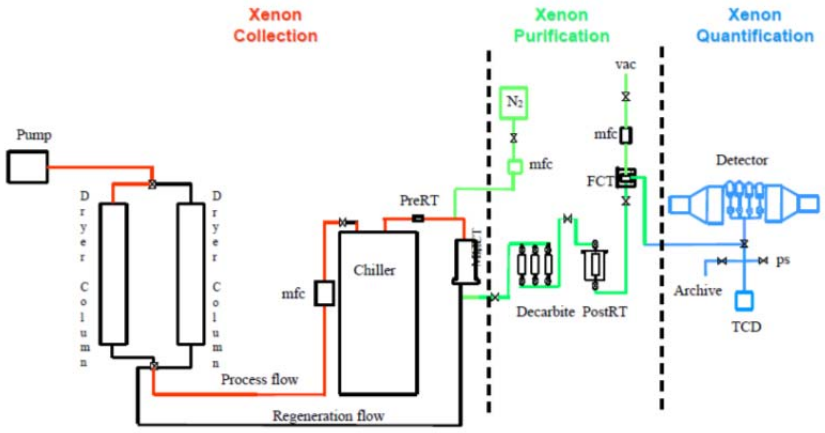

Fig. 2.3: Schematic diagram of the ARSA operation stages (Taken from (Hayes et al., 1999)).

The radioxenon detection consists of four cylindrical plastic cells (BC-404) to detect beta particles and conversion electrons. The plastic cells are also used to contain the xenon gas. The ends of each plastic cell are viewed by two PMTs (Thorn 9078SA, 1.90-cm diameter). The plastic cells have a cylindrical shape with outside dimensions of 5.08-cm length by 1.51-cm diameter and 0.12-cm thick walls and 0.10-cm thick end plugs. This resulted an internal volume of 6.18 cm^3(Bowyer, McIntyre, & Reeder, 1999). The beta cells are surrounded by two rectangular NaI (Tl) crystal planes with a size of 10.16 cm x 17.78 cm x 3.81 cm. Each plane is coupled to two 7.62 cm diameter PMTs to detect gamma rays and X-rays (P. L.

Reeder & Bowyer, 1998). The detection system uses 12 PMTs in total. A simplified ARSA detection system is shown in Fig. 2.4.

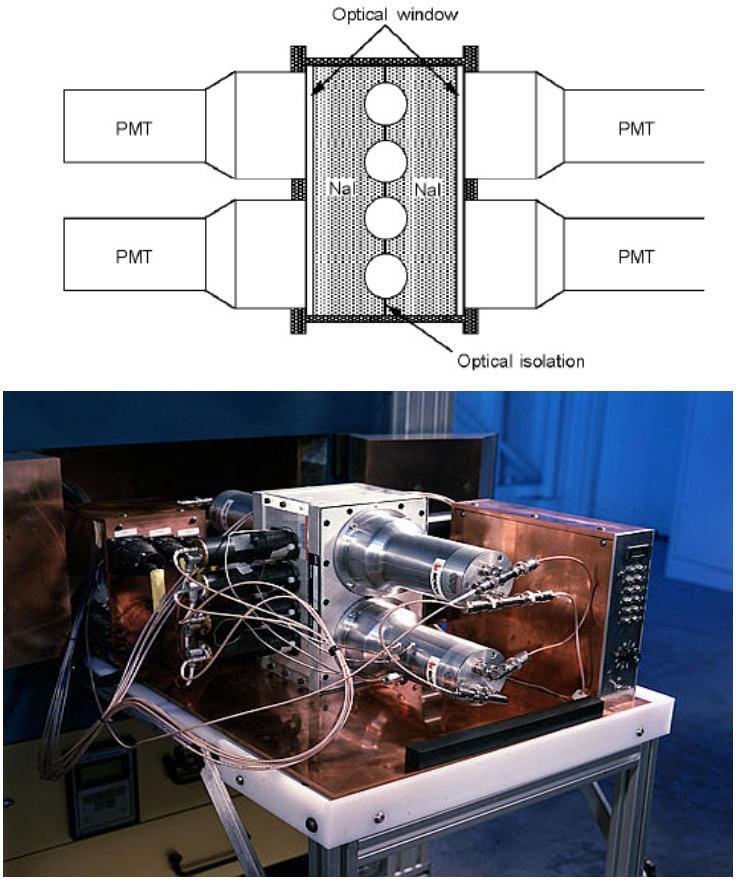

Fig. 2.4: The ARSA spectrometer system (Taken from ("ARSA," 2013; Bowyer et al., 1999)).

In the measurements, a two-dimensional beta/gamma coincidence spectrum was constructed to identify four xenon radioisotopes in coincidence mode. There are three regions in the spectrum from which the concentration of the four xenon radioisotopes can be calculated. These three areas are located at three gamma/x-ray energies; 30, 80, and 250 keV. Fig. 2.5 shows a two-dimensional beta/gamma spectrum from the ARSA system.

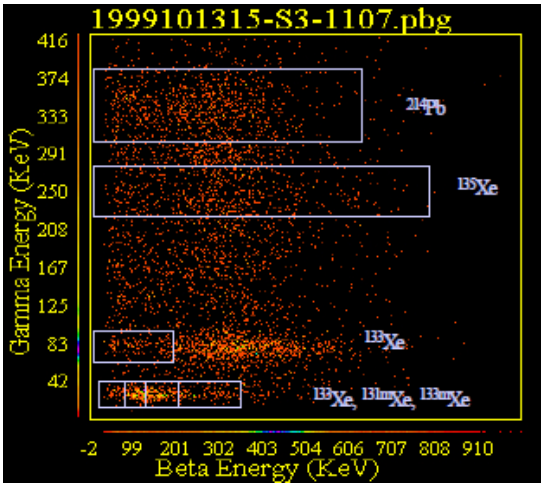

Fig. 2.5: Two-dimensional beta/gamma spectrum from the ARSA system(Taken from (McIntyre, Bowyer, & Reeder, 2006)).

2.2.3 PNNL modified beta-gamma radioxenon detector (BGW detector)

The ARSA design was modified to reduce the problem of gain matching that was caused by the usage of several PMTs. In this design, a single well-type detector of CsI(Na) crystal is used for both X-rays and gamma-rays. The crystal size is 76-mm long by 81.3-mm in diameter, with a well 31-mm wide by 51-mm deep. A single gas cell (2-mm in thickness) coupled with a single PMT (75 mm) (in the previous design, the gas cell contained two PMTs) is used for Beta and conversion electron detection. The gas cell is 28 mm long by 18 mm in diameter, with 2 mm thick plastic scintillation walls and a rounded end. A thin gas transfer tube is placed into a small hole. In this design, there are four individual beta-gamma detectors (called "Quad"detector) separated from each other (Cooper et al., 2007; Cooper, Aalseth, Haas, & Hayes, 2011; Cooper et al., 2005). Fig. 2.6 show one of the four detectors and the partially assembled detector respectively. One advantage of this design is

the ability to calibrate each gamma detector independently, which simplifies the calibration process. Another advantage is the separation of the detectors from one another, which reduces the energy resolution problem. The beta-gamma coincidence spectrum obtained from ^{133}Xe sample with ^{133m}Xe contaminate for the modified detector can be seen in Fig. 2.7.

Fig. 2.6: One of the "quad" beta-gamma detectors and the partially assembled detector (Taken from (Cooper et al., 2011)).

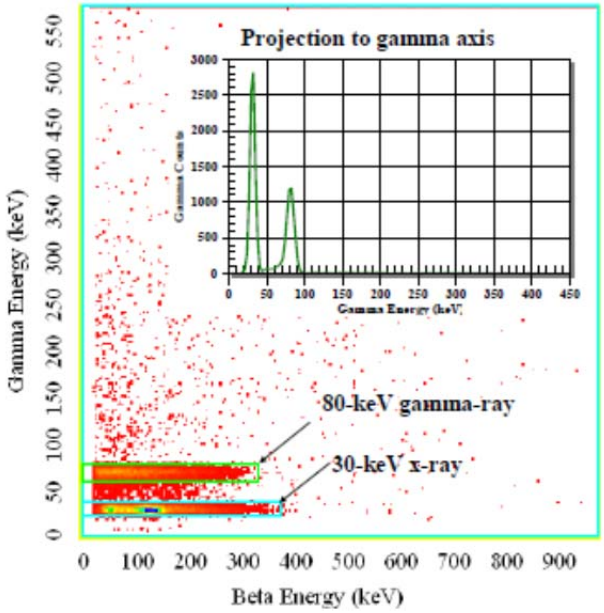

Fig. 2.7: A 2D beta-gamma coincidence histogram obtained from the modified detector. The inset shows a spectrum from the 30-keV x-rays and 80-keV gamma-rays.

2.2.4 The Swedish Automatic Unit for Noble gas Acquisition (SAUNA)

The SAUNA system was developed by the Swedish defense research agency (FOI). The concept of the SAUNA detection system is similar to that of ARSA system. The system has radioxenon sampling, processing, quantification and detection functionality as shown in Fig. 2.8.

The detection system consists of two similar detectors with separate channels to detect beta particles and gamma rays. For beta and conversion electron detection, a BC-404 plastic scintillator is used. It has a volume of 6.4 cm^3, with an inner radius of 0.635 cm, a length of 5.08 cm, and a gas cell thickness of 0.1 cm. Samples are injected into the cell through a stainless steel pipe. The BC-404 is coupled to two PMTs and a cylindrical NaI(Tl) detector. The cylindrical NaI (Tl) detector is coupled with a single PMT for gamma and x-ray detection. The NaI (Tl) detector has a diameter of 10.2 cm and a height of 12.7 cm. The beta detector is placed in a 3.5 cm diameter hole bored inside the NaI (Tl) cylinder. The detector is shielded by a 5 cm thick lead layer and 0.5 cm thick copper layer inside the lead. A simplified SAUNA detection system is shown in Fig. 2.9 (Ringbom et al., 2003).

Fig. 2.8: Sauna detection system (Taken from ("SAUNA Systems - SAUNA II," 2013)).

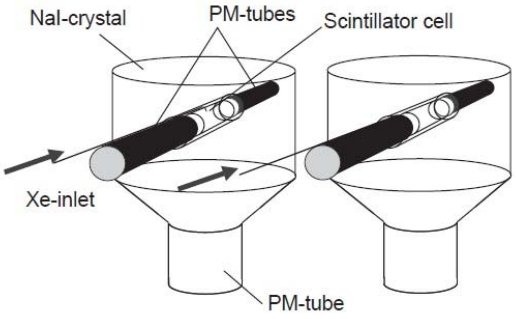

Fig. 2.9: A schematic drawing of the SAUNA detector system used (Taken from (Ringbom et al., 2003)).

Similar to the ARSA detection systems, the SAUNA system uses a two-dimensional beta-gamma energy spectrum to identify xenon radioisotopes. The spectrum was obtained by displaying the NaI(Tl) pulse height versus the summed pulse heights from the two beta cell PMTs. Fig. 2.10 shows a 2D spectrum from a sample containing a mixture of ^{133}Xe and ^{135}Xe.

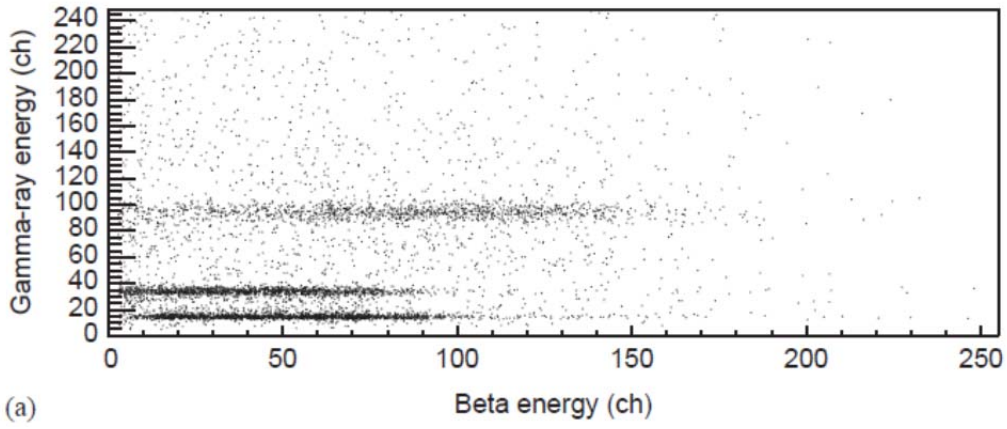

Fig. 2.10: A two-dimensional beta/gamma spectrum from the SAUNA system for an injected sample of a mixture of ^{133}Xe and ^{135}Xe (Taken from (Ringbom et al., 2003))

2.2.5 Russia's Analyzer of Xenon Radioisotopes (ARIX)

The ARIX radioxenon monitoring system was developed at Khlopin Radium Institute, Russia. The system has automatic xenon extraction from air, sample preparation, sample spectrometric analysis and activity measurement (Prelovskii et al., 2007). Schematic flow diagram of the system can be seen in Fig. 2.11. Fig. 2.12 shows the general ARIX system.

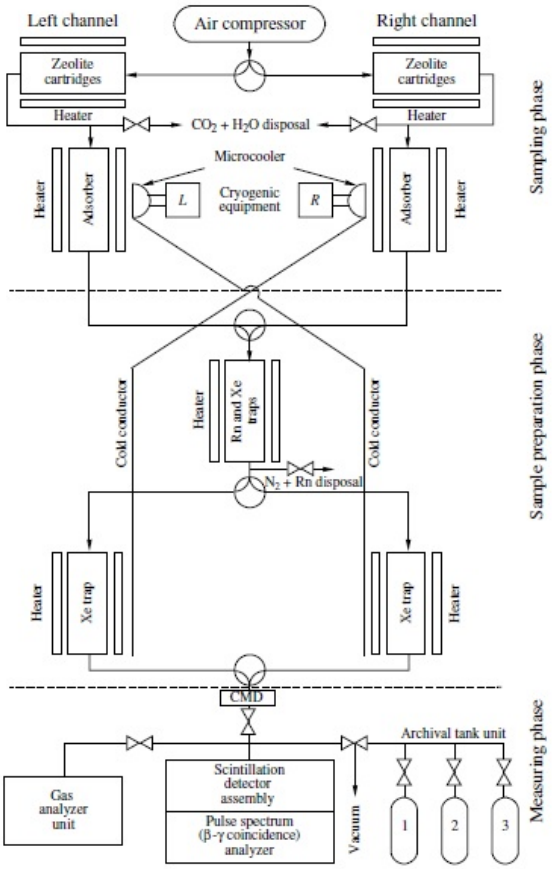

Fig. 2.11: Schematic diagram of the ARIX system (Taken from (Dubasov et al., 2005)).

Fig. 2.12: General ARIX system (Taken from (Dubasov et al., 2005)).

In the detection system a well-type NaI(Tl) crystal is used for gamma and X-ray detection. The crystal has an outside diameter of 4 cm, a height of 3.7 cm, and a well 1.8 cm in diameter and 2.8 cm in depth. Beta particles and conversion electrons are detected using a polystyrene organic scintillator of thickness 0.01 cm applied inside the well surface. The well has a volume of 7.3 cm^3 (Popov, Kazarinov, Popov, Rykov, & Skirda, 2005). The detector design can be seen in Fig. 2.13.

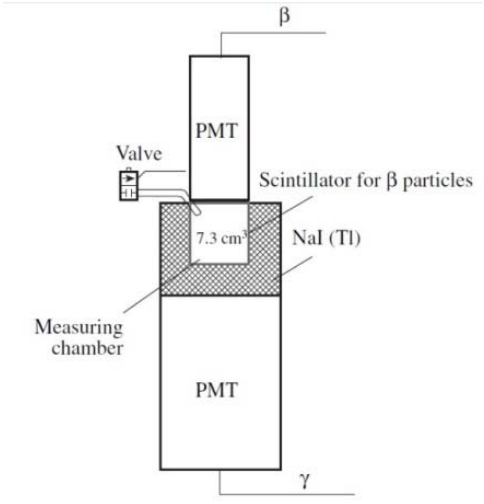

Fig. 2.13: ARIX detector design (Taken from (Popov et al., 2005))

In the earlier ARIX system, the radioxenon detection is based on beta-gated gamma coincidence detection method. The detector only records gamma energy pulse height spectra when it gets a trigger from the beta or conversion electron. So, in order to analytically separate ^{131m}Xe and ^{133m}Xe nuclides, the difference in half-lives are used. This method was changed in the recent ARIX system to beta-gamma coincidence method (Auer, Kumberg, Sartorius, Wernsperger, & Schlosser, 2010).

2.2.6 Phoswich detectors for radioxenon monitoring

2.2.6.1 PNNL phoswich radioxenon detection system

The first approach to use phoswich detector for radioxenon monitoring was made by James H. Ely et al. (J. H. Ely et al., 2005). In this approach, the detector has two layers: A 2x2 inch NaI(Tl) crystal (250 nsec decay time) for gamma radiation and a 0.04 inch thick window of CaF_2(Eu) crystal (940 nsec decay time) for beta radiation. The crystals were made by Saint-Gobain crystals. Due to the hygroscopic nature of NaI(Tl), a 0.25 inch thick quartz optical window was used. One end of the NaI(Tl) crystal was coupled with a PMT (ETI 9266). A hollow cylindrical aluminum was used to hold the radioxenon gas. ORTEC 276 single-unit PMT base with preamp, PMT high voltage and signals were connected to a NIM crate. Pulses were then processed by an XIA DGF4C digital pulse processor.

Pulses were discriminated based on the amount of time the pulses took to reach from 10% to 90% of the maximum height (pulse rise-time) and also with respect to energy and the results were plotted as shown in Fig. 2.14.

The discrimination method used showed that it was possible to discriminate between single events or pulses created in either of the scintillators. But it was not easy to discriminate coincident events (pulses created from both layers simultaneously) in this method.

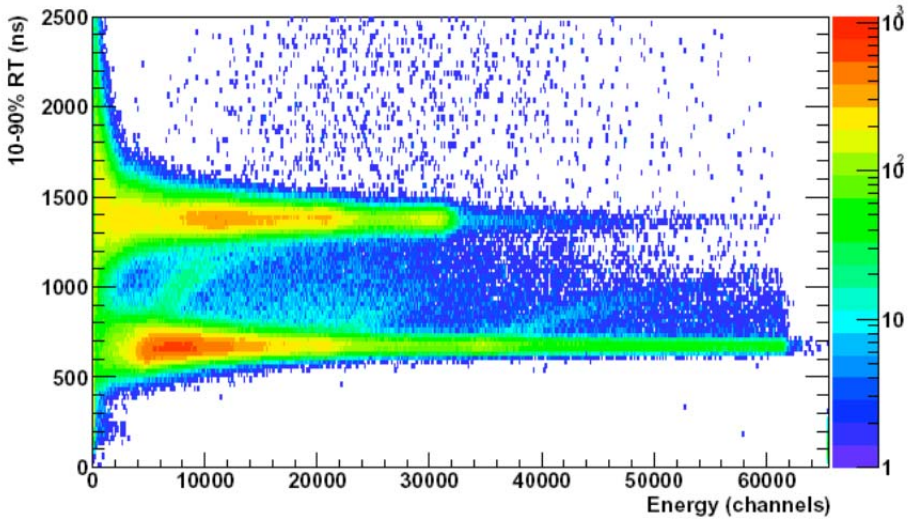

Fig. 2.14: Result of the pulse shape discrimination method for xenon pulses (Taken from(J. H. Ely et al., 2003)).

2.2.6.2 XIA single channel beta-gamma coincidence detection (PhosWatch)

The PhosWatch system developed by XIA has simplified the use of separate beta and gamma scintillation channels by introducing a single phoswich detector with pulse shape analysis for coincidence detection. The detector consists of a BC-404 plastic (1 mm thick, 25.4 mm diameter) disk to absorb beta and conversion electrons. The plastic scintillator is then optically coupled to a 25.4 mm long cylinder of CsI(Tl) crystal. The crystal is used to absorb both x-rays and gamma rays. The BC-404 and CsI (Tl) are viewed by a single PMT which is connected to an XIA DGF Pixie-4 digital pulse processor. Total energy of each acquired pulse was calculated by using a digital trapezoidal filter of rise time ~7 μs implemented in a field programmable gate array. To discriminate between single and coincidence events, signal rise time and different filter sums were calculated for each pulse as

shown in Fig. 2.15 in offline mode (W. Hennig, Tan, Warburton, & McIntyre, 2006).

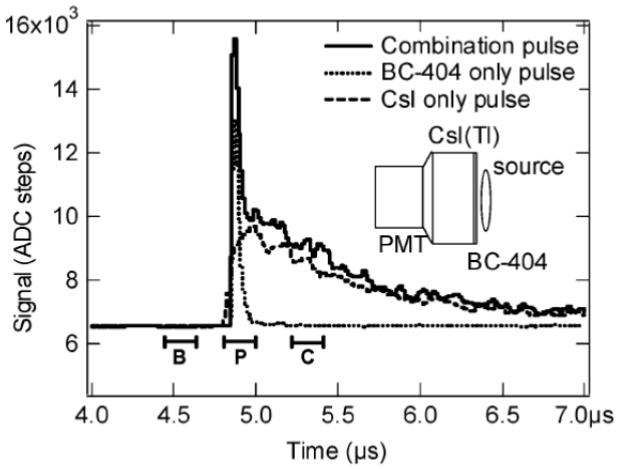

Fig. 2.15: Different pulse types from the phoswich detector using a Co-60 source (Taken from (W. Hennig et al., 2006)).

The results were then used to discriminate between single (CsI(Tl) or BC-404) and combination events as shown in a two-dimensional plot of Fig. 2.16. The result showed three different regions based on the layer at which energy deposition occurred.

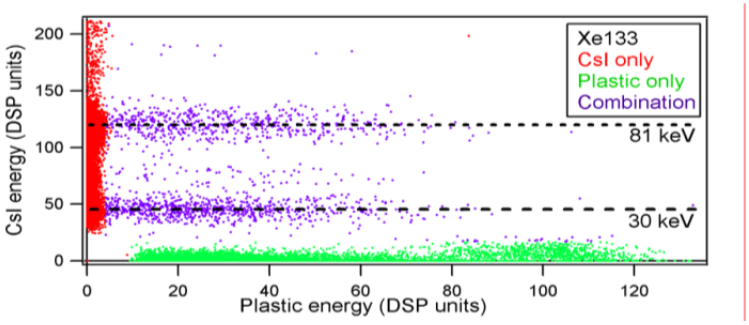

Fig. 2.16: A 2-D energy scatter plot for data acquired with a Xe-133 source. The vertical and horizontal axis represents single CsI and plastic events respectively. Coincidence events form horizontal bands at characteristic x-ray or gamma ray energies with varying beta energy (Taken from(Wolfgang Hennig et al., 2005)).

2.2.6.3 First generation OSU phoswich detection system

The detector consists of a thin hollow disk that is 2 mm in thickness and 76.2 mm in diameter as the radioxenon gas cell. The gas cell is surrounded by two identical planar triple-layer phoswich detectors. An aluminum sleeve is used to join the two detectors. The phoswich detector is designed with three scintillation layers: BC-400 (~ 2.4 ns decay constant) to detect beta particles and CE, CaF_2 (~ 900 ns decay constant) for 30 keV x-ray detection and NaI(Tl) (~ 230 ns decay constant) for gamma-ray detection. The thickness of the BC-400, CaF_2 and NaI(Tl) are 1.5, 2.0 and 25.4 mm, respectively. Because the NaI(Tl) crystal is highly hygroscopic, a quartz window (6.35 mm in thickness) separates the NaI(Tl) layer from the CaF_2 layer. Fig. 2.17 shows a schematic diagram of the detector.

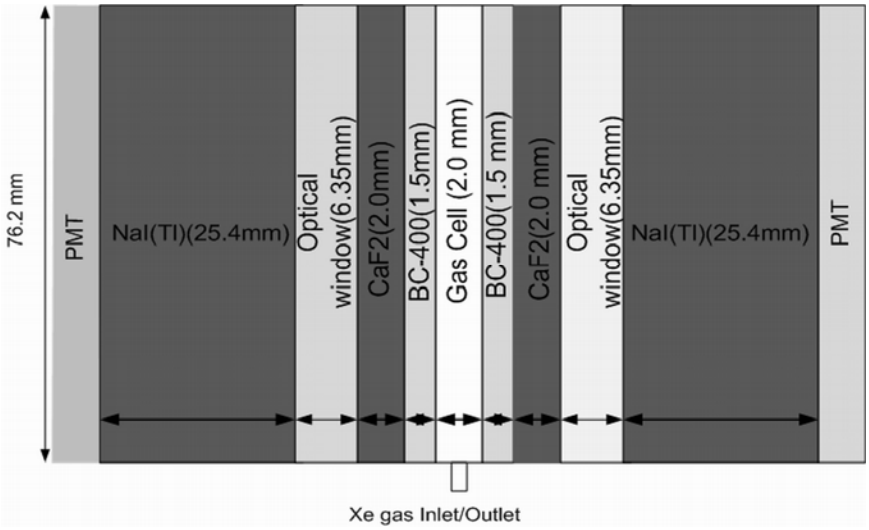

Fig. 2.17: Schematic diagram of a two-channel triple layer phoswich detection system (Taken from (Abi T. Farsoni, Hamby, Ropon, & Jones, 2007)).

The design is based on a triple coincidence pulse processing method to improve background reduction. In this method eight possible triple-coincidence scenarios are divided into two scenario groups as seen in Fig. 2.18. In one group, beta

particles and conversion electrons are detected in the same phoswich and in the other group, the beta particle is detected by one phoswich and the conversion electron is detected by the other phoswich. In one group, beta particles and conversion electrons (45 keV) are absorbed in a single phoswich and cannot be separated, thus the resulting pulse from the beta layer is recorded in the beta spectrum. In the second group (scenarios 5 to 8), the beta particle and conversion electron are absorbed in opposite phoswich detectors; thus, they can be separated when a triple event is identified and confirmed by detecting a 30 keV x-ray in one of two phoswich detectors. This leads to rejection of the beta event while the CE event is recorded in the beta spectrum, resulting in reduction of the beta-background (Abi T. Farsoni et al., 2007).

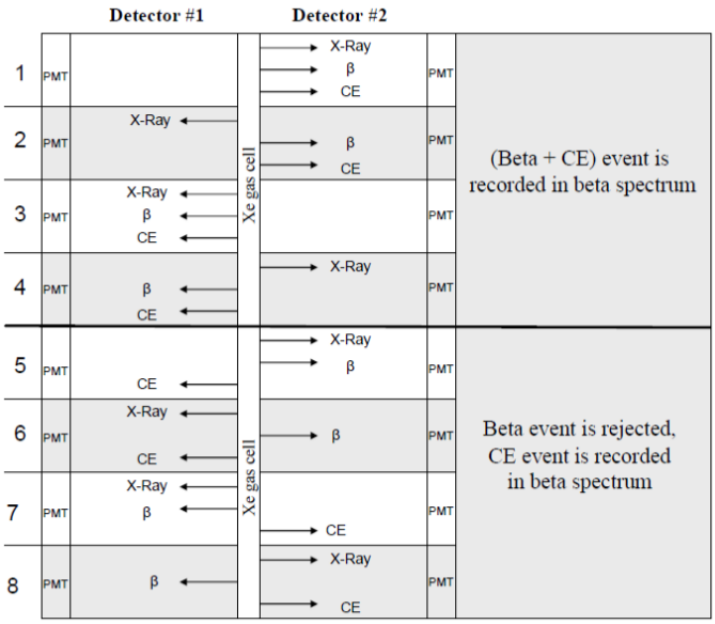

Fig. 2.18: The eight scenario groups in the two-channel phoswich detector (Taken from (Abi T. Farsoni et al., 2007)).

Coincident events are discriminated from single events using digital pulse shape analysis. Based on how incident radiation releases energy on each scintillator, seven possible pulse types are generated from the anode output of the PMT. These

pulse types are separated using three digital trapezoidal filter sums to calculate fast component ratio and slow component ratio. A scatter plot of the ratios is used to identify single or coincident events as shown in Fig. 2.19. (Abi T. Farsoni, Hamby, Lee, & Elliot, 2008; Abi T. Farsoni et al., 2007; Abi T. Farsoni & Hamby, 2009). Coincident events are then used to plot a two-dimensional beta/gamma coincidence and identify the different radioxenon as shown in Fig. 2.20 (Abi T. Farsoni & Hamby, 2010a).

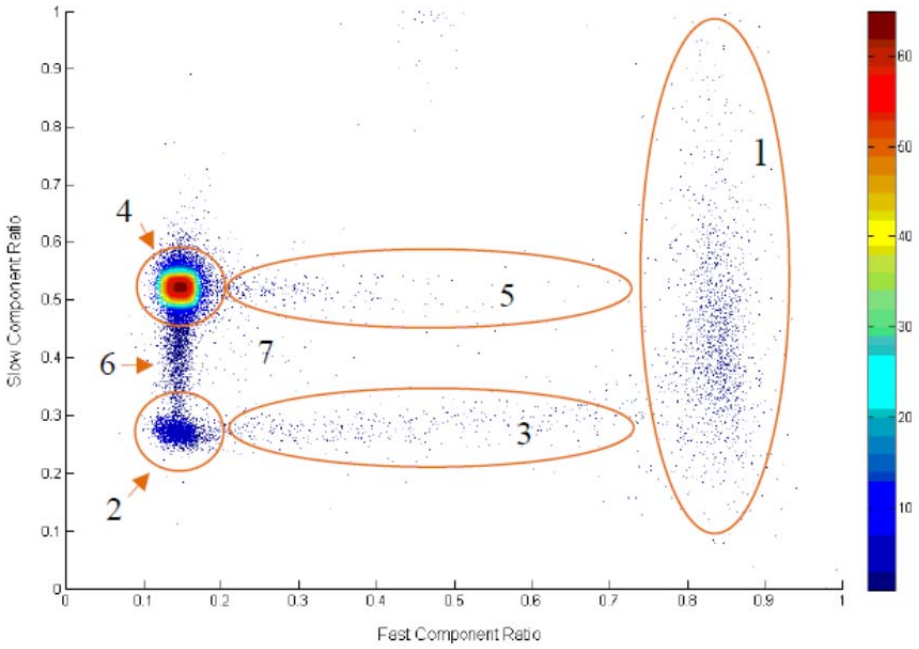

Fig. 2.19: Scatter plot of fast component ratio versus slow component ratio. Regions 1, 2 and 4 represent single events. Regions 3, 5, 6 and 7 represent coincidence events (Taken from(Abi T. Farsoni & Hamby, 2009)).

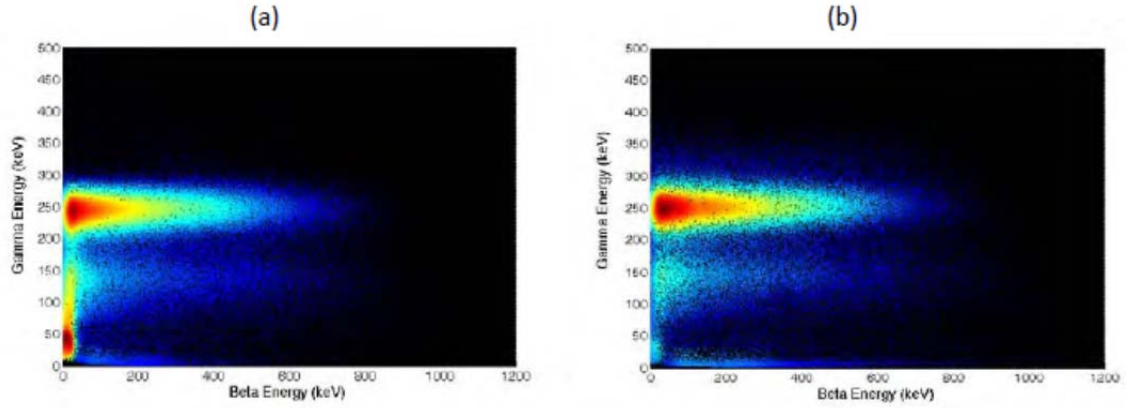

Fig. 2.20: Two-dimensional beta gamma coincidence energy histograms from ^{135}Xe in phoswich 1 (a) and phoswich 2 (b) of the two-channel phoswich detector (Taken from (Abi T. Farsoni & Hamby, 2010a)).

2.2.6.4 Second generation phoswich detection system

Even though the beta/gamma coincidence detection system enhances the identification of radioxenon, it showed high background interference in the radioxenon energy range of interest. This interference is primarily due to the probability of high-energy gamma-rays Compton scattering in the detector.

The second generation OSU phoswich detection system, called the Actively-Shielded Phoswich Detector (ASPD), tried to address the problem of Compton scattering interference observed by integrating a Compton suppression capability into the phoswich detector system (Abi T. Farsoni & Hamby, 2010b). The suppression is done by surrounding a CsI(Tl) scintillator with a high-density BGO crystal. The detector has three scintillation layers: BC-400 for beta and conversion electrons detection, CsI(Tl) crystal for gamma-rays and X-rays detection and BGO

crystal to identify scattered photons and to shield the CsI(Tl) crystal from external background gamma-rays. Schematic diagram of the design can be seen in Fig. 2.21.

Anode pulses from the detector is processed digitally using a FPGA-based user-programmable digital spectrometer (Abi T. Farsoni, Alemayehu, Alhawsawi, & Becker, 2013). Coincidence and single events are discriminated using digital pulse shape analysis method similar to the one used in the first generation.

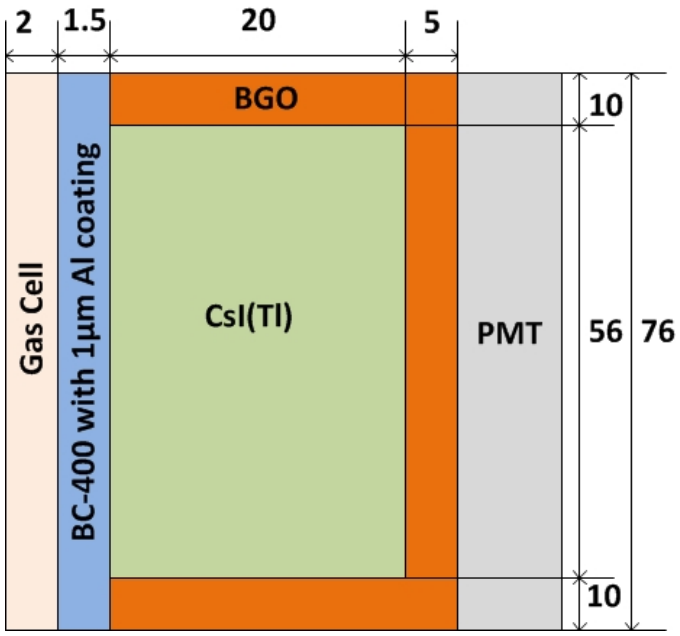

Fig. 2.21: Schematic diagram of the Compton suppressed phoswich design. All dimensions are in mm.

2.3 Minimum detectable concentration (MDC)

The basic requirement of the International Monitoring System (IMS) is to have a high sensitivity for radioxenon detection systems. Environmental factors reduce the

concentration of radioxenon when it reaches detection systems; therefore, detectors that are used for radioxenon measurement should be highly sensitive to low concentrations of radioxenon. This sensitivity is measured in terms of detector's minimum detectable concentration (MDC). The minimum requirement for any CTBT radioxenon system is an MDC of less than or equal to 1 mBq/m^3 for ^{133}Xe.

According to the MDC definition stated in (Currie, 1968; McIntyre et al., 2006),

for the beta-gamma detector systems the MDC for a single radioxenon isotope is typically calculated as:

$$MDC\left(\frac{mBq}{m^3 air}\right) = \frac{2.71+4.65\sigma_0}{\varepsilon_\gamma \varepsilon_\beta \gamma_{BR} \beta_{BR}} \frac{\lambda^2}{(1-\exp(-\lambda T_c))\exp(-\lambda T_P)(1-\exp(-\lambda T_A)} \cdot \frac{T_c * 1000}{V_{air}} \quad [2.1]$$

where

$\sigma_0 = \sqrt{Background\ Counts}$

$\varepsilon_\gamma =$ γ efficiency

$\varepsilon_\beta =$ β efficiency

$\gamma_{BR} =$ γ branching ratio

$\beta_{BR} =$ β branching ratio

$\lambda = \ln(2)/t_{1/2}$

$T_c =$ Xenon Collection Time

$T_P =$ Processing Time of Gas

$T_A =$ Acquisiton Time of Counts

$V_{air} =$ cc of Xenon / 0.087 cc of Xenon per m^3 air

To reduce the MDC, background uncertainty (σ_0) can be reduced (by extending the count time or reducing the overall background), the detector γ and β efficiencies

can be increased, Xenon collection time can be reduced or the volume can be increased(J. Ely et al., 2012). Table 2.3 lists the measured MDCs of the reviewed systems, which range between 0.11-0.5 mBq/m^3. This sensitivity is in agreement with CTBT requirements.

Table 2.3: Minimum detectable concentration.

Detector type	**Minimum detectable concentration for ^{133}Xe (MDC)**
SPALAX	0.11 (Le Petit et al., 2008)
ARSA	0.50 (Foltz Biegalski & Biegalski, 2001)
SAUNA	0.18 (Wolfgang Hennig et al., 2011)
XIA	0.5 (Wolfgang Hennig et al., 2009)

2.4 Memory effect

Except for the SPALAX system, the radioxenon detection systems use plastic scintillators for beta ray and conversion electron detection. In this common design, the xenon sample diffuses into the plastic material and remains there even after evacuation using a vacuum pump. This persistence causes the memory effect, which increases the background count and the minimum detectable concentration (MDC) of any subsequent measurements. When a high xenon background is present, which is common around most nuclear facilities, this effect has a major contribution to the sensitivity reduction of the systems. The SPALAX system does not experience the memory effect because of its aluminum gas cell.

Two methods were employed to reduce the memory effect. In the first approach, a background measurement is taken before each sampling and subtracted from each

sample measurement. This approach is inefficient and time consuming. It also affects the MDC measurement. Another approach uses a plastic coating to reduce the diffusion of xenon gas into the plastic. Studies have investigated the efficacy of coating the plastic with aluminum (Bläckberg et al., 2011; Seifert et al., 2005). Various aluminum coatings were tested to mitigate the memory effect. In one of those studies, a 425 nm Al_2O_3 coating reduced the diffusion of xenon into the plastic by a factor of 100.

3. Experimental Setup

3.1 Well-type Compton Suppressed Phoswich Detector

The ASPD described in section 2.4.6.4 has low detection efficiency due to its geometry: at least half of all beta and gamma radiation from the source does not interact with the detector. To maximize the efficiency, a well-type actively-shielded phoswich detector (hereafter called WASPD) with Compton suppression capability and beta-gamma coincidence technique has been designed with three scintillation layers having different decay times: A 15mm-diameter BC-400 (decay time: ~2.4 ns) to contain radioxenon gas and to detect beta and conversion electrons. BC-400 is enclosed by a 20 mm diameter CsI(Tl) crystal (decay time: ~1000 ns) to measure x-rays and gamma rays. In order to have Compton suppression capability, the CsI(Tl) was surrounded by a 56 mm diameter BGO crystal (decay time: ~300 ns.) Fig. 3.1 shows schematic diagram of the design. Table 3.1 shows the properties of the scintillators used in the design.

Table 3.1: Properties of the scintillator materials used in the design.

Material	**Density(g/cm^3)**	**Wavelength of maximum emission (nm)**	**Decay time constant (ns)**	**Index of refraction**	**Light yield (photons/MeV)**
BC-400	1.032	423	2.4	1.58	65
CsI(Tl)	4.51	550	1000	1.79	64800
BGO	7.13	480	300	2.15	8200

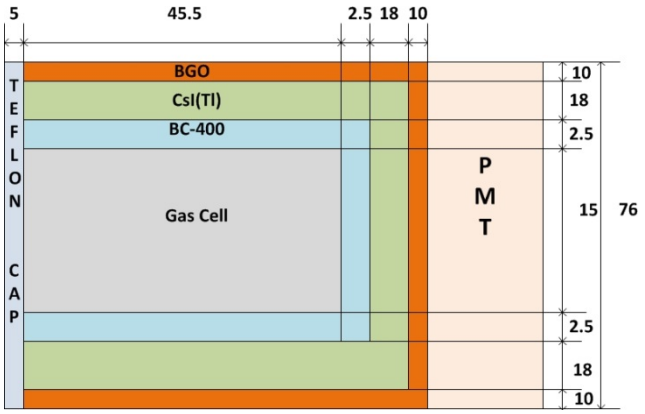

Fig. 3.1: Schematic diagram of the well-type phoswich detector design. All dimensions are in mm.

The BGO crystal has a high density (7.13 g/cm^3) and is usually used for Compton suppression (De Voigt et al., 1995; A. T. Farsoni, Alemayehu, Alhawsawi, & Becker, 2012). The Compton suppression capability is expected to reduce the Compton continuum in the regions of interest of radioxenon gamma ray and improve the minimum detectable concentration (MDC). The BGO is also used as a shield for the CsI(Tl) crystal. The crystals were ordered from Saint Gobain crystals and PMT (R1166) was ordered from Hamamatsu Corporation. Fig. 3.2 shows the crystals and PMT received.

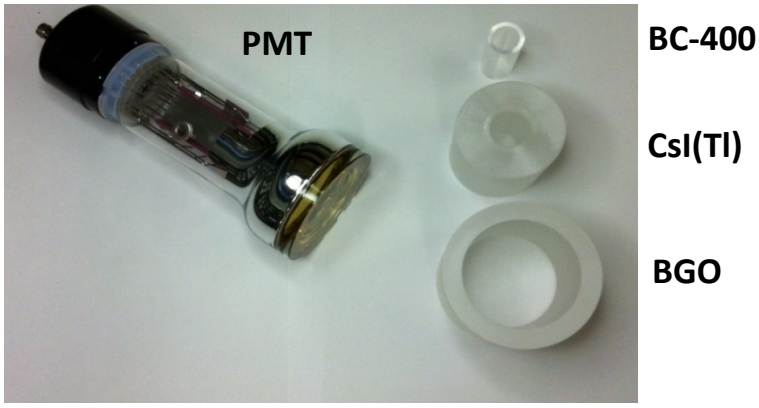

Fig. 3.2: Well-type scintillators and PMT before assembly.

Assembly of the WASPD begun by smearing a layer of silicone grease (BC-630, Saint-Gobain Crystals) for optical coupling between BC-400, CsI(Tl), BGO and PMT. For light reflection, the PMT and scintillators were then wrapped with several layers of Teflon tape (BC-642 PTFE Reflector Tape, Saint-Gobain crystals). The PMT and scintillators were then wrapped with plastic to maintain the integrity of the assembly. At last, the whole assembly was placed and fastened inside a custom-made housing. Fig. 3.3 shows the final assembly.

3.2 MCNP simulations

A Monte Carlo analysis using the MCNP5 code was performed to simulate Beta/CE and Gamma/X-ray interaction probability in the different scintillation layers Fig. 3.1. The results were used to estimate the Beta/CE (ε_β) and Gamma/X-ray (ε_γ) efficiency of the detector. The coincidence detection efficiency ($\varepsilon_\beta * \varepsilon_\gamma$) was then calculated for each region of interest (ROI) (Table 3.2.) The coincidence detection efficiency was later used to estimate the minimum detectable concentration (MDC) of the detector for each xenon radioisotopes.

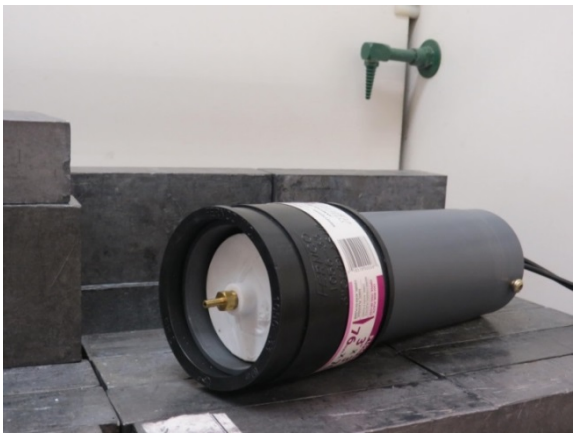

Fig. 3.3: Detector assembled and placed in a custom designed housing.

Table 3.2: Radioxenon region of interest used in the simulation.

Radioxenon	Region of interest(ROI)
^{131m}Xe	31 keV X-rays + 129 keV CEs
^{133}Xe	31 keV X-ray + 346 keV beta
	81 keV gamma + 346 beta
^{133m}Xe	31 keV X-rays and 199 keV CEs
^{135}Xe	250 keV gamma + 910 keV beta

The detector geometry (Fig. 3.1) was constructed in MCNP5. Material composition values were taken from (Williams III, Gesh, & Pagh, 2006). Input decks were constructed for the following radiation sources: 31 keV X-ray, 81 and 250 keV gamma-rays, 129 and 199 keV conversion electrons (CEs) and 346 and 910 keV betas. An example input deck can be seen in Appendix A and Appendix B. The source was distributed in the entire gas cell. This was done by setting the source position to the bottom of the gas cell and using the RAD, AXS, and EXT cards to define the radial distribution, axis of extent, and axial distribution respectively. For each input deck, pulse height tally (F8) was used. The F8 tally gives energy distribution of light pulses created in each scintillation layer for a given energy bins. The tally was used to model the interaction probability of radioxenon isotopes in BC-400 (electron mode) and CsI(Tl) scintillation layers (Photon mode). All simulations were run for 10^7 events. For all calculations a threshold of 20 keV was used. The source cell was modeled as a 2:1 xenon-nitrogen mix.

Table 3.3: Simulation results for the radioxenon ROIs.

Decay energy (keV)	**CsI(Tl) interaction probability**
31 keV (γ)	(86.0±1.0)%
81 keV (γ)	(84.2±1.0)%
250 keV (γ)	(70.0±1.4)%
	BC-400 interaction probability
45 keV (CE)	(36.5±2.3)%
129 keV (CE)	(89.9±3.5)%
199 keV (CE)	(91.3±7.4)%
346 keV (beta)	(89.6±4.3)%
910 keV (beta)	(94.2±8.6)%

The coincidence detection efficiency for the radioxenon coincident decays was calculated by taking the product of X-ray/gamma interaction probability with Beta/CE interaction probability for each ROI. The result can be seen in Table 3.4.

Table 3.4: Coincidence detection efficiency

Isotope	**Coincident decays**	**Coincidence detection efficiency (simulation)**
^{131m}Xe	31 keV X-rays and 129 keV CE	(73.0±3.0)%
^{133}Xe	31 keV X-ray + 346 keV beta	(77.1±3.8)%
	81 keV gamma + 346 beta	(75.4±3.7)%
^{133m}Xe	31 keV X-ray and 199 keV CE	(78.5±6.4)%
^{135}Xe	250 keV gamma + 910 keV beta	(65.9±7.4)%

3.3 Gas transfer system

To test the detector for measuring xenon radioisotopes ^{131m}Xe, ^{133m}Xe , ^{133}Xe and ^{135}Xe , stable and highly enriched (>99%) isotopes of ^{130}Xe, ^{132}Xe , and ^{134}Xe were purchased from ISOFLEX USA. Fig. 3.4 shows the stable gas vessels.

To activate the stable xenon gas, a simple and low-cost gas transfer method was designed and used. Stable gas was first transferred from the gas vessel to a polypropylene syringe as shown in Fig. 3.5. The polypropylene syringe was chosen because of its low activity after neutron irradiation.

Fig. 3.4: Highly enriched stable ^{130}Xe, ^{132}Xe, and ^{134}Xe purchased from ISOFLEX USA.

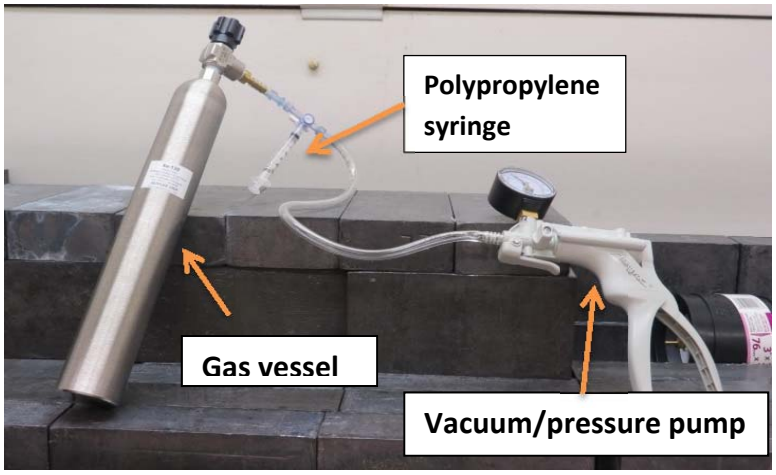

Fig. 3.5: An example of ^{130}Xe gas transfer from the vessel to a polypropylene syringe

The syringe was then activated in the thermal column of the Oregon State University's TRIGA reactor to get ^{131m}Xe, ^{133m}Xe , ^{133}Xe and ^{135}Xe . Lastly, the activated xenon gas was injected into the detector gas cell as shown in Fig. 3.6.

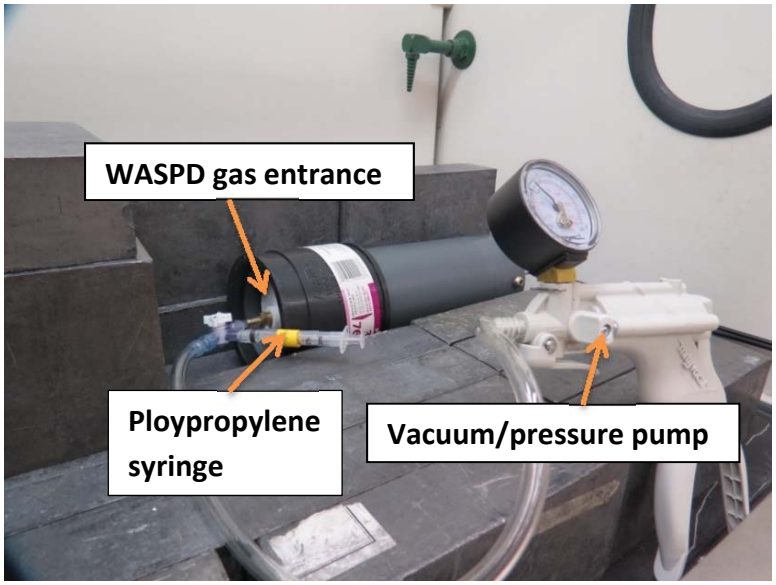

Fig. 3.6: Activated gas in the polypropylene gas is injected into the detector gas cell.

3.4. Digital Pulse Processor

3.4.1 Digital pulse processor (RX1200)

Anode pulses were processed using a user-programmable digital pulse processor (RX1200, Avicenna Instruments, LLC). Fig. 3.7 shows the schematic design of the RX1200.

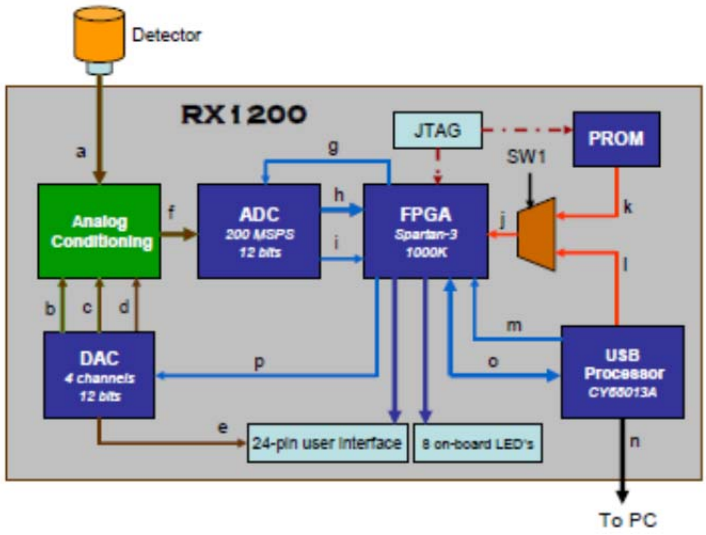

Fig. 3.7: Schematic diagram of the RX-1200.

The digital pulse processor has an input (a) to receive analog signals from a detector and several signal processing chains that transfers data (n) to the PC side. The first stage in the signal processing chain is analog conditioning. It is an electric circuitry (module) which adjusts the signal to bring it to the dynamic range of the ADC (Analog to Digital converter).

The basic precondition before sampling a signal by an ADC is fulfilling the Nyquist theory (sampling rate of ADC should be larger than two times the

maximum frequency of the signal). The ADC on board can sample signals with a maximum frequency of 200 MSPS (Mega samples per second) (an interval of 5 nsec between two samples) and has 12 bits resolution. For a 200 MHz sampling frequency, the ADC input signal shouldn't have frequencies higher than 100 MHz. So the major task in the analog conditioning is to cut those higher frequencies. The frequency cut-off in the analog condition is 90 MHz.

The analog conditioning is controlled by three signals from the DAC on board. The first signal (b) is the gain adjustment signal. This signal controls the variable gain of the amplifiers inside the analog conditioning. Another adjustment that can be done in analog conditioning is controlling the input offset. This is controlled by the input offset adjustment signal (c). The third signal, ADC offset adjustment signal (d), controls the ADC offset. The DAC analog output signal (e) is used to adjust high voltage. This signal is one of the pins in the 24-pin user interface on board.

The filtered and amplified analog signal will be fed to the ADC. At this stage, there is no pulse processing except Nyquist filtering. At the ADC, signals will be sampled every 5 nsec. The input clock for the ADC (g) is provided by the FPGA. At the output of ADC will be a digital data output (h) and ADC clock output (i). The output ADC digital data is synchronized with its ADC clock output. All ADC input and output signals are LVDS (Low Voltage Differential Signal). LVDS is used to reduce sensitivity to noise when using a low voltage and high frequency. In the field-programmable gate array (FPGA), the differential signaling will be converted to single signal (one wire for each bit).

FPGA receives 12 bit data bus from the ADC. The FPGA can be programmed in 3 different ways. The first one is external prom memory on board. All designs can be downloaded to this memory and be there permanently. Any time when the system is powered up, the FPGA file in PROM will automatically configure the FPGA. The other way of programming the FPGA is using a USB port. The switch on

board determines to power the FPGA from prom or USB port. Another method of programming the FPGA is using a JTAG port. In this research work, the FPGA is programmed using the USB port.

The data from FPGA (o) will be read using the USB port and will be sent to PC (n) application program based on the USB clock output (m).

For troubleshooting and prototyping, the RX1200 has two features. One of them is LEDs. The processor has 8 on-board LEDs. These LEDs can be connected to any signal inside the FPGA. When there are signals which have very fast transitions to be monitored using LEDs, a 24-pin user interface on board can be used.

3.4.2 Pulse shape discrimination

To discriminate the different types of the anode output pulses and to calculate the corresponding energy, two different off-line pulse shape discrimination and energy measurement methods have been tested using MATLAB. The programs used can be seen in Appendix C and Appendix D.

3.4.2.1 Fast and slow component ratio (FCR and SCR) pulse shape discrimination method

In the FCR and SCR pulse shape discrimination method (Abi T. Farsoni et al., 2008), single and coincident events were discriminated using three digital triangular filters with different peaking times. Using these filters, the integration of three areas of the anode pulse, A, B and C are calculated as shown in Fig. 3.8.

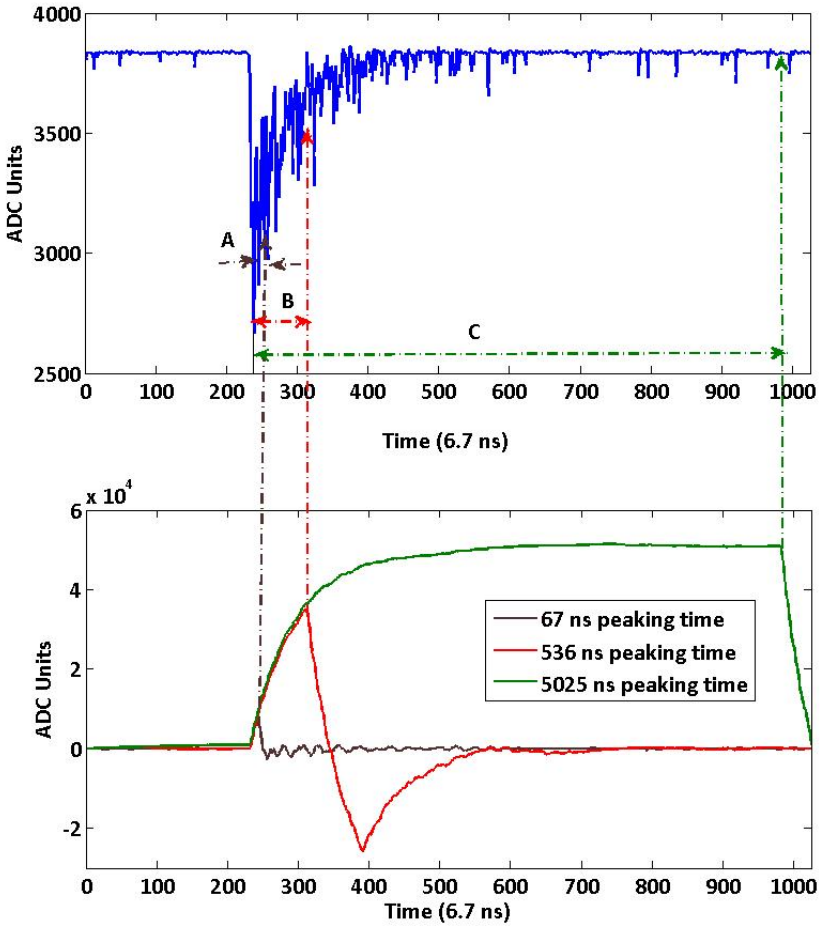

Fig. 3.8: Three regions of integration (Upper figure) and their corresponding filter responses (Lower figure.)

In the figure, A represents amplitude of the filter response for BC-400 scintillator pulse. B represents amplitude of the filter response for BGO scintillator pulse. C represents amplitude of the filter response for CsI(Tl) scintillator pulse.

Using these three sums, fast component ratio (FCR) and slow component ratio (SCR) are calculated from each anode pulses using the following equations:

Fast Component Ratio (FCR) = A/B [3.1]

Slow Component Ratio (SCR) = B-A/ (C-A) [3.2]

The FCR and SCR range from 0 to 1. A 2D scatter plot of FCR (Equation 3.1) versus SCR (Equation 3.2) shows different regions of concentration based on the scintillation layers at which energy deposition occurred (Fig. 3.8 and Fig. 3.9). The FWHM of the CsI(Tl) only region was used to get the optimum filter sizes used in the integrations.

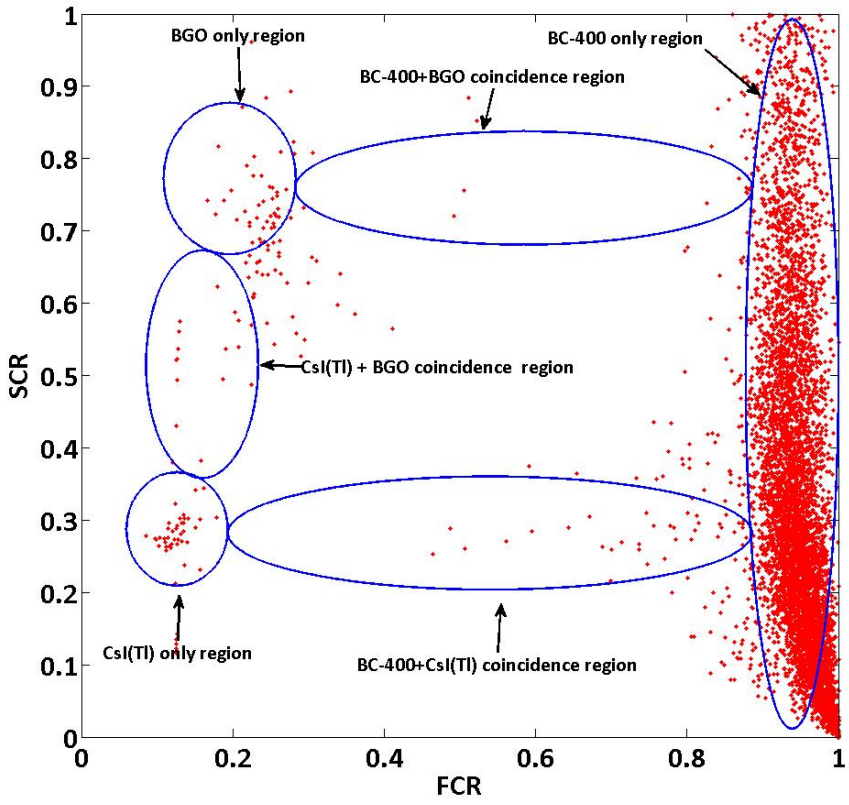

Fig. 3.9: Scatter of fast and slow component ratios from ^{36}Cl. The circled regions show single and coincidence events from BC-400, CsI(Tl) , and BGO

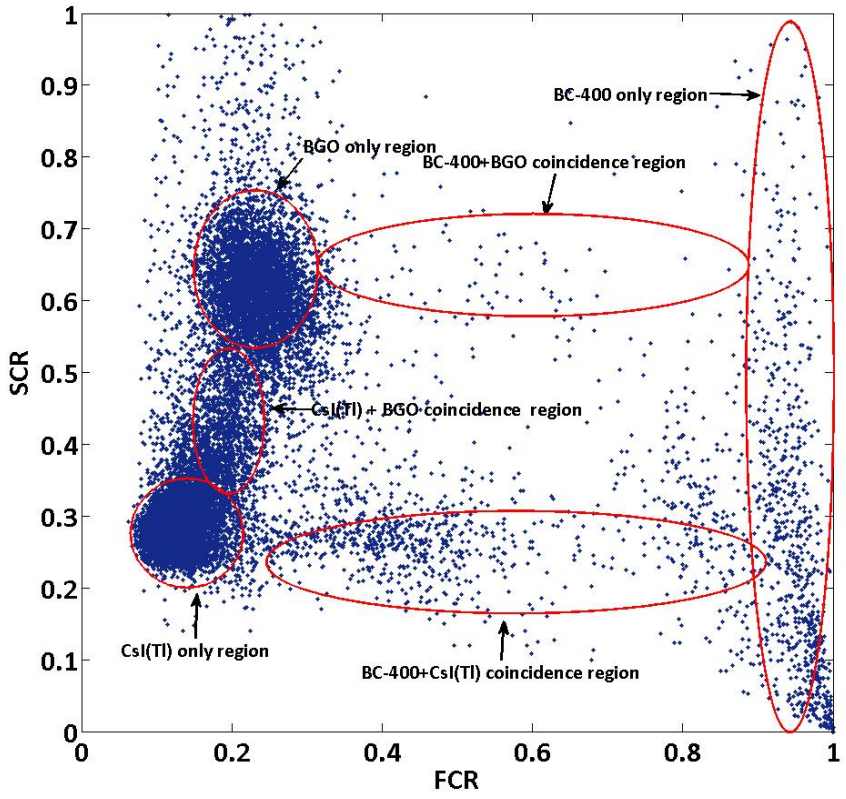

Fig. 3.10: Scatter of fast and slow component ratios from ^{137}Cs. The circled regions show single and coincidence events from BC-400, CsI(Tl) and BGO.

3.4.2.2 Least square pulse shape discrimination method

The second method implemented on MATLAB is to use a linear fit (Chapra, 2012) of the anode signals with experimentally determined functions. The anode signals can be written as

$$y_i = A.f_{A,i} + B.f_{B,i} + C.f_{c,i} + e_i \qquad [3.3]$$

where A, B and C are the unknown coefficients representing the amplitudes of anode pulses from the interaction with the three scintillators: BC-400, CsI(Tl) and BGO respectively. f_A is the response of the system to the BC-400 scintillator, f_B to the CsI(Tl) scintillator and f_C to the BGO scintillator. e_i is a residual between the response of the system and the actual anode signal.

The strategy to fit the data would be to minimize the sum of the squares of the residual for all the available data as shown in Equation [3.4]

$$S_r = \sum_{i=1}^{n} e_i^2 = \sum_{i=1}^{n} \left(y_i - \{Af_{A,i} + Bf_{B,i} + Cf_{c,i}\}\right)^2 \qquad [3.4]$$

To determine A, B and C, Equation [3.4] is differentiated with respect to each unknown coefficient

$$\frac{\partial S_r}{\partial A} = 2 \sum_{i=1}^{n} \left(y_i - \{Af_{A,i} + Bf_{B,i} + Cf_{C,i}\}\right) . f_{A,i} \qquad [3.5]$$

$$\frac{\partial S_r}{\partial B} = 2 \sum_{i=1}^{n} \left(y_i - \{Af_{A,i} + Bf_{B,i} + Cf_{C,i}\}\right) . f_{B,i} \qquad [3.6]$$

$$\frac{\partial S_r}{\partial C} = 2 \sum_{i=1}^{n} \left(y_i - \{Af_{A,i} + Bf_{B,i} + Cf_{C,i}\}\right) . f_{C,i} \qquad [3.7]$$

Setting the derivatives equal to zero will result in a minimum S_r

$$\sum_{i=1}^{n} \left(y_i f_{A,i}\right) = \sum_{i=1}^{n} \left(Af_{A,i}^2 + Bf_{B,i}f_{A,i} + Cf_{C,i}f_{A,i}\right) \qquad [3.8]$$

$$\sum_{i=1}^{n} \left(y_i f_{B,i}\right) = \sum_{i=1}^{n} \left(Af_{A,i}f_{B,i} + Bf_{B,i}^2 + Cf_{C,i}f_{B,i}\right) \qquad [3.9]$$

$$\sum_{i=1}^{n} \left(y_i f_{C,i}\right) = \sum_{i=1}^{n} \left(Af_{A,i}f_{C,i} + Bf_{B,i}f_{C,i} + Cf_{C,i}^2\right) \qquad [3.10]$$

Writing Equation(3.8-3.10) in a matrix form

$$\begin{pmatrix} \sum_{i=1}^{n}(y_i f_{A,i}) \\ \sum_{i=1}^{n}(y_i f_{B,i}) \\ \sum_{i=1}^{n}(y_i f_{C,i}) \end{pmatrix} = \begin{pmatrix} \sum_{i=1}^{n}(f_{A,i}^2) & \sum_{i=1}^{n}(f_{B,i} f_{A,i}) & \sum_{i=1}^{n}(f_{C,i} f_{A,i}) \\ \sum_{i=1}^{n}(f_{A,i} f_{B,i}) & \sum_{i=1}^{n}(f_{B,i}^2) & \sum_{i=1}^{n}(f_{C,i} f_{B,i}) \\ \sum_{i=1}^{n}(A f_{A,i} f_{C,i}) & \sum_{i=1}^{n}(B f_{B,i} f_{C,i}) & \sum_{i=1}^{n}(f_{C,i}^2) \end{pmatrix} . \begin{pmatrix} A \\ B \\ C \end{pmatrix}$$

[3.11]

The unknown coefficients from each scintillator can then be calculated as

$$\begin{pmatrix} A \\ B \\ C \end{pmatrix} = \begin{pmatrix} \sum_{i=1}^{n}(f_{A,i}^2) & \sum_{i=1}^{n}(f_{B,i} f_{A,i}) & \sum_{i=1}^{n}(f_{C,i} f_{A,i}) \\ \sum_{i=1}^{n}(f_{A,i} f_{B,i}) & \sum_{i=1}^{n}(f_{B,i}^2) & \sum_{i=1}^{n}(f_{C,i} f_{B,i}) \\ \sum_{i=1}^{n}(A f_{A,i} f_{C,i}) & \sum_{i=1}^{n}(B f_{B,i} f_{C,i}) & \sum_{i=1}^{n}(f_{C,i}^2) \end{pmatrix}^{-1} . \begin{pmatrix} \sum_{i=1}^{n}(y_i f_{A,i}) \\ \sum_{i=1}^{n}(y_i f_{B,i}) \\ \sum_{i=1}^{n}(y_i f_{C,i}) \end{pmatrix}$$

[3.12]

The model pulses f_A, f_B and f_c were determined experimentally. The three model pulses can be seen in Fig. 3.10.

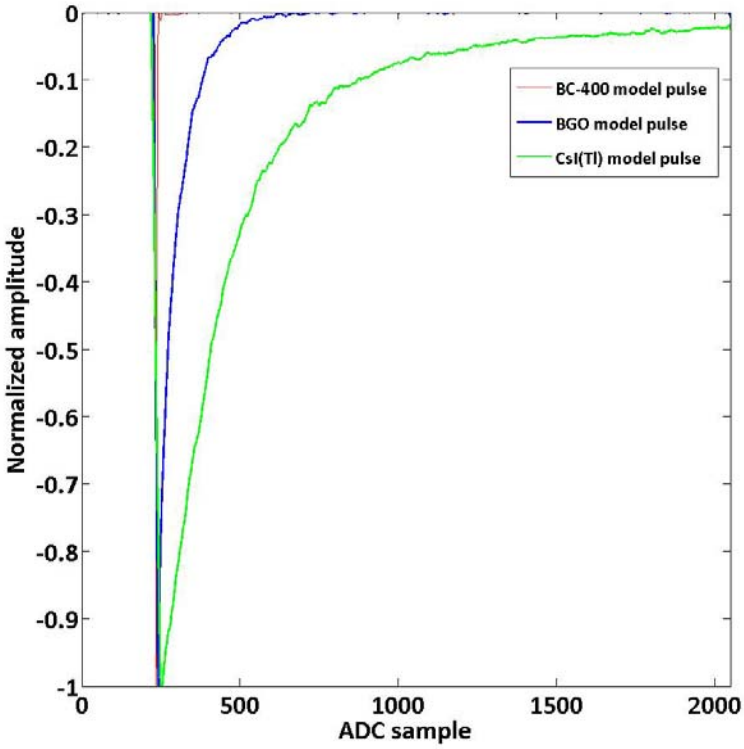

Fig. 3.11: Model pulses of BC-400, BGO and CsI(Tl).

A 2D scatter plot of the BC-400 (A) and CsI(Tl) (B) amplitude was used to test the pulse shape discrimination response for beta and gamma check sources. Fig. 3.11 shows 2D scatter plot when the phoswich detector is exposed to ^{36}Cl (beta source). Fig. 3.12 shows 2D scatter plot when the phoswich detector is exposed to ^{137}Cs (gamma source).

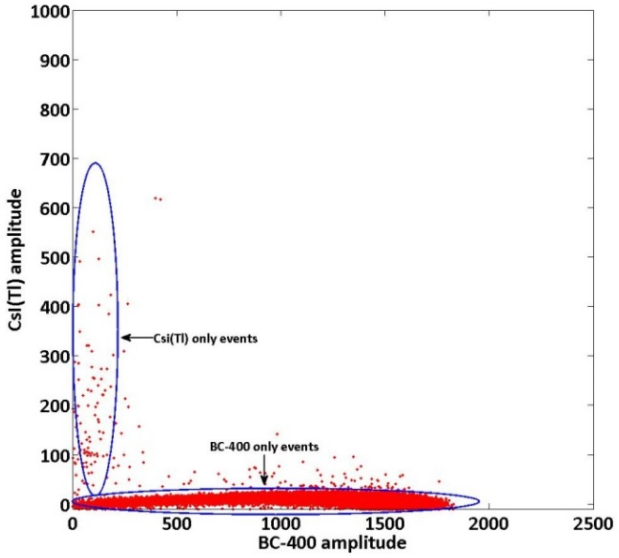

Fig. 3.12: A 2D scatter plot from ^{36}Cl using least square fitting method. The circled regions show single events from BC-400 and CsI(Tl) scintillators.

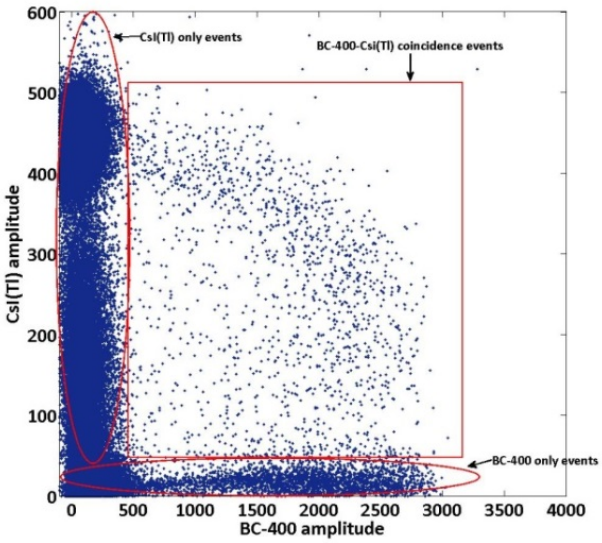

Fig. 3.13: A 2D scatter plot from ^{137}Cs using least square fitting method. The circled regions show single and coincidence events from BC-400 and CsI(Tl) scintillators.

For single events, majority of the events lie on the axis. Depending on which layer the interaction is occurring, the corresponding axis for that layer is populated. The other axis value will be closer to zero. For Beta source (^{36}Cl) the majority of the events were observed on the BC-400 amplitude axis. For gamma source (^{137}Cs) majority of the events were observed on the CsI(Tl) amplitude axis. For coincidence events, majority of the events are seen to lie on the plane instead of the axis. Using the different planes of interest, different coincidence events can be studied.

3.4.2.3 Energy Measurement

Similar energy measurement technique was used after pulses were discriminated in the FCR and SCR or least square pulse shape discrimination method. Using three digital triangular filters (f_1, f_2 and f_3) three values (F_{BC-400}, $F_{CsI(Tl)}$ and F_{BGO}) were used to integrate different areas of the pulse. f_1, f_2 and f_3 were chosen to integrate each pulse 67, 536 and 5025 ns after the trigger point respectively. Using appropriate calibration coefficients a and b, F_{BC-400}, $F_{CsI(Tl)}$ and F_{BGO} were used to calculate the energy released in BC-400, CsI(Tl) and BGO layers respectively. For coincidence events the energy deposition were calculated differently. For example, for a coincidence events between BC-400 and CsI(Tl) layer,

$E_{CsI(Tl)}$ (Energy deposited in the CsI(Tl) layer) = $a_{CsI(Tl)} + b_{CsI(Tl)} (F_{CsI(Tl)} - F_{BC-400})$ [3.13]

E_{BC-400}(Energy deposited in the BC-400 layer) = $a_{BC-400} + b_{BC-400} (F_{BC-400} - K (F_{CsI(Tl)}))$ [3.14]

$a_{CsI(Tl)}$ and $b_{CsI(Tl)}$ in Eq. 3.13 represents calibration coefficients for the CsI(Tl) layer. a_{BC-400} and b_{BC-400} in Eq. 3.14 represents calibration coefficients for the BC-

400 layer. K represents the contribution of CsI(Tl)'s scintillation component in the f_1 integration period.

Lab sources (^{109}Cd and ^{137}Cs) were used to measure the energy resolution (FWHM) of 22-keV, 88-keV and 662 keV x-rays and gamma rays. Fig. 3.13 and Fig. 3.14 show an example of energy spectrum obtained from the two pulse shape discrimination methods. The CsI(Tl) regions showed in Fig. 3.9 and Fig. 3.12 were used to plot the spectrum.

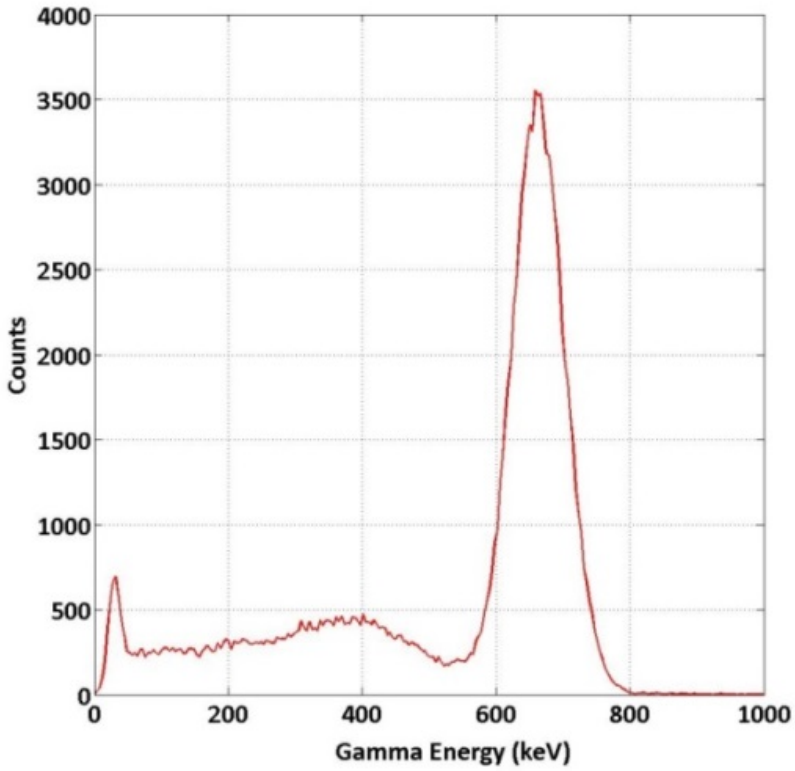

Fig. 3.14: The ^{137}Cs spectra which was collected from CsI(Tl) only events shown in Fig. 3.9.

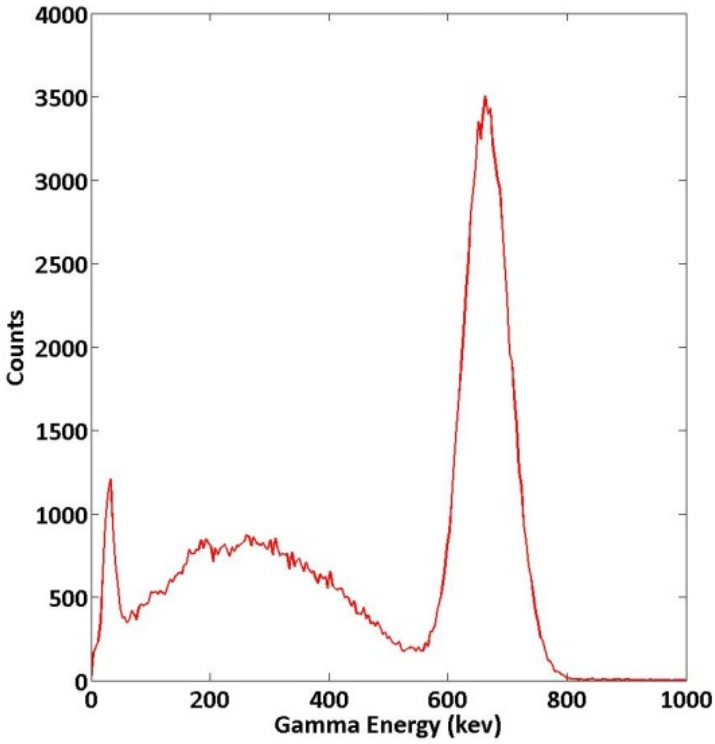

Fig. 3.15: The ^{137}Cs spectra which was collected from CsI(Tl) only events shown in Fig. 3.12.

The energy resolution measured can be seen in Table 3.5. The FCR-SCR method showed a better energy resolution when compared with the least square pulse shape discrimination method. In the least square pulse shape discrimination, events populated at the origin could not be discriminated as single CsI(Tl) or BC-400 events. So there are events lost at the origin. This might be one possible reason for the difference in energy resolution.

In the RX-1200 digital pulse processing firmware, the FCR-SCR method was implemented on the FPGA for real-time characterization of the phoswich detector.

Table 3. 5: Energy resolution measurement of ^{109}Cd and ^{137}Cs using the FCR-SCR and least square fitting pulse shape discrimination method.

Energy (keV)	Source	Resolution (%)	
		FCR-SCR method	Least square fitting method
22	^{109}Cd	60.0	70.0
30	^{137m}Ba	53.2	56.1
88	^{109}Cd	29.6	29.9
662	^{137}Cs	9.3	12.7

3.4.3 Real-time digital pulse processing firmware

A real-time digital pulse processing firmware was developed and implemented in a Field-programmable Gate Array (FPGA) device (A. T. Farsoni, Alemayehu, Alhawsawi, & Becker, 2013). A FPGA is a type of logic chip which is interconnected by a network of wires than can be programmed after manufacturing. FPGAs can be reprogrammed in-circuit in only a small fraction of a second.

In a FPGA-based radiation pulse processing system, all the pulse processing functions including energy measurement and histogram construction are realized in a single FPGA device. Since all the computation functions are executed in parallel in the hardware, a minimal dead time can be achieved using a single FPGA for real-time measurements. Since only one processing device is employed, developing codes for FPGA-based pulse processors are much easier and less time consuming (A. T. Farsoni et al., 2013).

The FPGA pulse processing algorithm was developed for operation in four modes. These modes are: Scope, Pulse-Shape analysis (PSA), Coincidence event (CE), and Multichannel Analyzer (MCA).

3.4.3.1 Scope mode

In the Scope mode, anode pulses are captured in a circular buffer and transferred to the PC. From this mode, the user can check the condition of anode pulses and make necessary modifications such as offset level, amplification gain and threshold. These changes can be made by a MATLAB program. Fig. 3.15 shows an example output of the scope mode.

3.4.3.2 Pulse-Shape analysis (PSA) mode

PSA mode is used to define four boundaries on the FCR-SCR scatter graph from single pulses. These boundaries are: Fast Ratio Lower Level (FRLL), Fast Ratio Upper Level (FRUL), Slow Ratio Lower Level (SRLL) and Slow Ratio Upper Level (SRUL). Pulse processing algorithm in the CE and MCA modes are based on the boundary regions set in the PSA mode. An example of the PSA mode output is seen in Fig. 3.16.

3.4.3.3 Coincidence event (CE) mode

In the CE mode, for individual coincidence pulse detected, pulse areas A_g and A_b (proportional to the number of scintillation photons in the CsI(Tl) and BC-400, respectively) are calculated in real-time and transferred to the PC. This will be used to construct a 3-D beta/gamma coincidence energy spectrum. An example of the CE mode output is seen in Fig. 3.17.

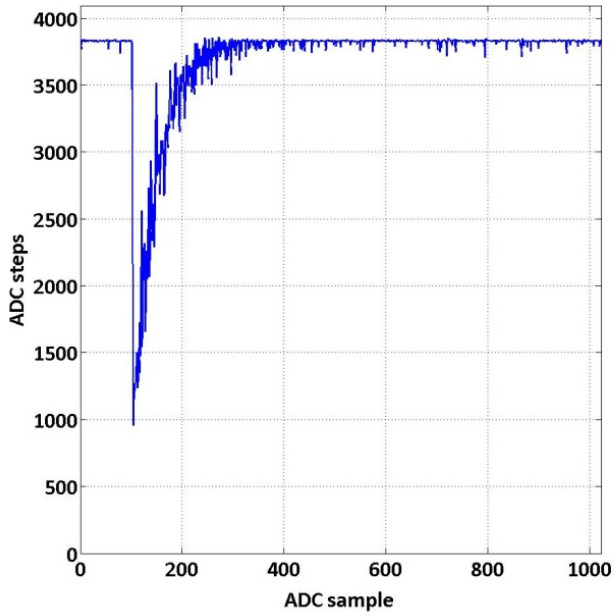

Fig. 3.16: An example of Scope mode output.

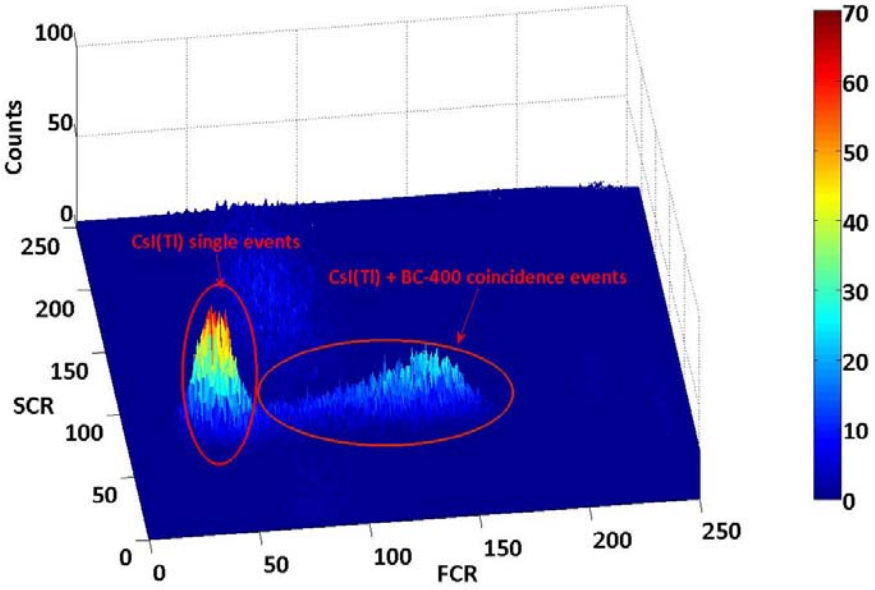

Fig. 3.17: An example of PSA mode output from ^{135}Xe

3.4.3.4 Multichannel Analyzer (MCA) mode

The MCA mode is used to collect separate gamma and beta-ray histograms in on-board FPGA device. Both histograms are updated only if the measured FCR and SCR values of the pulse are identified to be in a region of interest. An example of the MCA mode output is seen in Fig. 3.18.

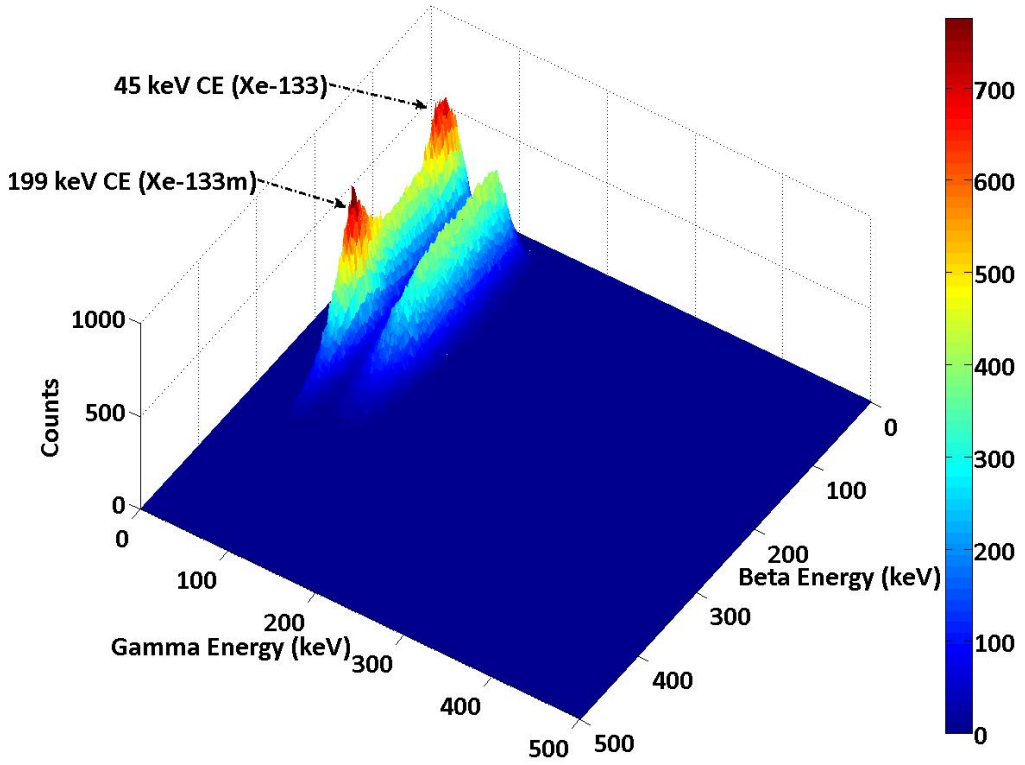

Fig. 3.18: An example of CE mode output from ^{133}Xe/^{133m}Xe

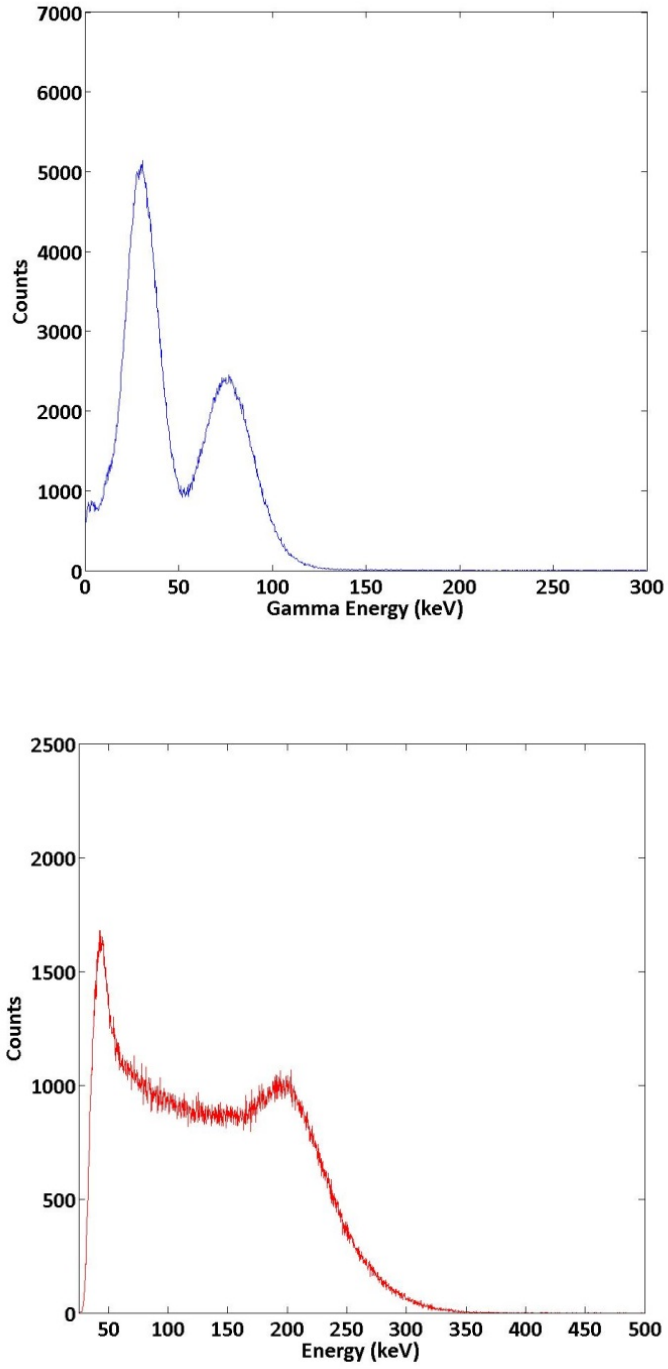

Fig. 3.19: An example of MCA mode output from $^{133}Xe/^{133m}Xe$.

3.4.4 FPGA design and implementation

Three modules: Trigger, Scope and Histogram are used to realize the four operational modes.

3.4.4.1 Scope module

The Scope mode is realized in the Scope module including two state machines and a circular buffer to capture and transfer sampled pulses to the PC. No digital processing is performed in this module.

3.4.4.2 Trigger module

The Trigger module was realized by using a digital triangular Finite Impulse Response filter. The module is used to generate a trigger input to other modules. Fig. 3.19 shows a block diagram of the Trigger module. In this module, the ADC samples are fed into the triangular filter then from there to a comparator. A state machine is used to issue a one-cycle trigger output when the filter output is above a predetermined threshold level.

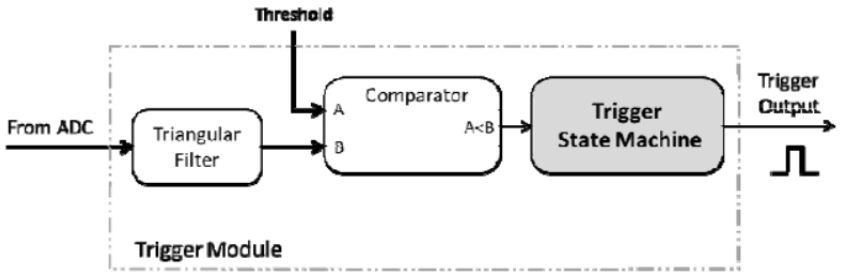

Fig. 3.20: Block diagram of the Trigger module. (Taken from (A. T. Farsoni et al., 2013)).

3.4.4.3 Histogram module

Except the scope mode, the other three FPGA operational modes were realized in the Histogam module illustrated in Fig. 3.20. The Histogram module receives 12 bits detector sample data from ADC and a trigger signal from the Trigger module.

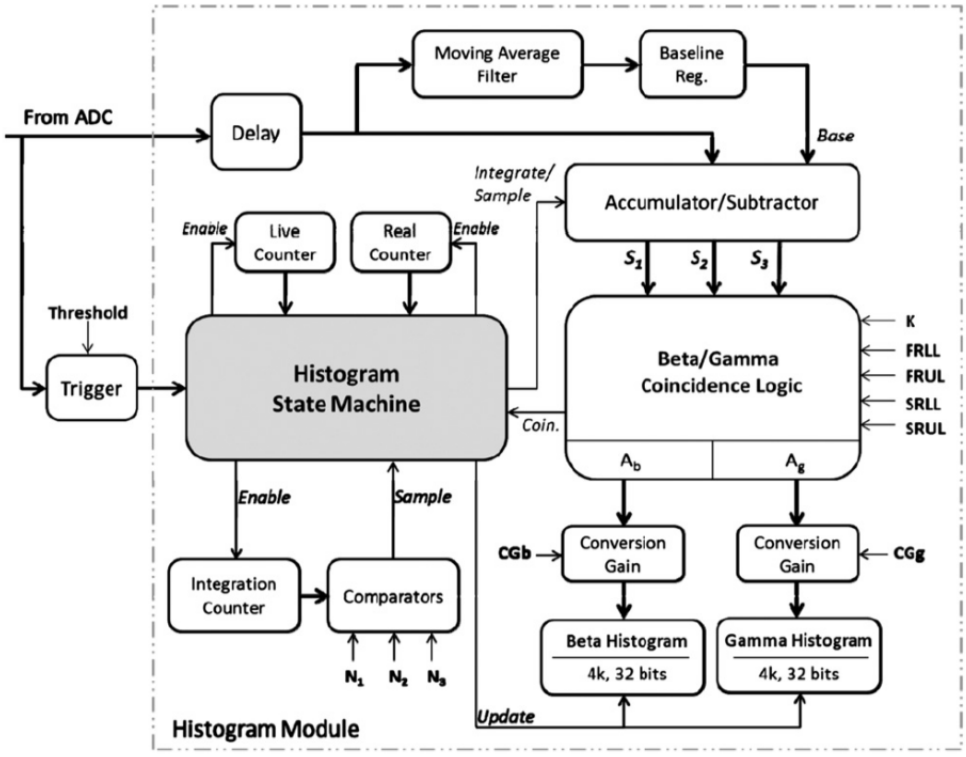

Fig. 3.21: A simplified block diagram of the Histogram module implemented in the FPGA device for real-time pulse shape discrimination and beta/gamma coincidence measurements. To simplify the diagram, only data processing path for the MCA mode is shown.(Taken from (A. T. Farsoni et al., 2013)).

A moving average filter is used to compute the average *Base* which is used to estimate the areas under each phoswich pulse. The *Base* is an average of the

baseline over eight ADC samples before a radiation pulse arrives. The average baseline is sampled using a register. The average baseline and delayed ADC samples are inputs to the Accumulator/Subtractor unit. The unit is used to estimate S_1, S_2 and S_3, defined mathematically by Eq. 3.15-3.19.

$$y[n] = y[n-1] + x[n] \quad [3.15]$$

$$b[n] = b[n-1] + Base \quad [3.16]$$

$$S_1 = b[N_1] - y[N_1] \quad [3.17]$$

$$S_2 = b[N_2] - y[N_2] \quad [3.18]$$

$$S_3 = b[N_3] - y[N_3] \quad [3.19]$$

where n is the sample index, $x[n]$ is the delayed ADC sample, $y[n]$ and $b[n]$ are the outputs from two accumulators, *Base* is the averaged baseline, and N_1 ,N_2 and N_3 are the number of ADC clock cycles within the three integration intervals Δt_1, Δt_2 and Δt_3, respectively.

The three calculated sums (S_1,S_2 and S_3) are fed into the Beta/Gamma Coincidence Logic (BGCL) unit (Fig. 3.21) . In the BGCL unit coincidence pulses are identified and their pulse areas A_g and A_b are calculated using the following equations:

$$A_g = S_3 - S_1 \quad [3.20]$$

$$A_b = S_1 - K(S_3 - S_1) \quad [3.21]$$

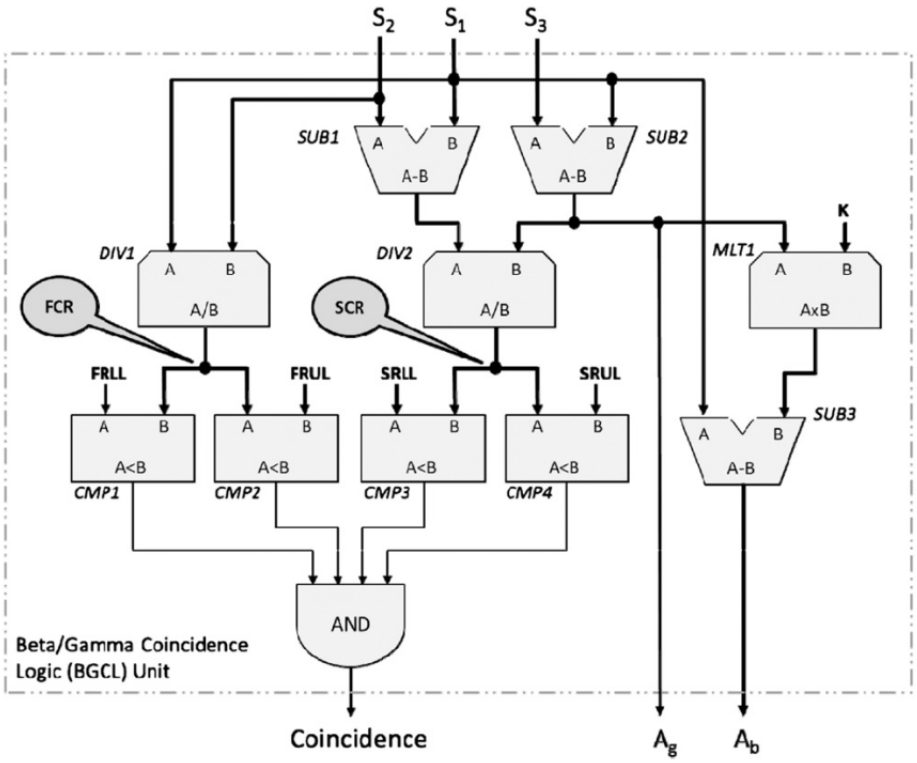

Fig. 3.22: Block diagram of the Beta/Gamma Coincidence Logic (BGCL) unit. (Taken from (A. T. Farsoni et al., 2013)).

Two separate histograms were implemented in the FPGA design to reconstruct the beta particle (conversion electrons) and gamma-ray (X-ray) energy spectra in real-time. The histograms were implemented using dual-port Block RAM memories available in SPARATAN-3 FPGA devices. Sixteen Block RAM's were used to implement these two 4k, 32-bit histograms. To measure elapsed real and live times to perform real-time quantitative measurements, two counters (*Live Counter* and *Real Counter*) were implemented in the Histogram module. The real-time pulse processing algorithm was synthesized and implemented using Xilinx's ISE webpack software (A. T. Farsoni et al., 2013).

4. Results and discussion

4.1 WASPD background count rate

For background count rate measurement, the phoswich detector was placed in a lead shield with a thickness of 5.0 cm. The total count rate from all events was measured to be 1.26 counts per second. For coincidence events (Fig. 3.16), the count rate was 0.023 counts per second. The measured background count rate was compared with other Radioxenon detection systems. The result can be seen in Table 4.1. When compared with other radioxenon detectors, WASPD showed a significant reduction in background count rate in all and coincidence events. The observed reduction in background count rate is the result of integrating BGO scintillator with BC-400 and CsI(Tl) scintillators and pulse shape discrimination to identify scattered photons and ultimately reduce the background count rate.

Table 4.1: Background count rated for the phoswich and other radioxenon detectors.

Detector	**Background Count Rate (Counts per second)**	
	All events	Coincidence events
WASPD (This work)	1.26	0.02
ASPD(Abi T. Farsoni et al., 2013)	3.29	0.06
SAUNA(Wolfgang Hennig et al., 2009)	7.5-12	0.03
ARSA(Wolfgang Hennig et al., 2009)	30	0.1
BGW(Wolfgang Hennig et al., 2009)	5.5	0.025
PhosWatch(Wolfgang Hennig et al., 2009)	3-8	0.02-0.08

4.2 WASPD Compton suppression capability, energy resolution and efficiency

To study the phoswich detector Compton suppression capability, measurement was first done by assembling the CsI(Tl) scintillator only (unsuppressed) and later assembling the BGO together with CsI(Tl)(suppressed). Fig. 4.1 shows unsuppressed and suppressed background gamma-ray spectra. The measurements were taken for 24 hours without using any shielding.

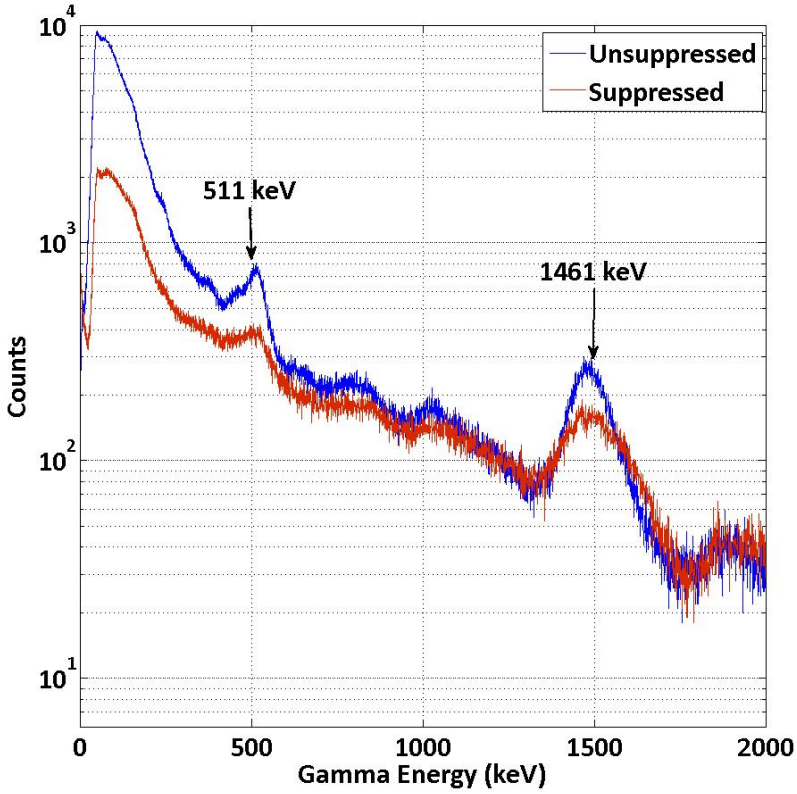

Fig. 4.1: Background spectra for suppressed (red) and unsuppressed (blue) settings. The spectra were collected for 24 h. No shielding was used in these measurements

The background suppression factor was studied by using the equation:

$$\text{Suppression Factor (E)} = \frac{C_u(E) - C_s(E)}{C_u(E)} \times 100 \qquad [4.1]$$

Where $C_u(E)$ is the number of counts in energy E of the unsuppressed spectrum and $C_s(E)$ is the number of counts in energy E of the suppressed spectrum. The total background count was reduced by (49±9) % in the suppressed case for 10-400 keV energy range. Fig. 4.2 shows the background suppression factor plot.

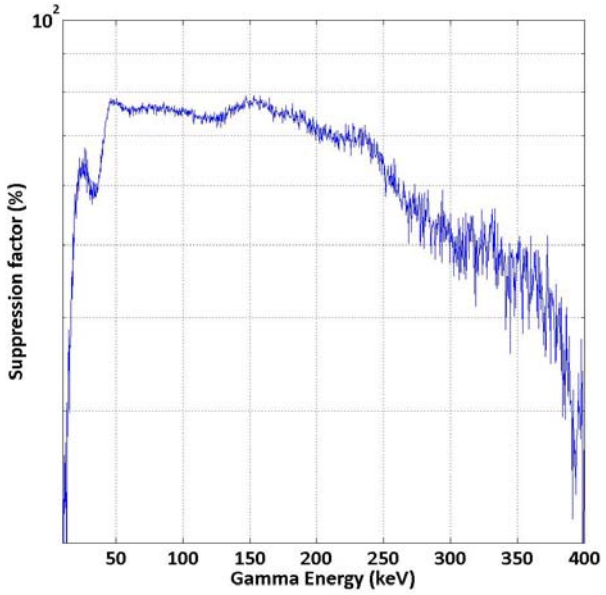

Fig. 4.2: Background suppression factor plot

The detector Compton suppression capability, energy resolution and photopeak intrinsic efficiencies for different gamma energies were studied using ^{109}Cd, ^{137}Cs and ^{60}Co tube sources (Fig. 4.3). The tube sources were purchased from Spectrum Techniques.

Fig. 4.3: Tube sources used in the study.

The radionuclides used, their half-life, photon energy, intensity, calibration date, activity at the time of purchase can be seen in Table 4.2.

Table 4.2: Gamma sources used, date of purchase, activity at the time of measurement and yield.

Source	Half-life (years)	Photon Energy (keV)	Intensity (%)	Calibration date	Activity (µ Ci)
^{109}Cd	1.27	22	85.2	May 13, 2013	0.113
	1.27	88	3.61	May 13, 2013	0.113
^{137}Cs	30.07	661.66	85.1	May 13, 2013	0.106
^{60}Co	5.2714	1173.24	99.97	May 13, 2013	0.134
	5.2714	1332.5	99.99	May 13, 2013	0.134

All measurements were done by placing the tube sources inside the CsI(Tl) well. To get optimal light collection efficiency, the tube sources were wrapped with several layers of Teflon tape (BC-642 PTFE Reflector Tape, Saint-Gobain crystals). The wrapping showed an enhancement in the light collection efficiency. Fig. 4.4 shows a ^{137}Cs spectrum taken for 1 hr. and same photopeak count with and

without wrapping of the tube source with Teflon. The photopeak light collection efficiency was improved by 5.5 % after the wrap. For the rest of the measurements, the tube sources were wrapped with Teflon before placing it in the well.

Fig. 4.5 shows the unsuppressed and suppressed plots for ^{137}Cs. Here the detector was placed inside a thick lead shield and a tube source was placed at the center of the detector well. The figure shows 30 keV X-ray peak from ^{137m}Ba and 662 keV photopeak. It can be seen that in the events close to Compton edge, suppressed events are more populated than the unsuppressed events. This is believed to be due to considering the same maximum photopeak count in both cases.

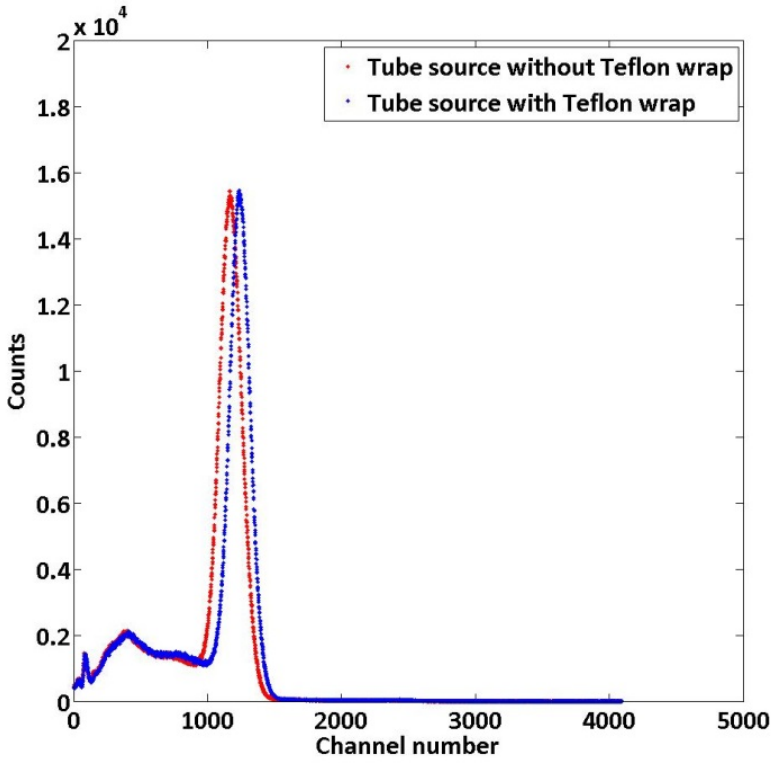

Fig. 4.4: Light collection comparison when the ^{137}Cs is placed in the well with (blue) and without (red) Teflon wrap.

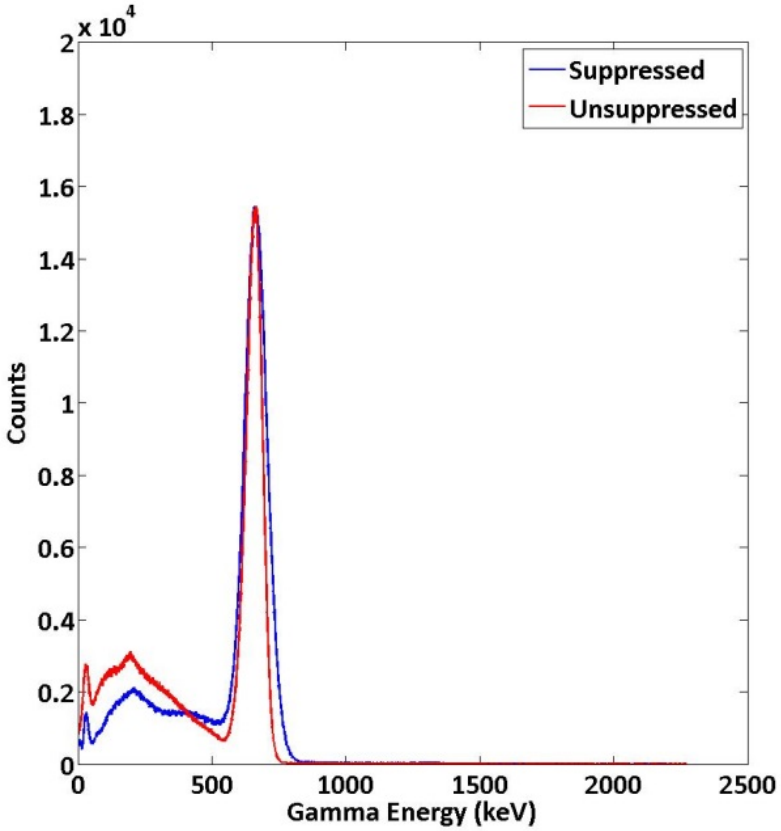

Fig. 4.5: Unsuppressed and suppressed gamma-ray spectra from Cs-137.

Fig. 4.6 shows a suppression factor as a function of gamma-ray energy for Cs-137. The suppression factor was observed to range from 67-30% in the energy range 10-350 keV. The suppression factor was observed to decrease for higher energies (> 350 keV.) This was because the CsI(Tl) was not surrounded by BGO at the front. The BGO is more effective for forward scattering photons. High energy photons have the tendency to scatter with large angles (Knoll, 2010). Some of these high energy photons will thus leave the detector without depositing energy. This as a result will reduce the suppression factor.

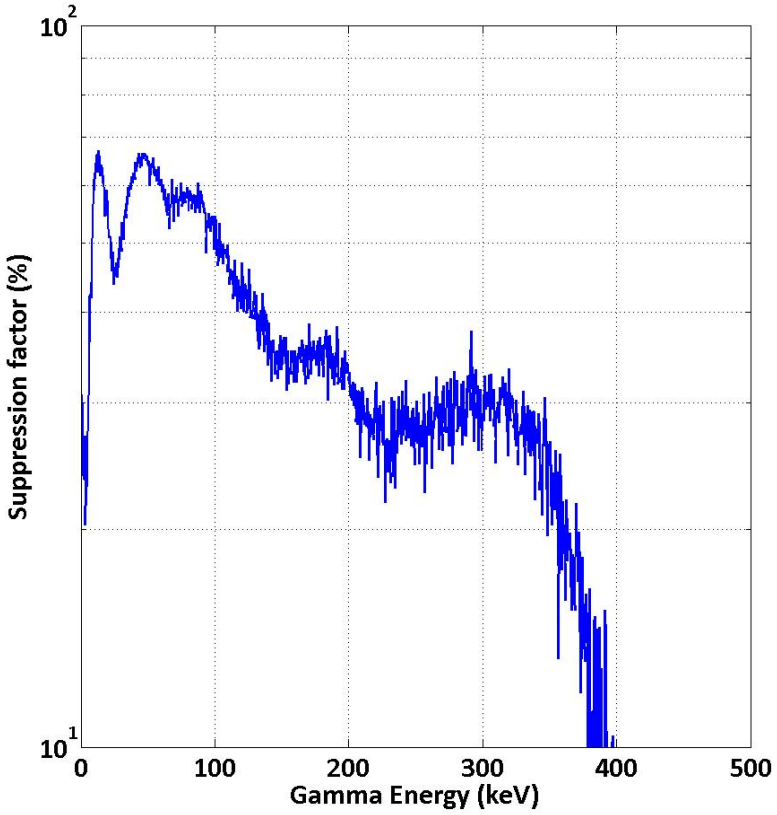

Fig. 4.6: Suppression factor as a function of gamma-ray energy when the detector is exposed to ^{137}Cs.

Energy resolution for different gamma energies can be seen in Fig. 4.7 and Table 4.3 for unsuppressed and suppressed configuration. Energy resolution for 662 keV ^{137}Cs photopeak from suppressed and unsuppressed configuration was measured to be 13.6 and 9.4 % respectively. The resolution of 662 keV of ^{137}Cs is 12% and 7.3% for ARSA (Paul L. Reeder et al., 2004) and SAUNA (Ringbom et al., 2003) radioxenon detectors.

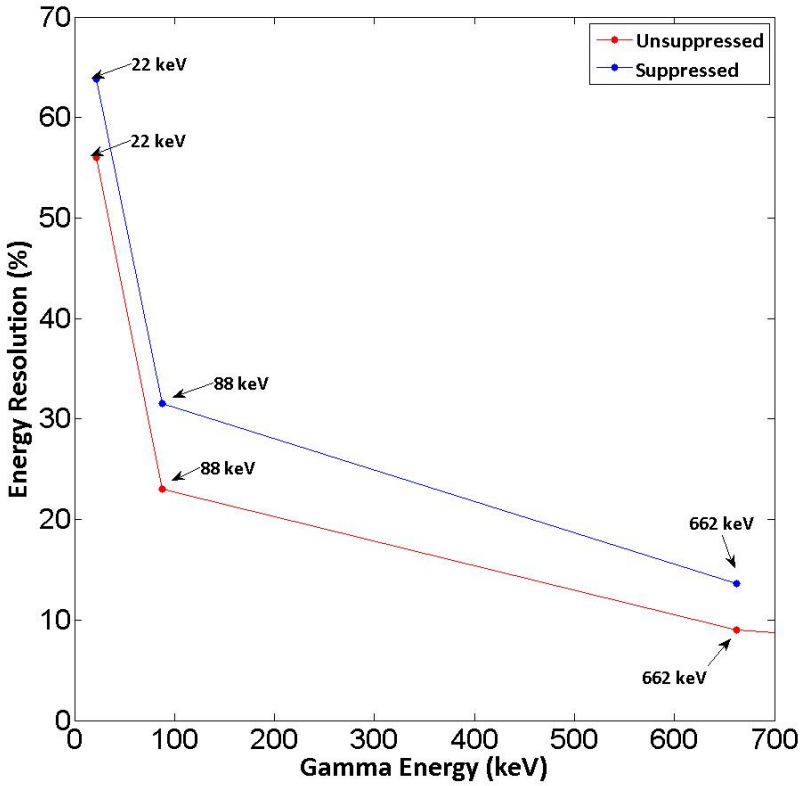

Fig. 4.7: Unsuppressed and suppressed energy resolution versus gamma energy.

Table 4.3: Energy resolution measured for Unsuppressed and Suppressed configuration.

		Energy resolution (%)	
Photon Energy (keV)	**Source**	**Unsuppressed**	**Suppressed**
22	^{109}Cd	56.1	63.8
88	^{109}Cd	23.4	31.5
662	^{137}Cs	9.4	13.6

Fig. 4.8 and Table 4.4 show photopeak intrinsic efficiencies for three photon energies in unsuppressed and suppressed configurations. From the results it can be seen that the pulse shape discrimination used doesn't reject photoelectric events significantly. The difference between the unsuppressed and suppressed photopeak efficiency was observed to range only between 2-13 %.

Table 4.4: Photopeak efficiencies measured for Unsuppressed and Suppressed configuration.

		Photopeak effieciency (%)	
Photon Energy (keV)	**Source**	**Unsuppressed**	**Suppressed**
88	^{109}Cd	57.59±0.11	44.60±0.11
662	^{137}Cs	24.17±0.01	21.67±0.01
1332	^{60}Co	7.62±0.01	5.54±0.01

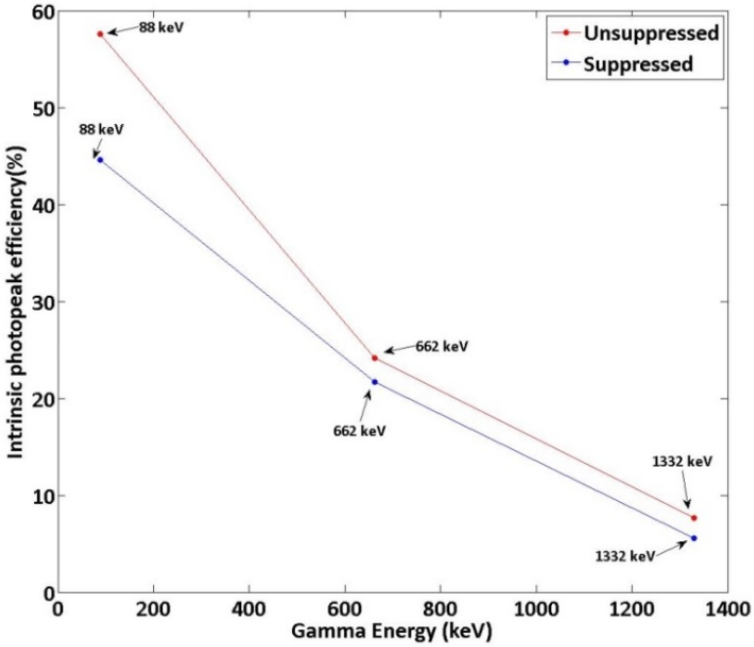

Fig. 4.8: Unsuppressed and suppressed Photopeak efficiency versus gamma energy.

4.3 Real-time Radioxenon measurements using WASPD

To test the detector for measuring xenon radioisotopes ^{131m}Xe, ^{133m}Xe, ^{133}Xe and ^{135}Xe, stable and highly enriched (>99%) isotopes of ^{130}Xe , ^{132}Xe and ^{134}Xe were irradiated in the thermal column of the Oregon State University TRIGA reactor. Table 4.5 shows the activation time for each gas and the resulting activities before cooling.

Table 4.5: Stable xenon activation time and resulting activities.

Stable Xenon isotope	Activation time (hrs.)	Neutron flux ($n.cm^{-2}.s^{-1}$)	Resulting activities (μci)
^{130}Xe	12	7×10^{10}	1.79 (^{131m}Xe)
^{132}Xe	12	7×10^{10}	1.13 (^{133}Xe)
^{132}Xe	12	7×10^{10}	3.84 (^{133m}Xe)
^{134}Xe	6	7×10^{10}	14.5 (^{135}Xe)

4.3.1 ^{135}Xe measurements

^{135}Xe emits 250 keV gamma-rays in coincidence with beta particles (E_{max}= 905 keV). Fig. 4.9 shows the resulting gamma-ray spectrum obtained in CsI(Tl)+BC-400 coincidence events region. The spectrum features the characteristic ^{135}Xe peak at 250 keV for gamma-ray and distributed beta energy. The 250 keV photopeak in Fig. 4.9 has a resolution (FWHM) of about 19.3%.

Resulting 3-D beta-gamma surface plot from ^{135}Xe can be seen in Fig. 4.10. The plot features a populated area at gamma energy (250 keV) and beta energy extending from zero to the maximum energy of beta particles (905 keV)

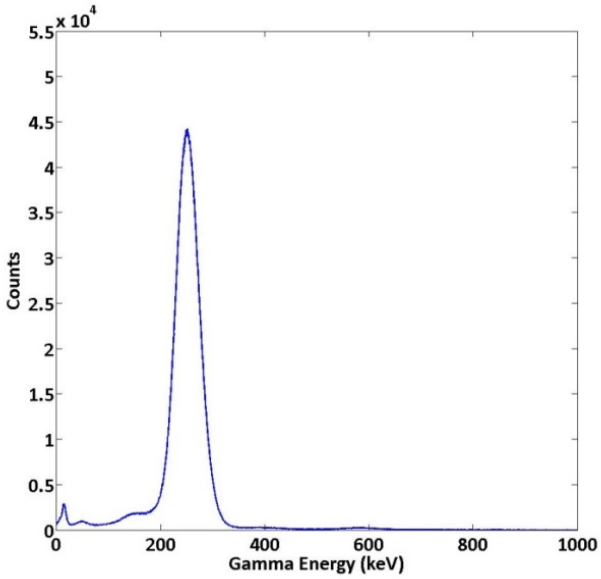

Fig. 4.9: Gamma energy spectrum from ^{135}Xe. The spectrum was collected from beta-gamma coincidence events.

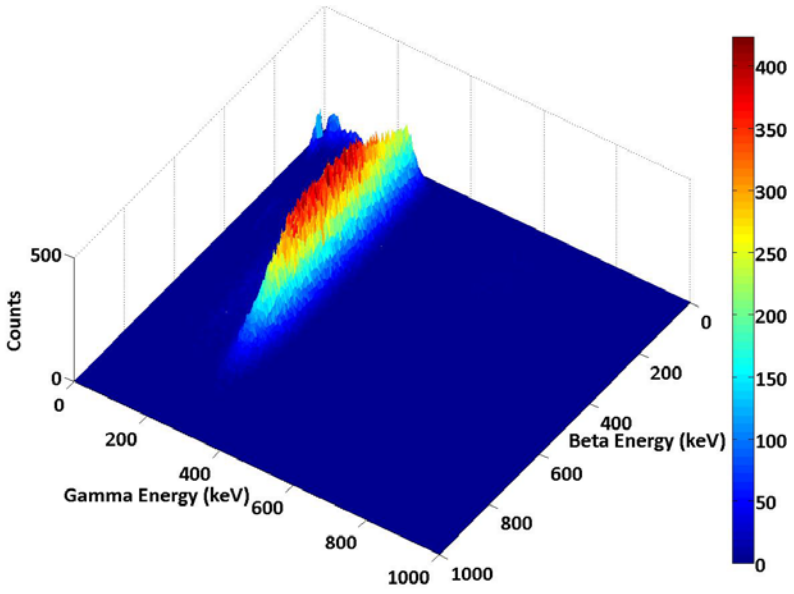

Fig. 4.10: 3-D beta-gamma surface plot from ^{135}Xe.

4.3.2 ^{133}Xe/^{133m}Xe measurements

^{133}Xe/ ^{133m}Xe emits 31 keV X-rays in coincidence with beta particles (E_{max} = 346 keV) and conversion electrons (45 keV and 199 keV) and 81 keV gamma-rays in coincidence with beta particles (E_{max} = 346 keV). Fig. 4.11 shows the resulting characteristic ^{133}Xe/ ^{133m}Xe peaks at 31 and 81 keV for gamma-ray and Fig. 4.12 shows distributed beta energy. The 31 and 81 keV photopeaks in Fig. 4.11 have a resolution (FWHM) of about 47.7% and 27.6% respectively. Fig. 4.12 shows two peaks at 45 keV and 199 keV. These peaks represent conversion electrons emitted from ^{133}Xe and ^{133m}Xe respectively.

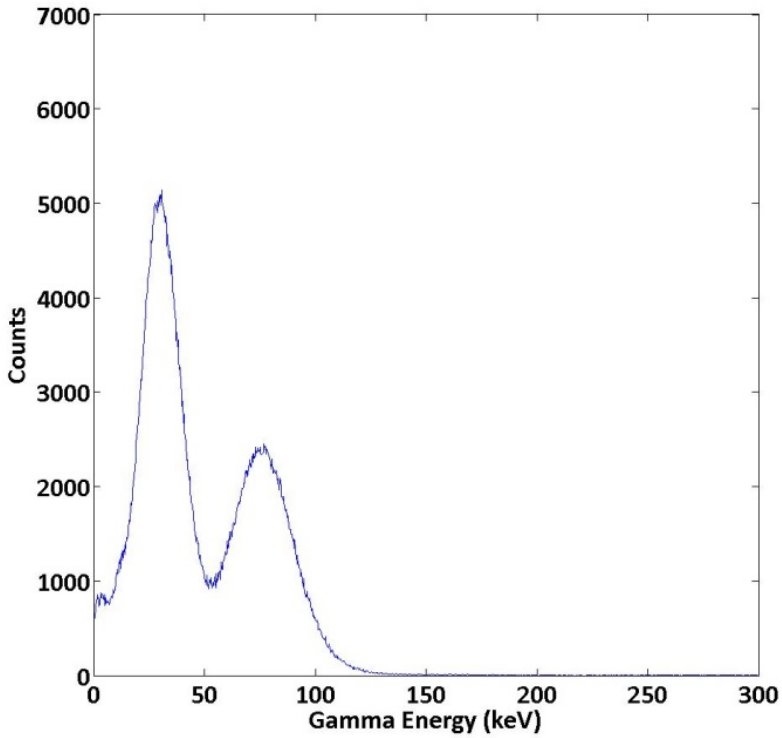

Fig. 4.11: Gamma energy spectrum from ^{133}Xe/^{133m}Xe. The spectrum was collected from beta-gamma coincidence events.

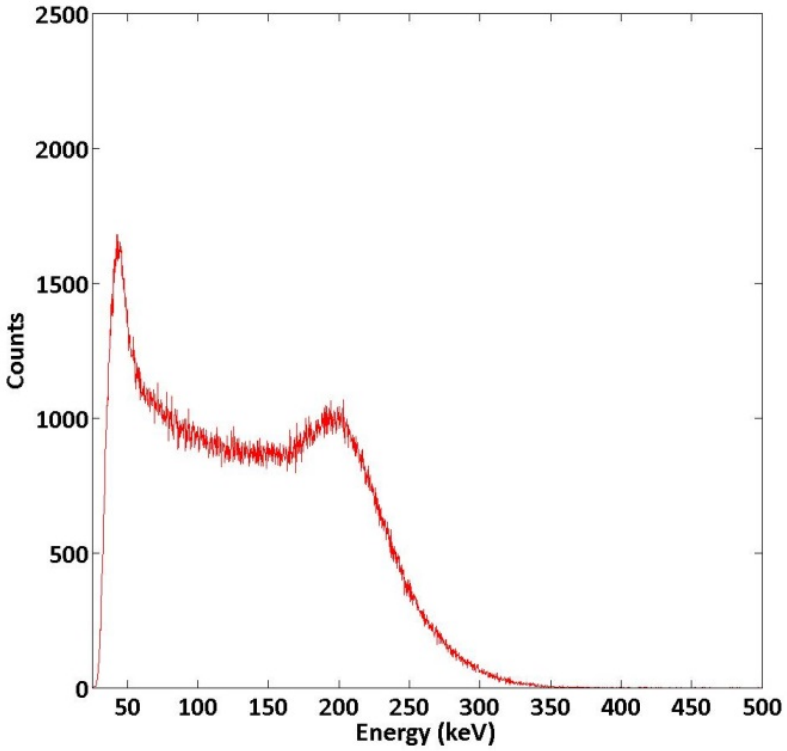

Fig. 4.12: Beta energy spectrum from ^{133}Xe/^{133m}Xe. The spectrum was collected from beta-gamma coincidence events

Resulting 3-D beta-gamma surface plot from ^{133}Xe/ ^{133m}Xe can be seen in Fig. 4.13. The plot features a populated area at gamma energy (30 keV and 81 keV) and beta energy extending from zero to the maximum energy of beta particles (346 KeV). In the 30 keV line, due to simultaneous absorption of conversion electrons (45 keV) and betas, the beta energy distribution was observed to be shifted to higher energies. The 45 and 199 keV conversion electron peaks can also be seen in the 31 keV line.

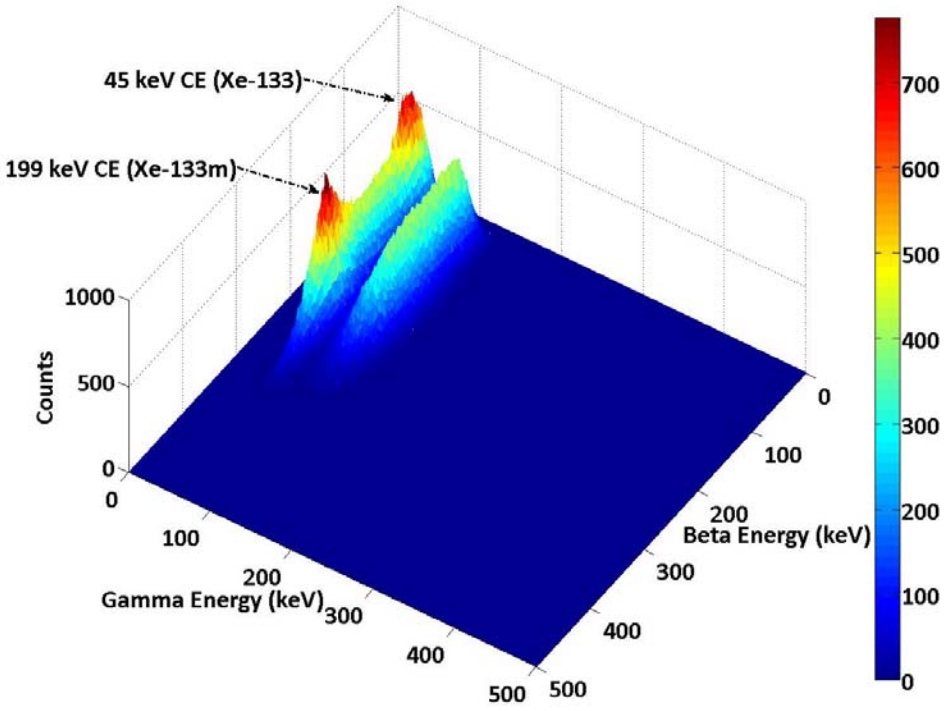

Fig. 4.13: 3-D beta-gamma surface plot from ^{133}Xe/^{133m}Xe.

4.3.3 ^{131m}Xe measurements

^{131m}Xe emits 30 keV x-rays in coincidence with 129 keV CEs. Fig. 4.14 and Fig. 4.15 show the X-ray and CE spectra. The spectra feature the characteristic ^{131m}Xe peak at 30 keV for x-ray and a peak at 129 keV for CE. The 30 keV photopeak in Fig. 4.15 has a resolution (FWHM) of about 51.7%. The 129 keV CE peak in Fig. 4.15 has a resolution (FWHM) of about 38.5%. Resulting 3-D beta-gamma surface plot from ^{131m}Xe can be seen in Fig. 4.16. Because ^{131m}Xe has only CEs, a fixed peak was observed at the beta energy axis instead of a distribution.

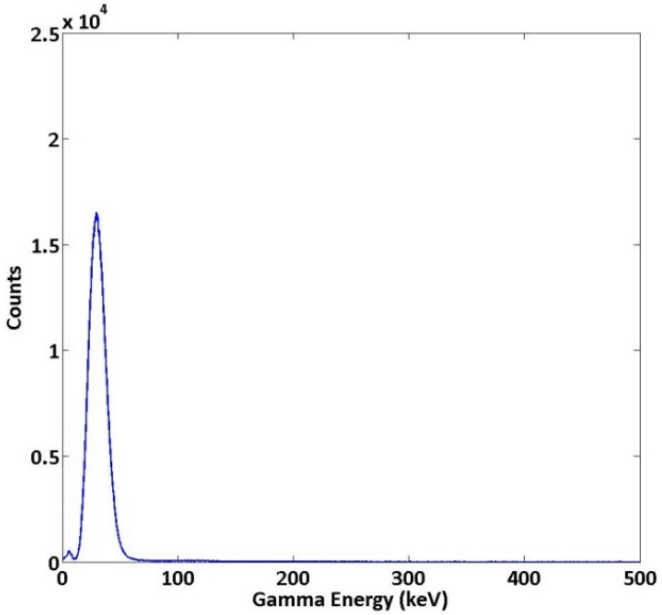

Fig. 4.14: Gamma energy spectrum from ^{131m}Xe. The spectrum was collected from beta-gamma coincidence events.

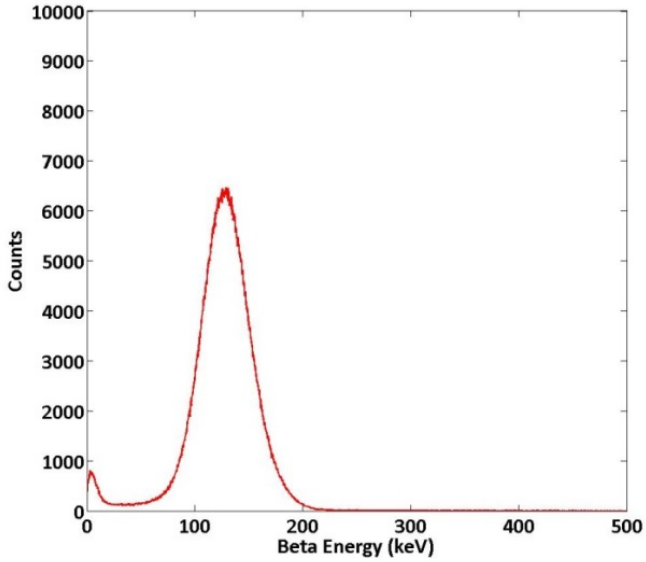

Fig. 4.15: Beta energy spectrum from ^{131m}Xe. The spectrum was collected from beta-gamma coincidence events.

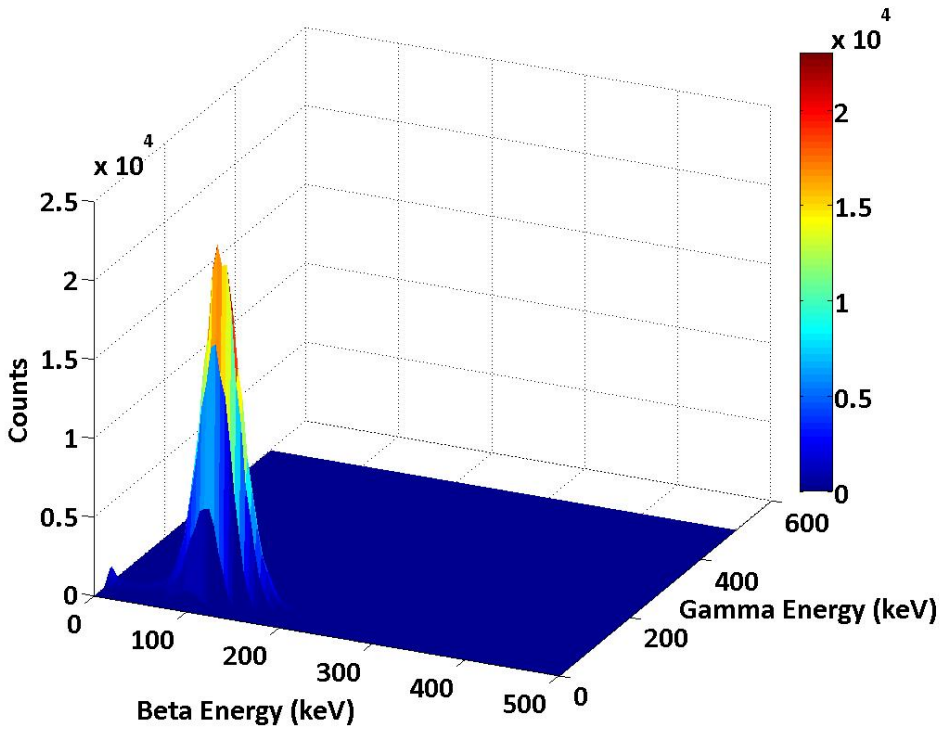

Fig. 4.16: 3-D beta-gamma surface plot from ^{131m}Xe

4.4 Minimum Detectable Concentration (MDC)

Radioxenon detection systems to be installed at the radioxenon monitoring stations should have a high sensitivity due to environmental factors which reduce their concentration when they reach radioxenon detection systems. This sensitivity is measured in terms of detector's Minimum Detectable Concentration (MDC). IMS requires that radioxenon monitoring systems should have a MDC of less than or equal to 1 mBq/m^3 for ^{133}Xe (Wernsperger & Schlosser, 2004).

According to the MDC definition stated in (Currie, 1968)(McIntyre et al., 2006), the MDC can be calculated by:

$$MDC\left(\frac{mBq}{m^3 air}\right) = \frac{2.71+4.65\sigma_0}{\varepsilon_\gamma \varepsilon_\beta \gamma_{BR} \beta_{BR}} \frac{\lambda^2}{(1-\exp(-\lambda T_c))\exp(-\lambda T_P)(1-\exp(-\lambda T_A)} \cdot \frac{T_c * 1000}{V_{air}} \quad [4.2]$$

where

$\sigma_0 = \sqrt{Background\ Counts}$

$\varepsilon_\gamma =$ γ efficiency

$\varepsilon_\beta =$ β efficiency

$\gamma_{BR} =$ γ branching ratio

$\beta_{BR} =$ β branching ratio

$\lambda = \ln(2)/t_{1/2}$

$T_c =$ Xenon Collection Time

$T_P =$ Processing Time of Gas

$T_A =$ Acquisiton Time of Counts

$V_{air} =$ cc of Xenon / 0.087 cc of Xenon per m^3 air

In our phoswich detection system, radioxenon gas was directly injected into the gas cell. So xenon collection time, processing time of the gas and decays during collection and processing of the gas can be ignored(Wolfgang Hennig et al., 2011). Simplifying eq. 4.2 after these considerations

$$MDC\left(\frac{mBq}{m^3 air}\right) = \frac{2.71+4.65\sigma_0}{\varepsilon_\gamma \varepsilon_\beta \gamma_{BR} \beta_{BR} T_A V_{air}} \quad [4.3]$$

Where

$\sigma_0 = \sqrt{Background\ Counts}$

$\varepsilon_\gamma =$ γ efficiency

$\varepsilon_\beta =$ β efficiency

$\gamma_{BR} =$ γ branching ratio

$\beta_{BR} =$ β branching ratio

T_{acq} = measurement time (24 h)

V_{air} = cc of Xenon / 0.087 cc of Xenon per m^3 air

A 24h background measurement was taken and 2xFWHM of counts under each region of interest (ROI) shown in Table 4.6 was used to calculate σ_0. For ^{135}Xe background measurement, the 2D region in Fig 4.10 was used to calculate the percentage of counts falling in the 250 keV region and the result was used to correct the 250 keV background counts. For ^{133}Xe background measurement, the 2D region in Fig 4.13 was used to calculate the percentage of counts falling in the 31 and 81 keV regions and the result was used to correct the 31 and 81 keV background counts. For ^{133m}Xe background measurement, the 2D region in Fig 4.13 was used to calculate the percentage of counts falling in the 199 keV region and the result was used to correct the 31 keV background counts. For ^{131m}Xe background measurement, the 2D region in Fig 4.16 was used to calculate the percentage of counts falling in the 129 keV region and the result was used to correct the 31 keV background counts.

Beta (β_{BR}) and gamma (γ_{BR}) branching ratio values were taken from literature (Auer et al., 2010). For V_{air} and T_A, a 20 m^3 air volume and 24 hrs acquisition time was used respectively.

Table 4. 6: Branching ratios for the ROIs.

Radioxenon	**Region of interest(ROI)**	**Branching ratio (%)** $\gamma_{BR} * \beta_{BR}$
^{131m}Xe	Sum of 29.46 to 34.61 keV X-rays and 129 keV CEs	56.1
^{133}Xe	31.63 keV X-ray + 45 keV CEs + 346 keV beta	48.9
	80.98 keV gamma + 346 beta	37.2
^{133m}Xe	Sum of 29.46 keV-34.61 keV X-rays and 199 keV CEs	58.4
^{135}Xe	249.8 keV gamma + 910 keV beta	90

The coincidence detection efficiency was computed experimentally using the following equation for each ROI.

$$\varepsilon_{ROI} = \left(\frac{\sum_{photopeak} - \sum_{background}}{t * A * f} \right) \qquad [4.4]$$

Where

$\sum_{photopeak} - \sum_{background}$ = net count under coincidence photopeak of the ROI

t = Live time

A = Activity of the source

f = decay fraction

The experimental coincidence detection efficiencies are given in Table 4.7. Uncertainties in the neutron flux and amount of gas lost while transferring the activated gas to the detector gas cell have a major contribution to the associated errors given in Table 4.7.

Table 4. 7: Coincidence detection efficiency.

Isotope	Coincident decays	Coincidence detection efficiency (simulation)	Coincidence detection efficiency (experimental)
^{131m}Xe	31 keV X-rays and 129 keV CE	(73.0±3.0)%	(49.19±4.1)%
^{133}Xe	31 keV X-ray + 346 keV beta	(77.1±3.8)%	(41.1±6.4)%
	81 keV gamma + 346 beta	(75.4±3.7)%	(37.0±6.1)%
^{133m}Xe	31 keV X-ray and 199 keV CE	(78.5±6.4)%	(44.22±3.32)%
^{135}Xe	250 keV gamma + 910 keV beta	(65.9±7.4)%	(39.45±3.85)%

The MDC was then calculated for each radioxenon isotopes using [4.3] and [4.4]. As can be seen from table 4.7, even though Xe-133 has two signatures, a single MDC was calculated by combining both MDCs using the equation(McIntyre et al., 2006):

$$^{133}\mathrm{Xe}_{\mathrm{MDC}}\left(\frac{mBq}{m^3\ air}\right) = \sqrt{\frac{1}{\left(^{133}Xe_{MDC}^{81keV}\right)^{-2}+\left(^{133}Xe_{MDC}^{30keV}\right)^{-2}}} \qquad [4.5]$$

It can be seen from Table 4.8, the MDC calculated for all xenon radioisotopes are close to or below the minimum IMS requirement of 1 mBq/m^3.

Table 4. 8: Simulation and experimental MDC result.

Isotope	**Minimum Detectable Concentration (MDC) (mBq/m^3)**	
	Simulation	**Experimental**
^{131m}Xe	(0.75±0.08)%	(1.1±0.27)%
^{133}Xe	(0.28±0.04)%	(0.57±0.11)%
^{133m}Xe	(0.28±0.05)%	(0.50±0.23)%
^{135}Xe	(0.1±0.02)%	(0.16±0.08)%

Fig.4.17 compare the MDCs reported from ARSA (Foltz Biegalski & Biegalski, 2001), SAUNA (Wolfgang Hennig et al., 2011), SPALAX (Le Petit et al., 2008) , PW5 (Wolfgang Hennig et al., 2009) and the MDCs we obtained in this work.

Our detection system has comparable MDCs with all detection systems except PW5. It was observed from Fig. 4.17 that PW5 has a relatively large MDC compared to ours. PW5 has similar design concept as ours except the detector does not have any background suppression mechanism (Wolfgang Hennig et al., 2009). This could be a possible reason for its high MDC.

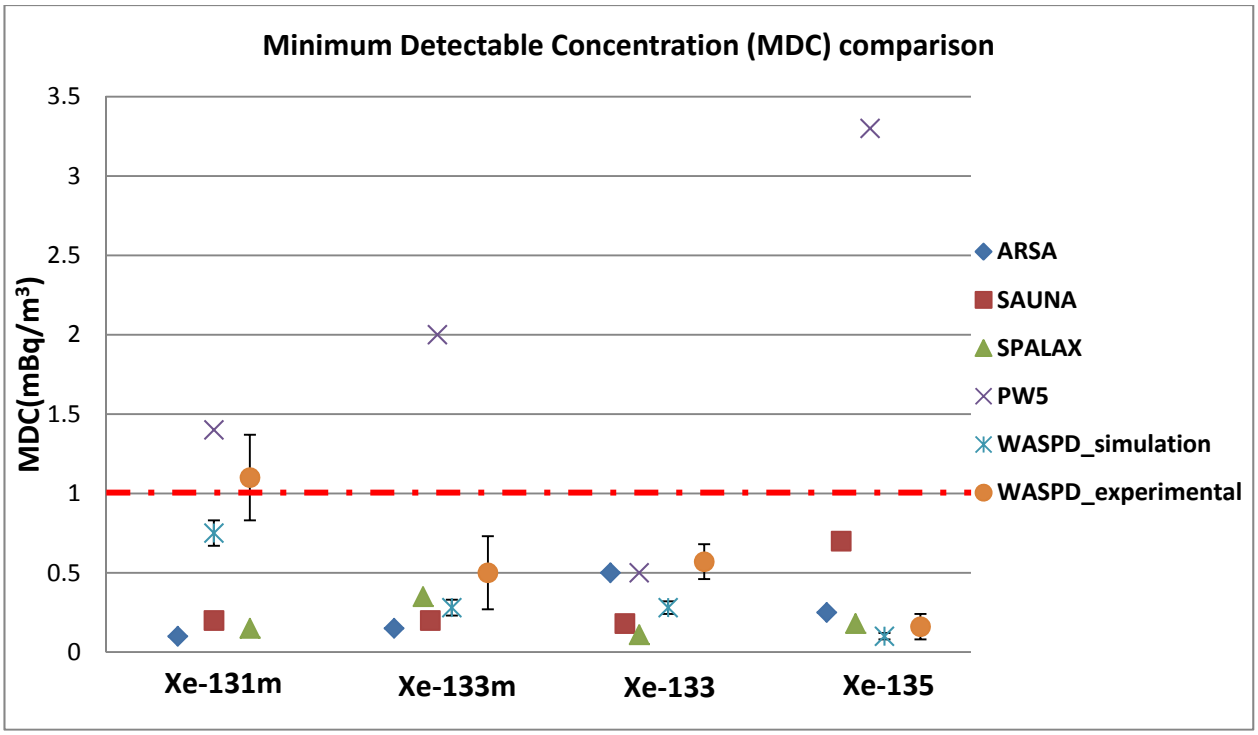

Fig. 4.17: MDC comparison with other radioxenon detection systems.

5. Conclusions and future work

5.1 Conclusions

A well-type phoswich detector with Compton suppression capability was designed, constructed and characterized at Oregon State University. The phoswich detector used in this work consisted of three scintillation crystals: a BC-400 crystal to detect beta and conversion electrons, a CsI(Tl) crystal to detect X-rays and gamma-rays and a BGO crystal to identify scattered photons and reduce the Compton continuum in the gamma energy spectrum. The detector performance was studied for gamma spectroscopy and radioxenon measurement.

To discriminate the different type of the anode output pulses from the detector and to calculate the corresponding energy, two different off-line pulse shape discrimination and energy measurement methods (FCR–SCR and Least Square Pulse Shape Discrimination) were tested using MATLAB. The FCR-SCR method showed a better energy resolution when compared with the least square pulse shape discrimination method.

All pulses from the detector were digitally processed using a user-programmable digital pulse processor to discriminate different pulse shapes and radiation interaction events in the detector. A real-time digital pulse processing firmware was implemented in a FPGA. The pulse processing algorithm has four operational modes: Scope, Pulse-Shape Analysis, Coincidence Event and Multichannel Analyzer modes. The detector and the digital pulse processor were tested for measuring radioxenon through beta/gamma coincidence technique by activating stable and enriched isotopes of ^{130}Xe, ^{132}Xe and ^{134}Xe.

Background suppression study showed that, integrating a BGO to the detector has resulted in Compton suppression of (49±9) % in the energy range 10-400 keV. The Compton suppression mechanism reduces the Compton continuum from ^{137}Cs 662

keV photons by 67-30% in the energy range 10-350 keV. The phoswich detector can be used in environments where there is high background in the energy range of interest. From Beta/Gamma coincidence measurements with ^{131m}Xe, ^{133}Xe/ ^{133m}Xe and ^{135}Xe radioisotopes, the 31 and 81 keV photopeaks showed energy resolution of 47.7% and 27.6% respectively. The 250 keV photopeak showed energy resolution of 19.3%. The MDC calculated for all xenon radioisotopes showed that the results are close to or below the minimum IMS requirement of 1 mBq/m^3.

In radioxenon measurement where gases travel a long distance before reaching measurement stations, background suppression is an important component. The phoswich detector developed distinguishes itself from the current radioxenon detection instruments, such as ARSA, SAUNA and ARIX by eliminating the usage of multiple PMTs. Results showed that all radioxenon measurements can be done by employing a phoswich scintillator coupled to a single PMT. This will reduce the need for gain matching between PMTs. As a result it will enhance the detector robustness and it reduces the detector complexity. Reducing the complexity will ease the assembly procedure hence reducing the overall detector cost.

Implementing all pulse processing functions including energy measurement and histogram on a FPGA resulted that pulses were processed fast and with less dead time, it was easier to change code without changing the hardware, and there was no need for external memory for histogram and energy measurement.

The Compton-suppressed well-type phoswich detector integrated with real-time digital pulse processing has a promising potential to be used in the future to verify nuclear weapon testing.

5.2 Future work

The detector should be tested with real gas samples from atmosphere using available sampling systems at the PNNL. The performance of the detector can be further studied by employing the detector in actual field setup and comparing its performance side-by-side with other radioxenon monitoring instruments.

Light collection efficiency of the detector can be further studied by reassembling the detector with wrapping materials having high reflectivity. In plastic scintillators, xenon samples diffuse into the plastic material and remains there for a long time. This causes memory effect, which increases the MDC of the detector. The memory effect can be reduced by coating the BC-400 scintillator with various aluminum coatings.

Bibliography

ARSA. (2013). Retrieved May 2, 2013, from http://picturethis.pnl.gov/picturet.nsf/All/3ZHRYX?opendocument

Auer, M., Kumberg, T., Sartorius, H., Wernsperger, B., & Schlosser, C. (2010). Ten years of development of equipment for measurement of atmospheric radioactive xenon for the verification of the CTBT. *Pure and Applied Geophysics*, *167*(4-5), 471–486.

Bardelli, L., Bini, M., Poggi, G., & Taccetti, N. (2002). Application of digital sampling techniques to particle identification in scintillation detectors. *Nuclear Instruments and Methods in Physics Research Section A: Accelerators, Spectrometers, Detectors and Associated Equipment*, *491*(1), 244–257.

Bläckberg, L., Fay, A., Jõgi, I., Biegalski, S., Boman, M., Elmgren, K., … Nielsen, F. (2011). Investigations of surface coatings to reduce memory effect in plastic scintillator detectors used for radioxenon detection. *Nuclear Instruments and Methods in Physics Research Section A: Accelerators, Spectrometers, Detectors and Associated Equipment*, *656*(1), 84–91.

Bowyer, T. W., McIntyre, J. I., & Reeder, P. L. (1999). High-sensitivity detection of xenon isotopes via beta-gamma coincidence counting. *Proceeding of the 21st Seismic Research Review: Ground-Based Nuclear Explosion Monitoring Technologies, LA-UR-99-4700*, *2*, 231–241.

Browne, E., & Firestone, R. B. (1986). *Table of Radioactive Isotopes*. New York: John Wiley and Sons Inc.

Bush-Goddard, S. P. (2000). Beta spectroscopy using deconvolution and spectral stripping techniques with a triple layer phoswich detector[dissertation].

CEA - Earth and Environmental Science. (2013). Retrieved May 2, 2013, from http://www-dase.cea.fr/default.php?lang=en

Chapra, S. C. (2012). *Applied Numerical Methods* (3rd ed.).

Childress, N. L., & Miller, W. H. (2002). MCNP analysis and optimization of a triple crystal phoswich detector. *Nuclear Instruments and Methods in Physics Research Section A: Accelerators, Spectrometers, Detectors and Associated Equipment*, *490*(1), 263–270.

Cooper, M. W., Aalseth, C. E., Haas, D. A., & Hayes, J. C. (2011). Initial beta-gamma nuclear detector background study. *Monitoring Research Review*. Retrieved from http://www.rdss.info/librarybox/mrr/MRR2011/PAPERS/04-07.PDF

Cooper, M. W., Carman, A. J., Hayes, J. C., Heimbigner, T. R., Hubbard, C. W., Litke, K. E., … Suarez, R. (2005). Improved β-γ coincidence detector for radioxenon detection. *Proceedings of the 27th Seismic Research Review: Ground-Based Nuclear Explosion Monitoring Technologies*, 779–786.

Cooper, M. W., McIntyre, J. I., Bowyer, T. W., Carman, A. J., Hayes, J. C., Heimbigner, T. R., Thompson, R. (2007). Redesigned β–γ radioxenon detector. *Nuclear Instruments and Methods in Physics Research Section A: Accelerators, Spectrometers, Detectors and Associated Equipment*, *579*(1), 426–430.

CTBTO Preparatory Commission. (2013). Retrieved April 9, 2013, from http://www.ctbto.org/

Currie, L. A. (1968). Limits for qualitative detection and quantitative determination. Application to radiochemistry. *Analytical chemistry*, *40*(3), 586–593.

De Voigt, M. J. A., Bacelar, J. C., Micek, S. L., Schotanus, P., Verhoef, B. A. W., Wintraecken, Y. J. E., & Vermeulen, P. (1995). A novel compact Ge-BGO Compton-suppression spectrometer. *Nuclear Instruments and Methods in Physics Research Section A: Accelerators, Spectrometers, Detectors and Associated Equipment*, *356*(2), 362–375.

Dubasov, Y. V., Popov, Y. S., Prelovskii, V. V., Donets, A. Y., Kazarinov, N. M., Mishurinskii, V. V., Skirda, N. V. (2005). The АРИКС-01 Automatic Facility for Measuring Concentrations of Radioactive Xenon Isotopes in the Atmosphere. *Instruments and Experimental Techniques*, *48*(3), 373–379.

Ely, J. H., Aalseth, C. E., Hayes, J. C., Heimbigner, T. R., McIntyre, J. I., Miley, H. S., Ripplinger, M. (2003). Novel Beta-Gamma coincidence measurements using phoswich detectors. In *Proceedings of the 25th Seismic Research Review—Nuclear Explosion Monitoring: Building the Knowledge Base* (pp. 533–541). Retrieved from http://www.rdss.info/librarybox/mrr/srr2003/hardcopy/section6.pdf

Ely, J. H., Aalseth, C. E., & McIntyre, J. I. (2005). Novel beta-gamma coincidence measurements using phoswich detectors. *Journal of radioanalytical and nuclear chemistry*, *263*(1), 245–250.

Ely, J., Hayes, J., Haas, A., Harper, W., Madison, J., Ringbom, A., & Elmgren, K. (2012). Technology goals for a next generation radioxenon monitoring system. *Pacific Northwest National Laboratory and the Swedish Defense Research Agency. Proceeding monitoring research review: ground-based nuclear explosion monitoring technologies*. Retrieved from http://www.rdss.info/librarybox/mrr/MRR2012/PAPERS/05-02.PDF

Farsoni, A. T., Alemayehu, B., Alhawsawi, A., & Becker, E. M. (2012). A compton-suppressed phoswich detector for gamma spectroscopy. *Journal of Radioanalytical and Nuclear Chemistry*, *296*(1), 63–68.

Farsoni, A. T., Alemayehu, B., Alhawsawi, A., & Becker, E. M. (2013). Real-Time Pulse-Shape Discrimination and Beta-Gamma Coincidence Detection in Field-Programmable Gate Array. *Nuclear Instruments and Methods in Physics Research Section A: Accelerators, Spectrometers, Detectors and Associated Equipment*, *712*, 75–82.

Farsoni, Abi T., Alemayehu, B., Alhawsawi, A., & Becker, E. M. (2013). A Phoswich Detector with Compton Suppression Capability for Radioxenon Measurements. *IEEE Transactions on Nuclear Science*, *60*(1), 456–464.

Farsoni, Abi T., & Hamby, D. M. (2009). Characterization of triple-layer phoswich detector for radioxenon measurements. *Proceedings of the 2009 Seismic Research Review: Ground-Based Nuclear Explosion Monitoring Technologies*, 631–640.

Farsoni, Abi T., & Hamby, D. M. (2010a). Characterizing a two-channel phoswich detector using radioxenon isotopes produced in the Oregon State University TRIGA reactor. *Proceedings of the 2010 Monitoring Research Review: Ground-Based Nuclear Explosion Monitoring Technologies*, 585–594.

Farsoni, Abi T., & Hamby, D. M. (2010b). Design and modeling of a Compton-suppressed phoswich detector for radioxenon monitoring. *Proceedings of the 2010 Monitoring Research Review: Ground-Based Nuclear Explosion Monitoring Technologies*, 595–603.

Farsoni, Abi T., Hamby, D. M., Lee, C. S., & Elliot, A. J. (2008). Preliminary experiments with a triple-layer phoswich detector for radioxenon detection. *Proceedings of the 2009 Monitoring Research Review: Ground-Based Nuclear Explosion Monitoring Technologies,* 631–640.

Farsoni, Abi T., Hamby, D. M., Ropon, K. D., & Jones, S. E. (2007). A two-channel phoswich detector for dual and triple coincidence measurements of radioxenon isotopes. *Proceedings of the 29th Monitoring Research Review: Ground-Based Nuclear Explosion Monitoring Technologies,* 747–756.

Foltz Biegalski, K. M., & Biegalski, S. R. (2001). Determining detection limits and minimum detectable concentrations for noble gas detectors utilizing beta-gamma coincidence systems. *Journal of Radioanalytical and Nuclear Chemistry*, *248*(3), 673–682.

Fontaine, J.-P., Pointurier, F., Blanchard, X., & Taffary, T. (2004). Atmospheric xenon radioactive isotope monitoring. *Journal of Environmental Radioactivity*, *72*(1-2), 129–135.

Gilmore, G. (2011). *Practical gamma-ray spectroscopy*. Wiley. com.

Grupen, C., & Buvat, I. (2011). *Handbook of particle detection and imaging* (Vol. 1). Springer Verlag.

Gupta, E. K. (1999). *Comprehensive Nuclear Test-ban Treaty [CTBT]*. Atlantic Publishers & Dist.

Hayes, J. C., Abel, K. H., Bowyer, T. W., Heimbigner, T. R., Panisko, M. E., Reeder, P. L., … Warner, R. A. (1999). Operations of the Automated Radioxenon Sampler/Analyzer—ARSA. In *Proceedings of the 21st Seismic Research Symposium: Technologies for Monitoring the Comprehensive Nuclear-Test-Ban Treaty* (pp. 249–260).

Hennig, W., Tan, H., Warburton, W. K., & McIntyre, J. I. (2006). Single-channel beta-gamma coincidence detection of radioactive xenon using digital pulse shape analysis of phoswich detector signals. *IEEE Transactions on Nuclear Science*, *53*(2), 620–624.

Hennig, Wolfgang, Cox, C. E., Asztalos, S. J., Tan, H., Franz, P. J., Grudberg, P. M., Huber, A. (2011). Study of silicon detectors for high resolution radioxenon measurements. *Journal of Radioanalytical and Nuclear Chemistry*, *712*, 75–82.

Hennig, Wolfgang, Tan, H., Warburton, W. K., & McIntyre, J. I. (2005). Digital pulse shape analysis with phoswich detectors to simplify coincidence measurements of radioactive xenon. *Proceedings of the 27th Seismic Research Review: Ground-Based Nuclear Explosion Monitoring Technologies*, 787–794.

Hennig, Wolfgang, Warburton, W. K., Fallu-Labruyere, A., Sabourov, K., Cooper, M. W., McIntyre, J. I., Ungar, K. (2009). *Radioxenon measurements with the phoswatch detector system*. XIA LLC. Retrieved from http://www.xia.com/Papers/MRR09_PW_paper.pdf

Kalinowski, M. B., Becker, A., Saey, P. R. J., Tuma, M. P., & Wotawa, G. (2008). The complexity of CTBT verification. Taking noble gas monitoring as an example. *Complexity*, *14*(1), 89–99.

Knoll, G. F. (2010). *Radiation Detection and Measurement* (4th ed.). Wiley.

Le Petit, G., Armand, P., Brachet, G., Taffary, T., Fontaine, J. P., Achim, P., … Pointurier, F. (2008). Contribution to the development of atmospheric

radioxenon monitoring. *Journal of Radioanalytical and Nuclear Chemistry*, *276*(2), 391–398.

Le Petit, G., Jutier, C., Gross, P., & Greiner, V. (2006). Low-level activity measurement of 131Xem, 133Xem, 135Xe and 133Xe in atmospheric air samples using high-resolution dual X-gamma spectrometry. *Applied radiation and isotopes: including data, instrumentation and methods for use in agriculture, industry and medicine*, *64*(10-11), 1307.

McFee, J. E., Faust, A. A., Andrews, H. R., Kovaltchouk, V., & Clifford, E. T. (2009). A comparison of fast inorganic scintillators for thermal neutron analysis landmine detection. *Nuclear Science, IEEE Transactions on*, *56*(3), 1584–1592.

McIntyre, J. I., Abel, K. H., Bowyer, T. W., Hayes, J. C., Heimbigner, T. R., Panisko, M. E., … Thompson, R. C. (2001). Measurements of ambient radioxenon levels using the automated radioxenon sampler/analyzer (ARSA). *Journal of Radioanalytical and Nuclear Chemistry*, *248*(3), 629–635.

McIntyre, J. I., Bowyer, T. W., & Reeder, P. L. (2006). *Calculation of Minimum Detectable Concentration Levels of Radioxenon Isotopes Using the PNNL ARSA System*. Pacific Northwest National Laboratory. Retrieved from http://www.pnl.gov/main/publications/external/technical_reports/PNNL-13102.pdf

Perkins, R. W., & Casey, L. A. (1996). *Radioxenons: their role in monitoring a comprehensive test ban treaty*. Pacific Northwest National Lab., Richland, WA (United States). Retrieved from http://www.osti.gov/energycitations/product.biblio.jsp?osti_id=266641

Popov, Y. S., Kazarinov, N. M., Popov, V. Y., Rykov, Y. M., & Skirda, N. V. (2005). Measuring Low Activities of Fission-Product Xenon Isotopes Using the β-γ Coincidence Method. *Instruments and Experimental Techniques*, *48*(3), 380–386.

Prelovskii, V. V., Kazarinov, N. M., Donets, A. Y., Popov, V. Y., Popov, I. Y., & Skirda, N. V. (2007). The ARIX-03F mobile semiautomatic facility for measuring low concentrations of radioactive xenon isotopes in air and subsoil gas. *Instruments and Experimental Techniques*, *50*(3), 393–397.

Reeder, P. L., & Bowyer, T. W. (1998). Delayed coincidence technique for Xe-133g detection. *Nuclear Instruments and Methods in Physics Research Section A: Accelerators, Spectrometers, Detectors and Associated Equipment*, *408*(2), 573–581.

Reeder, Paul L., Bowyer, T. W., McIntyre, J. I., Pitts, W. K., Ringbom, A., & Johansson, C. (2004). Gain calibration of a β/γ coincidence spectrometer for automated radioxenon analysis. *Nuclear Instruments and Methods in Physics Research Section A: Accelerators, Spectrometers, Detectors and Associated Equipment*, *521*(2), 586–599.

Ringbom, A., Larson, T., Axelsson, A., Elmgren, K., & Johansson, C. (2003). SAUNA—a system for automatic sampling, processing, and analysis of radioactive xenon. *Nuclear Instruments and Methods in Physics Research Section A: Accelerators, Spectrometers, Detectors and Associated Equipment*, *508*(3), 542–553.

Saint-Gobain Crystals. (2011). Scintillation Products - Organic Scintillation Materials.

SAUNA Systems - SAUNA II. (2013). Retrieved May 2, 2013, from http://www.saunasystems.se/default.aspx?PID=38

Seifert, C. E., McIntyre, J. I., Antolick, K. C., Carman, A. J., Cooper, M. W., Hayes, J. C., … Ripplinger, M. D. (2005). Mitigation of memory effects in beta scintillation cells for radioactive gas detection. *Proceedings of the 27th Seismic Research Review: Ground-Based Nuclear Explosion Monitoring Technologies*, 804–814.

USUDA, S. (1992). Development of ZnS (Ag)/NE102A and ZnS (Ag)/stilbene phoswich detectors for simultaneous α and β (γ) counting. *Journal of Nuclear Science and Technology*, *29*(9), 927–929.

Usuda, S., Abe, H., & Mihara, A. (1994a). Simultaneous counting of α, β and γ rays with phoswich detectors. *Journal of alloys and compounds*, *213*, 437–439.

Usuda, S., Abe, H., & Mihara, A. (1994b). Phoswich detectors combining doubly or triply ZnS (Ag), NE102A, BGO and/or NaI (Tl) scintillators for simultaneous counting of α, β and γ rays. *Nuclear Instruments and Methods in Physics Research Section A: Accelerators, Spectrometers, Detectors and Associated Equipment*, *340*(3), 540–545.

Usuda, S., Sakurai, S., & Yasuda, K. (1997). Phoswich detectors for simultaneous counting of α-, β (γ)-rays and neutrons. *Nuclear Instruments and Methods in Physics Research Section A: Accelerators, Spectrometers, Detectors and Associated Equipment*, *388*(1), 193–198.

Van Eijk, C. W. (2003). Inorganic scintillators in medical imaging detectors. *Nuclear Instruments and Methods in Physics Research Section A: Accelerators, Spectrometers, Detectors and Associated Equipment*, *509*(1), 17–25.

Van Eijk, C. W. (2012). Inorganic Scintillators for Thermal Neutron Detection. *IEEE Transactions on Nuclear Science*, *59*(5).

Weber, M. J. (2002). Inorganic scintillators: today and tomorrow. *Journal of Luminescence*, *100*(1), 35–45.

Wernsperger, B., & Schlosser, C. (2004). Noble gas monitoring within the international monitoring system of the comprehensive nuclear test-ban treaty. *Radiation Physics and Chemistry*, *71*(3), 775–779.

White, T. L., & Miller, W. H. (1999). A triple-crystal phoswich detector with digital pulse shape discrimination for alpha/beta/gamma spectroscopy. *Nuclear Instruments and Methods in Physics Research Section A: Accelerators, Spectrometers, Detectors and Associated Equipment*, *422*(1), 144–147.

Williams III, R. G., Gesh, C. J., & Pagh, R. T. (2006). Compendium of material composition data for radiation transport modeling. *Pacific Northwest National Laboratory*, 14–18.

Appendices

Appendix A: An example of MCNP5 photon transport modeling input deck

```
c Well-Type Compton Suppressed Phoswich Detector
c Three layars: BGO-CsI-BC400
c Testing detection efficiency of the detector for Radioxenon
c Xe-133 80keV photon
c
c Written by   Bemnet Alemayehu
c              Graduate Student
c              Oregon State University
c              alemayeb@onid.orst.edu
c
c *****************Cell Cards*****************
100 1 -7.13       -1 -2 3  #200 #300 #400              imp:p=1 $BGO
200 2 -4.51       -1 -4 5  #300 #400                   imp:p=1 $CsI
300 3 -1.032      -1 -6 7  #400                        imp:p=1 $BC400
400 4 -0.00588    -1 -8 9                              imp:p=1 $Xe
500 5  -1.406       -12 -10 11 #100 #200 #300 #400 #600    imp:p=1 $PVC
600 6  -2.2       -12 -2 1                             imp:p=1 $Teflon
700 7 -0.001205   91 -92 -90 #100 #200 #300 #400 #500 #600 imp:p=1 $air
1000 0            -91:92:90                            imp:p=0  $outside

c *****************Surface Cards*************
1 pz 7.6      $Upper Surface of BGO,CSI,BC400
2 cz 3.8      $Cylinder of BGO
3 pz 0        $Lower Surface of BGO
4 cz 2.8      $Cylinder of CsI
5 pz 1.0      $Lower Surface of CsI
6 cz 1.0      $Outer Cylinder of BC400
```

```
7  pz 2.8     $Lower Surface of BC400
8  cz 0.75    $Inner Cylinder of BC400
9  pz 3.05    $Lower surfce of gas cell
10 cz 4.0     $Cylinder of casing
11 pz -0.2    $Lower surface of casing
12 pz 8.103     $Upper surface of Teflon
90 cx 25      $Air outer cylinder
91 px -25     $Air cylinder left edge
92 px 25      $Air cylinder right edge

c ****************Material Cards*************
m1   83000.              4       $BGO
     32000.              3
     8000.              12
m2   55000.             .495      $CsI(Tl)
     53000.            .495
     81000.            .01
m3   1000.            0.5246      $BC400
     6000.           0.4754
m4   7000.            0.334298     $N; Xe-135 mix, d=4.465e-3 g/cc
     54133.          0.665702     $Xe-135
m5   17000.           0.166665
     1000.           0.499995     $PVC
     6000.           0.333340
m6   6000.            0.240183     $ Teflon
     9000.           0.759817
m7    7000.            0.781      $Air
      8000.           0.209
      18000.           0.01
mode p
```

```
c **********Source**********
sdef erg=0.081 pos 0 0 3.05 rad=d1 axs=0 0 1  ext=d2 cel 400 par=2 $ Xe-133
  si1 0.0 0.75
  si2 0.0 4.55
c **********History**********
nps 10000000
c **********Tallies**********
f18:p 100
e18 0.0 0.001 298i .3
f28:p 200
e28 0.0 0.001 298i .3
f38:p 300
e38 0.0 0.001 298i .3
```

Appendix B: An example of MCNP5 electron transport modeling input deck

```
c Well-Type Compton Suppressed Phoswich Detector
c Three layars: BGO-CsI-BC400
c Testing detection efficiency of the detector for Radioxenon
c Xe-133 45keV electron
c
c Written by   Bemnet Alemayehu
c              Graduate Student
c              Oregon State University
c              alemayeb@onid.orst.edu
c
c *****************Cell Cards*****************
100 1 -7.13       -1 -2 3  #200 #300 #400              imp:e=1 $BGO
200 2 -4.51       -1 -4 5  #300 #400                   imp:e=1 $CsI
300 3 -1.032      -1 -6 7  #400                        imp:e=1 $BC400
400 4 -0.00588    -1 -8 9                              imp:e=1 $Xe
500 5  -1.406       -12 -10 11 #100 #200 #300 #400 #600    imp:e=1 $PVC
600 6  -2.2       -12 -2 1                             imp:e=1 $Teflon
700 7 -0.001205   91 -92 -90 #100 #200 #300 #400 #500 #600 imp:e=1 $air
1000 0            -91:92:90                            imp:e=0  $outside

c *****************Surface Cards*************
1 pz 7.6      $Upper Surface of BGO,CSI,BC400
2 cz 3.8      $Cylinder of BGO
3 pz 0        $Lower Surface of BGO
4 cz 2.8      $Cylinder of CsI
5 pz 1.0      $Lower Surface of CsI
6 cz 1.0      $Outer Cylinder of BC400
7  pz 2.8     $Lower Surface of BC400
```

```
8  cz 0.75    $Inner Cylinder of BC400
9  pz 3.05    $Lower surfce of gas cell
10 cz 4.0     $Cylinder of casing
11 pz -0.2    $Lower surface of casing
12 pz 8.103   $Upper surface of Teflon
90 cx 25      $Air outer cylinder
91 px -25     $Air cylinder left edge
92 px 25      $Air cylinder right edge

c *****************Material Cards*************
m1   83000.              4       $BGO
     32000.              3
     8000.              12
m2   55000.              .495     $CsI(Tl)
     53000.             .495
     81000.             .01
m3   1000.             0.5246     $BC400
     6000.            0.4754
m4   7000.             0.334298    $N; Xe-131 mix, d=4.465e-3 g/cc
     54131.           0.665702    $Xe-131
m5   17000.           0.166665
     1000.            0.499995    $PVC
     6000.            0.333340
m6   6000.             0.240183    $ Teflon
     9000.            0.759817
m7    7000.             0.781     $Air
      8000.            0.209
      18000.            0.01
mode e
c ********************Source*******************
sdef erg=0.045 pos 0 0 3.05 rad=d1 axs=0 0 1  ext=d2 cel 400 par=3 $ Xe-131m
```

```
  si1 0.0 0.75
  si2 0.0 4.55
c ********************History*****************
nps 10000000
c ********************Tallies*********************
f18:e 100
e18 0 0.001 298i .3
f28:e 200
e28 0 0.001 298i .3
f38:e 300
e38 0 0.001 298i .3
```

Appendix C: MATLAB code for FCR-SCR pulse shape discrimination and energy measurement

```
%%%%%%% FCR-SCR pulse shape discrimination method %%%%%%%%%%%%%%

clear all

data_1 = zeros(1,2048);

valid  = 0;

fa     =  0;         % Maximum value of f1 filter convoloved with
the pulse 'integration result of each pulse'
fb     =  0;         % Maximum value of f2 filter convoloved with
the pulse 'integration result of each pulse'
fc     =  0;         % Maximum value of f3 filter convoloved with
the pulse 'integration result of each pulse'


fA     =    zeros( 1,valid);
fB     =    zeros( 1,valid);
fC     =    zeros( 1,valid);

f1     =    [-ones(1,10) ones(1,10)];            % Fast Filter
f2     =    [-ones(1,80) ones(1,80)];            % Medium Filter
f3     =    [-ones(1,750) ones(1,750)];          % Slow Filter

load('pulse')

[r,c]=size(pulse);


 for i=1:r

             data_1 = pulse(i,:);
             [mini,j] = min(data_1);    % Assigning the minimum
value of the pulse with its index "peak value of the pulse"

             if mini>0 && j>200 && j<400     % Record the pulse if
it's peak is in this range
                valid = valid+1;            % A counter to recored
valid pulses
                base = mean(data_1(j-80:j-70)); % Averaging the
base between 70 and 80 indices before the pulse

                data = [ones(1,1800)*base data_1]; % Exteding the
base line for the convolution process
```

```
                con1 =conv(double(data),double(f1)); % Convolution
of data with the fast filter f1
                fa = max(con1(1800:3000)) ;      % Summation or
integration reslut of the convolution process from f1

                con2 =conv(double(data),double(f2)); % Convolution
of data with the medium filter f2
                fb = max(con2(1800:3000));       % Summation or
integration reslut of the convolution process from f2

                con3 =conv(double(data),double(f3)); % Convolution
of data with the slow filter f3
                fc =  max(con3(1800:3000));      % Summation or
integration reslut of the convolution process from f3


                fA(valid) = fa;     % Store fa for the current
pulse
                fB(valid) = fb;     % Store fb for the current
pulse
                fC(valid) = fc;     % Store fc for the current
pulse


            end


   end
```

```
%%%%%Offline energy measurement and histogram construction %%%%%%%
    clear all

    [r,c]=size(fA);

    a_CSI = 0;
    b_CSI = 0.004;

    a_bc400 = 0;
    b_bc400 = 0.075;

    counter_csi   = 0;
    counter_bc400 = 0;

    Energy_csi    = zeros( 1,counter_csi);
    Energy_bc400  = zeros( 1,counter_bc400);


   %%%%%%%%%%%%%%%%%%% Energy analysis initialization
%%%%%%%%%%%%%%%%%%%


    %%%%%%%%%%%%  Number of bins allocation
%%%%%%%%%%%%%%%%%%%%%%%%%%%%%
    Energy_bin_csi         = 500;
    Energy_bin_bc400       = 500;

%%%%%%%%%%%%%%%%%%%%%%%%%%%%%%%%%%%%%%%%%%%%%%%%%%%%%%%%%%%%%%%%%%%
%%

    %%%%%%%%%%%% Maximum Energy allocation
%%%%%%%%%%%%%%%%%%%%%%%%%%%%%%
    max_csi               = 2000;
    max_bc400             = 2000;

%%%%%%%%%%%%%%%%%%%%%%%%%%%%%%%%%%%%%%%%%%%%%%%%%%%%%%%%%%%%%%%%%%%
%%%

    %%%%%%%%%%%%%% Energy per bin allocation
%%%%%%%%%%%%%%%%%%%%%%%%%%%%%
 binstep_csi     = 0: max_csi /(Energy_bin_csi - 1) : max_csi;
 binstep_bc400= 0: max_bc400 /(Energy_bin_bc400 - 1) : max_bc400;

%%%%%%%%%%%%%%%%%%%%%%%%%%%%%%%%%%%%%%%%%%%%%%%%%%%%%%%%%%%%%%%%%%%
%%%%
```

```
%%%%%%%%%%%%%%%%%%%%%%%%%%%%%%%%Ratio%%%%%%%%%%%%%%%%%%%%%%%%%%%%%%%%
    fab                   = fA./fB; % Result of the fast component
ratio over the medium component ratio
    fbc                   = (fB - fA)./(fC - fA); % Result of the
medium component over the slow component ratio

%%%%%%%%%%%%%%%%%%%%%%%%%%%%%%%%%%%%%%%%%%%%%%%%%%%%%%%%%%%%%%%%%%%%%%%
%%%%%%

for n=1:c;


%%%%%%%%%%%%%%%%%%%%%%%%%%CsI region %%%%%%%%%%%%%%%%%%%%%%%%%%%%%%%%
        if fbc(n) > 0.18 && fbc(n) < 0.3345 && fab(n) > 0.06284 &&
fab(n) < 0.2859
            counter_csi = counter_csi + 1;
            Energy_csi (counter_csi)= a_CSI + b_CSI * (fC(n));

%             subplot(2,1,1)
%             plot(fab(n),fbc(n),'.b')
%             axis([0 1 0 1 ])
%             grid on
%             pause(0.001)
%             hold on
%
%
%             subplot(2,1,2)
%             hist_csi = hist(Energy_csi,binstep_csi);
%             hist_csi(1) = 0;
%             hist_csi(Energy_bin_csi) = 0;
%             plot(binstep_csi,hist_csi,'-
','LineWidth',2,'MarkerSize',5),xlabel('CsI(Tl) region Gamma (FCR-
SCR): Energy (keV)'),ylabel('Counts')
%             pause(0.001)

        end

%%%%%%%%%%%%%%%%%%%%%%%%%%%%%%%%%%%%%%%%%%%%%%%%%%%%%%%%%%%%%%%%%%%%%%%

%%%%%%%%%%%%%%%%%%%%%%%%%%bc400 region %%%%%%%%%%%%%%%%%%%%%%%%%%%%%%%%
        if fbc(n) > 0 && fbc(n) < 1 && fab(n) > 0.9 && fab(n) < 1
            counter_bc400 = counter_bc400 + 1;
            Energy_bc400 (counter_bc400)= a_bc400 + b_bc400 *
(fA(n));

%             subplot(2,1,1)
%             plot(fab(n),fbc(n),'.b')
%             axis([0 1 0 1 ])
%             grid on
%             pause(0.001)
%             hold on
```

```
%
%
%             subplot(2,1,2)
%             hist_bc400 = hist(Energy_bc400,binstep_bc400);
%             hist_bc400(1) = 0;
%             hist_bc400(Energy_bin_bc400) = 0;
%
%             plot(binstep_bc400,hist_bc400,'-
r','LineWidth',2,'MarkerSize',5),xlabel('BC400 region FCR-SCR Beta:
Energy (keV)'),ylabel('Counts')
%
%             pause(0.001)
         end

%%%%%%%%%%%%%%%%%%%%%%%%%%%%%%%%%%%%%%%%%%%%%%%%%%%%%%%%%%%%%%%%%%%%%%%
         end


spec_csi = hist(Energy_csi,binstep_csi);
spec_csi(1) = 0;
spec_csi(Energy_bin_csi) = 0;

spec_bc400 = hist(Energy_bc400,binstep_bc400);
spec_bc400(1) = 0;
spec_bc400(Energy_bin_bc400) = 0;



%%%%%%%%%%%%%%%%%%%%%%%%%%%  Figure  for csi region gammma
%%%%%%%%
figure(1)
plot(binstep_csi,hist_csi,'-
r','LineWidth',2,'MarkerSize',5),xlabel('CsI region coincidence
Gamma: Energy (keV)'),ylabel('Counts')

%%%%%%%%%%%%%%%%%%%%%%%%%%%%  Figure  for bc400 region gammma
%%%%%%%%
figure(2)
plot(binstep_bc400,hist_bc400,'-
r','LineWidth',2,'MarkerSize',5),xlabel('BC400 region FCR-SCR Beta:
Energy (keV)'),ylabel('Counts')
```

Appendix D: MATLAB code for least square pulse shape discrimination and energy measurement

```
%%%%%Least square pulse shape discrimination and storing the
amplitude of discriminated pulses %%%%%%%%%


clear all
load('model_pulse_library')

pulse_corr        =    zeros(1,2048);
counter           =    0;

f_CSI_saved       =   zeros( 1,counter);
f_BC400_saved     =   zeros( 1,counter);
f_BGO_saved       =   zeros( 1,counter);
fitting_coeff_1   =   zeros( counter,3);

f_BC400           =   0;
f_CSI             =   0;
f_BGO             =   0;

z                 = [(Scaled_Average_BC400_pulses)
(Scaled_Average_CsI_pulses) (Scaled_Average_BGO_pulses)];
z_t               = z';


f_plastic        =   [-ones(1,10) ones(1,10)];
f_bgo            =   [-ones(1,80) ones(1,80)];
f_csi            =   [-ones(1,750) ones(1,750)];


load('pulse')

[r,c]=size(pulse);


for i = 1:r;

    data_1 = pulse(i,:);
    base = mean(data_1(10:30));
    pulse_corr(i,:) = data_1 - base;
    [mini,j] = min(data_1);

    if mini>0 && j>200 && j<400
       counter = counter+1;
       base = mean(data_1(j-80:j-70));
       data = [ones(1,1800)*base data_1];

       fitting_coeff_1(counter,:) =
((z_t*z)\(z_t*(pulse_corr(i,:)')))';
```

```
        con_csi = conv(double(data),double(f_csi));
        f_CSI = max(con_csi(1800:3000)) ;
        f_CSI_saved(counter) = f_CSI;

        con_plastic = conv(double(data),double(f_plastic));
        f_BC400 = max(con_plastic(1800:3000)) ;
        f_BC400_saved(counter) = f_BC400;

        con_bgo = conv(double(data),double(f_bgo));
        f_BGO = max(con_bgo(1800:3000)) ;
        f_BGO_saved(counter) = f_BGO;


    end



%     plot(pulse_corr(i,:),'r')
%     axis([0 2048 -1000 0])
%     grid on
%     pause (0.001)
%
%     plot(fitting_coeff_1(:,1),fitting_coeff_1(:,2),'.b')
%     axis([-100 4500 -100 500])
%     grid on
%     pause(0.001)


end
end
```

```
%%%%%Offline energy measurement and histogram construction %%%%%%%


a_bc400           =    0;
b_bc400           =    0.075486546;

a_csi             =    0;
b_csi             =    0.0045;

counter_csi       = 0;
counter_bc400     = 0;

Energy_csi        =    zeros( 1,counter_csi);
Energy_bc400      =    zeros( 1,counter_csi);

%%%%%%%%%%%%  Number of bins allocation
%%%%%%%%%%%%%%%%%%%%%%%%%%%%%

Energy_bin_bc400  = 250;
Energy_bin_csi    = 250;
Energy_bin_bgo    = 250;
%%%%%%%%%%%%%%%%%%%%%%%%%%%%%%%%%%%%%%%%%%%%%%%%%%%%%%%%%%%%%%%%%%%
%%

%%%%%%%%%%%% Maximum Energy allocation
%%%%%%%%%%%%%%%%%%%%%%%%%%%%%%

max_BC400 = 1000;
max_csi = 1000;
max_bgo = 1000;
%%%%%%%%%%%%%%%%%%%%%%%%%%%%%%%%%%%%%%%%%%%%%%%%%%%%%%%%%%%%%%%%%%%
%%%

%%%%%%%%%%%%%% Energy per bin allocation
%%%%%%%%%%%%%%%%%%%%%%%%%%%%%

binstep_BC400 = 0: max_BC400 /(Energy_bin_bc400 -1) : max_BC400;
binstep_csi = 0: max_csi /(Energy_bin_csi -1) : max_csi;
binstep_bgo = 0: max_bgo /(Energy_bin_bgo -1) : max_bgo;
%%%%%%%%%%%%%%%%%%%%%%%%%%%%%%%%%%%%%%%%%%%%%%%%%%%%%%%%%%%%%%%%%%%
%%%%

%%%%%%%%%%%%%%%% Memory allocation for spectrum
%%%%%%%%%%%%%%%%%%%%%%%

hist_BC400 = zeros(1, length(binstep_BC400));
hist_csi = zeros(1, length(binstep_csi));
hist_bgo = zeros(1, length(binstep_bgo));
%%%%%%%%%%%%%%%%%%%%%%%%%%%%%%%%%%%%%%%%%%%%%%%%%%%%%%%%%%%%%%%%%%%
%%%%
```

```
for n=1:counter-1;


      %%%%%%%%%%%%%%%%%%%%%%%%%CsI
region%%%%%%%%%%%%%%%%%%%%%%%%%%%%%%%%
   if fitting_coeff_1(n,1) <= 450 && fitting_coeff_1(n,2)>= 30

      counter_csi = counter_csi + 1;
      Energy_csi(counter_csi) = a_csi + b_csi * (f_CSI_saved(n)) ;


      subplot(2,1,1)
      plot(fitting_coeff_1(n,1),fitting_coeff_1(n,2),'.b')
      axis([-100 4500 -100 500 ])
      grid on
      pause(0.001)
      hold on

      subplot(2,1,2)
      hist_csi = hist(Energy_csi,binstep_csi);
      hist_csi(1) = 0;
      hist_csi(Energy_bin_csi) = 0;
      plot(binstep_csi,hist_csi,'-
','LineWidth',2,'MarkerSize',5),xlabel('CsI(Tl) region Gamma:
Energy (keV)'),ylabel('Counts')
      pause(0.001)

   end

%%%%%%%%%%%%%%%%%%%%%%%%%%%%%%%%%%%%%%%%%%%%%%%%%%%%%%%%%%%%%%%%%%%%%%%%%%%%

         %%%%%%%%%%%%%%%%%%%%%%%%BC400
region%%%%%%%%%%%%%%%%%%%%%%%%%%%%%%%%
   if fitting_coeff_1(n,1) >= 50 && fitting_coeff_1(n,2)<= 20 &&
fitting_coeff_1(n,1) <= 1500

      counter_bc400 = counter_bc400 + 1;
      Energy_bc400(counter_bc400) = a_bc400 + b_bc400 *
(f_BC400_saved(n)) ;

      plot(pulse(n,:),'r','LineWidth',3,'MarkerSize',8);
      axis([ 0 2048 0 4096]);
      grid on
      pause

      subplot(2,1,1)
      plot(fitting_coeff_1(n,1),fitting_coeff_1(n,2),'.b')
      axis([-100 4500 -100 500 ])
      grid on
      pause(0.001)
```

```
      hold on


      subplot(2,1,2)
      hist_BC400 = hist(Energy_bc400,binstep_BC400);
      hist_BC400(1) = 0;
      hist_BC400(Energy_bin_bc400) = 0;
      plot(binstep_BC400,hist_BC400,'-
r','LineWidth',2,'MarkerSize',5),xlabel('BC-400 region Beta: Energy
(keV)'),ylabel('Counts')
      pause(0.001)


   end

%%%%%%%%%%%%%%%%%%%%%%%%%%%%%%%%%%%%%%%%%%%%%%%%%%%%%%%%%%%%%%%%%%%%%%%
   end


% hist_csi = hist(Energy_csi,binstep_csi);
% hist_csi(1) = 0;
% hist_csi(Energy_bin_csi) = 0;
%
% hist_BC400 = hist(Energy_bc400,binstep_BC400);
% hist_BC400(1) = 0;
% hist_BC400(Energy_bin_bc400) = 0;
%
% figure(1)
% plot(binstep_csi,hist_csi,'-
r','LineWidth',2,'MarkerSize',5),xlabel('CsI region least square:
Energy (keV)'),ylabel('Counts')
% figure(2)
% plot(binstep_BC400,hist_BC400,'-
r','LineWidth',2,'MarkerSize',5),xlabel('Coincidence Beta: Energy
(keV)'),ylabel('Counts')
```